VERTICALLY LOADED ANCHOR: DRAG COEFFICIENT, FALL VELOCITY, AND PENETRATION DEPTH USING LABORATORY MEASUREMENTS

A Thesis

by

WILLIAM ANDRÉ CENAC II

Submitted to the Office of Graduate Studies of
Texas A&M University
in partial fulfillment of the requirements for the degree of

MASTER OF SCIENCE

May 2011

Major Subject: Ocean Engineering

Vertically Loaded Anchor: Drag Coefficient, Fall Velocity, and Penetration Depth Using Laboratory Measurements

VERTICALLY LOADED ANCHOR: DRAG COEFFICIENT, FALL VELOCITY, AND PENETRATION DEPTH USING LABORATORY MEASUREMENTS

A Thesis

by

WILLIAM ANDRÉ CENAC II

Submitted to the Office of Graduate Studies of
Texas A&M University
in partial fulfillment of the requirements for the degree of

MASTER OF SCIENCE

Approved by:

Chair of Committee,	Robert E. Randall
Committee Members,	Hamn-Ching Chen
	Gerald L. Morrison
Head of Department,	John Niedzwecki

May 2011

Major Subject: Ocean Engineering

ABSTRACT

Vertically Loaded Anchor: Drag Coefficient, Fall Velocity, and Penetration Depth Using Laboratory Measurements. (May 2011)

William André Cenac II, B.S, University of Louisiana

Chair of Advisory Committee: Dr. Robert E. Randall

The offshore oilfield industry is continuously developing unique and break-through technologies and systems to extract hydrocarbons from ever increasing ocean depths. Due to the extreme depths being explored presently, large anchors are being utilized to secure temporary and permanent facilities over their respective drilling/production site. A vertically loaded, torpedo-style, deepwater mooring anchor developed by Delmar Systems, Inc. is one of these anchors. The OMNI-Max anchor is an efficient, cost-effective alternative for use as a mooring system anchor intended for floating facilities. The OMNI-Max is designed to free-fall towards the ocean bottom and uses its kinetic energy for self-embedment into the soil, providing a mooring system anchor point. Values such as drag coefficient and terminal velocity are vital in predicting embedment depth to obtain the mooring capacity required by the floating facility.

Two scaled models of the Mark I OMNI-Max anchor were subjected to a series of tests in the Haynes Coastal Engineering Laboratory at Texas A&M University to evaluate the overall drag coefficient and penetration depth. The 1/24 scale model was

tested by measuring the amount of penetration into an artificial mud mixture. The 1/15 scale model was attached to a tow carriage and towed through a water-filled tank to measure the drag forces and evaluate the drag coefficient. The anchor terminal velocity was measured using underwater cameras to track the free fall of the model anchor through 15 ft of water inside the tow tank.

The 1/24 scale model penetrated the mud an average of 22 inches from the leading tip of the anchor to the mud surface, approximately 1.5 anchor lengths. The penetration depth increased as impact velocity increased, while the penetration depth decreased as the fins were retracted. The 1/15 scale anchor was towed at 6 different velocities producing a varied total drag coefficient between 0.70 and 1.12 for Reynolds number flows between 3.08E+05 and 1.17E+06. The drag coefficient increased as the fins were retracted and when the mooring rope was attached. The 1/15 scale anchor was allowed to free-fall in the tow tank and obtained an average terminal velocity of and 14.6 feet per second. The drag coefficients ranged from 0.46 to 0.83, which increased as the fins were retracted. When using the results to estimate prototype sized anchor drag coefficient, the average value was estimated to be 0.75.

DEDICATION

I would like to dedicate this thesis to my family. Without their love and support, this thesis and my education would not have been possible.

AKNOWLEDGEMENTS

I would like to thank my committee chair, Dr. Robert E. Randall, and my committee members, Dr. H.C. Chen & Dr. Gerald Morrison, for their guidance and support throughout the course of this research.

Thanks also go to my friends and colleagues and the department faculty and staff for making my time at Texas A&M University a great experience. I also want to extend my gratitude to Mr. John Shelton and Mr. Evan Zimmerman, for Delmar Systems, Inc., who provided the anchor models and support, and to Dr. Po-Hung Yeh, Mr. John Reed, Mr. Aaron Drake, and Mr. Rusty Permenter for their greatly appreciated assistance and guidance. I would also like to thank the undergraduate student workers at the Haynes Coastal Engineering Laboratory for their support with the experiments; Megan Blackburn, Eric Sonne, Chris Ryan, Paul Ramsey, Katy Stevenson, and Allison Gibson.

Finally, thanks to my family for their encouragement and support.

NOMENCLATURE

α	Adhesion Factor
A_F	Projected Frontal Area
A_s	Wetted, Surface Area
B/T	Mooring Arm is placed Between Fins (60°)
C_D	Overall Drag Coefficient
$C_{D,P}$	Drag Coefficient due to Form Drag
$C_{D,F}$	Drag Coefficient due to Skin Friction Drag
cm	Centimeter
d	Cylinder Diameter
D_p	Depth of Anchor Tip into Mud
F_D	Drag Force
F/E	Fins positioned into the Fully Extended Setting
fps	Feet per Second (ft/s)
F/R	Fins positioned into the Fully Retracted Setting
ft	Feet
Fx	Force along the X-Axis
Fy	Force along the Y-Axis
Fz	Force along the Z-Axis
G_{Su}	Undrained Shear Strength Gradient (psf/ft)
Hz	Hertz (Samples per Second)

I/L	Mooring Arm is placed In-Line with Fins
m	Anchor Mass (slugs)
M/S	Fins positioned into the Middle Setting
Mx	Moment about the X-Axis
My	Moment about the Y-Axis
Mz	Moment about the Z-Axis
N_b	T-bar Bar Factor
ρ	Fluid Density
P	Force per Unit Length on T-bar
psf	Pounds per Square Foot
Re	Reynolds Number
RPM	Revolutions per Minute
s	Second
Su	Undrained Shear Strength of Mud/Soil
V	Anchor Velocity
V_{ANCHOR}	Anchor Volume (ft^3)
V_c	Tow/Dredge Carriage Velocity
V_T	Terminal Velocity

TABLE OF CONTENTS

Page

Page

LIST OF FIGURES

Page

Page

Page

Page

LIST OF TABLES

Page

INTRODUCTION

The offshore oil industry is continuously developing innovative technologies to tackle the engineering challenges encountered on the high seas. As hydrocarbons are extracted further offshore and into deeper water, the cost to build a rigid, free standing facility becomes impractical. The second half of the 20th century has seen the rise in the use of floating facilities like Tension Leg Platforms (TLPs), SPAR platforms, Semisubmersible-Floating Production System platforms (Semisubmersible-FPSs), and Floating Production Storage and Off-loading facilities (FPSOs)(Colliat 2002). Since these floating facilities are subjected to large environmental forces and require extended amounts of time to perform their intended duties, a very cost-effective mooring method is the use of reusable, temporary anchors. There are various types of anchors available for use in offshore oil industry applications. Vertically loaded anchors include drag embedment anchors (DEAs), caisson suction pile anchors, and suction embedment plate anchors (SEPLAs). DEAs are primarily used with catenary mooring systems because a DEA is not capable of withstanding vertical loads. Meanwhile, suction piles and vertically loaded anchors provide the ability to use taut and semi taut mooring systems, which are capable of withstanding large vertical loads(Randall 2010). Delmar Systems, Inc. has designed a new iteration of a vertically loaded anchor for use in offshore facility mooring, the OMNI-Max Anchor (Patent #7,059,263).

The Mark I OMNI-Max anchor, as seen Figure 1, contains various, unique

---

This thesis follows the style of *Journal of Waterway, Port, Coastal and Ocean Engineering*.

features. The three fins toward the front, or nose, of the anchor are named the lower fins and the three fins after the mooring arm, which make up the tail of the anchor, are named the upper fins. The reason for this nomenclature is that the anchor is deployed in a vertical position, depicted in Figure 2. The fins have the ability to be retracted or extended, depending on various field and/or mooring load conditions or requirements. The upper and lower fins are retracted or extended collectively and have three different settings; fully extended (F/E), a middle setting (M/S), and fully retracted (F/R). Another key feature of the OMNI-Max is the mooring arm, where the mooring line to the facility is attached, which has the ability to rotate a full 360°(Shelton 2007). The arm position may be placed in-line with the upper and lower fins (I/L) or between the upper and lower fins (B/T) when deployed. This omni-directional mooring arm permits relatively quick deployment because orientation of the anchor with respect to the facility is not significantly critical; while for DEAs and suction piles, anchor orientation is crucial(Colliat 2002). Another feature of the OMNI-Max is the recovery pad-eye located on the rear of the anchor, behind the upper fins. This pad-eye allows for relatively quicker retrieval of the anchor compared to DEAs and suction piles(Zimmerman, Smith and Shelton 2009).

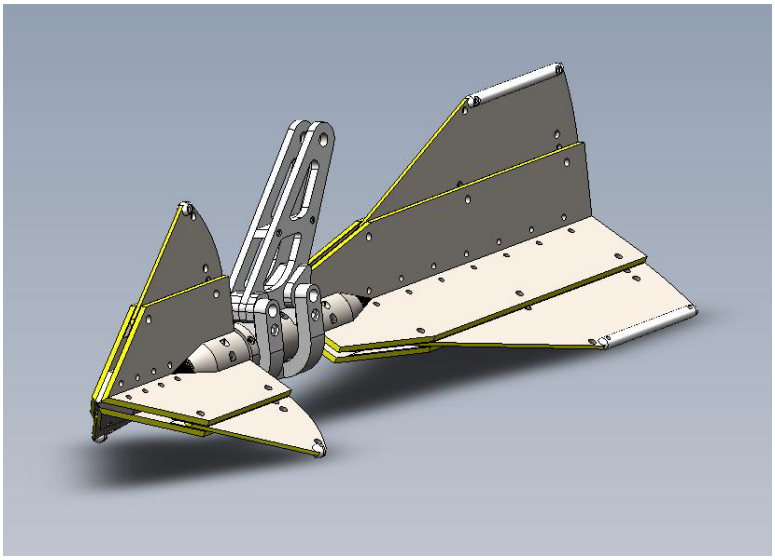

Figure 1. OMNI-Max Anchor (Drawing Courtesy of Texas A&M OWN Low Speed Wind Tunnel).

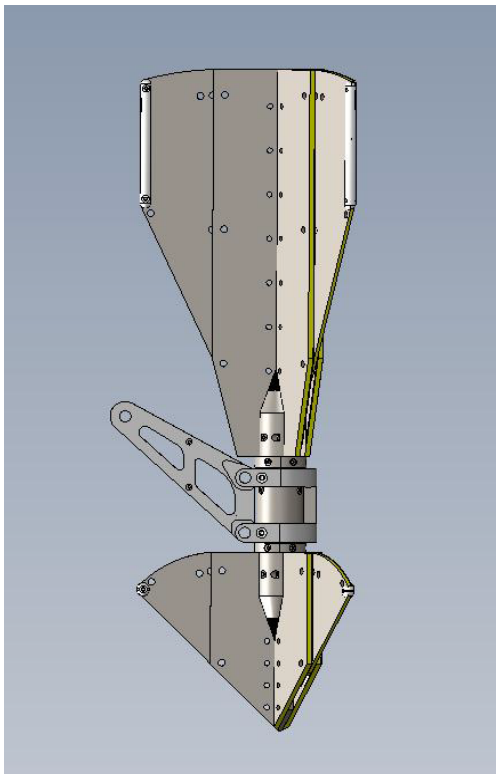

Figure 2. OMNI-Max Anchor Drawing - Side/Deployment View (Drawing Courtesy of Texas A&M OWN Low Speed Wind Tunnel).

The OMNI-Max is shaped to where the upper and lower fins act as the flukes of an anchor and the mooring arm as the anchors' shank. The angle between the "flukes" and the "shank" is crucial to the anchors' mooring performance, because the anchor is designed to penetrate further into the sea bottom when the holding capacity is exceeded(Zimmerman, Smith and Shelton 2009).

The deployment procedure of the OMNI-Max anchor is relatively quick and efficient. An Anchor Handling Vessel (AHV) attaches its' winch line to a tri-plate that carries the release hook and line connected to the anchor. The anchor has a recovery rope attached to the recovery pad-eye and a mooring line with a male/female connector with a small buoy. While the anchor is on the AHV deck, the male connector and buoy are attached to the mooring arm and the recovery rope is attached to the pad-eye. The mooring line and connector are overboarded first, followed by the anchor, and the finally the release hook attached to the tri-plate. A remotely operated vehicle (ROV) is utilized to inspect the rigging after overboarding and before release; the ROV also triggers the tri-plates' release hook and inspects the impact crater to ensure proper anchor embedment. When the male connector begins to approach the sea bottom as the AHV lowers the anchor, the ROV grabs it and places it away from the intended impact site in expected mooring direction. The buoy is attached to prevent the connector from being lost in the mud after the anchor impacts the mudline and pulls the connector. The mooring rope is given a sufficient amount of slack, allowing as much anchor penetration as possible. A guarded signal is then sent to the release hook which releases the anchor a pre-determined height above the seabed. The ROV then inspects the impact crater and

verifies the amount of penetration by inspecting the gradations located on the recovery rope. Once the depth of penetration is noted and deemed sufficient, the AHV lowers the work wire and lays down the mooring line towards the facility. If embedment is not sufficient of the impact crater is unsatisfactory, then the ROV will attach the female connector to the floating male connecter and winch the anchor out of the sediment for a second attempt at deployment. The deployment and retrieval process for the OMNI-Max anchor is filed under Patent #7,117,812 (Zimmerman, Smith and Shelton 2009).

The Mark I OMNI-Max anchor is a uniquely shaped object and some values, such as drag coefficient, are presently assumed at a value of 0.65 (Shelton 2007). Therefore, further investigation was required to find these values for various anchor fin settings and mooring arm positions, because each setting alters the anchors' geometry which changes the wetted surface area and projected frontal area. The projected frontal area of the OMNI-Max is defined as the portions of the anchor seen in Figure 3. In addition, the Mark I OMNI-Max anchor will be referred to as the "OMNI-Max" anchor for the remainder of the thesis. Due to the complexities of the OMNI-Max shape and the relatively new concept of a torpedo-style, vertically loaded anchor, a numerical modeling approach is ideal in predicting anchor performance. Therefore, engineers at Delmar Systems, Inc. have begun to construct a computer program which has the ability to predict prototype anchor deployment scenarios. Therefore, results from the numerical model need to be verified by either field or laboratory data aimed to calibrate the computer model.

A series of laboratory tests were performed which sought to evaluate the OMNI-Max anchor in different configurations and different mooring arm attachments. The primary goal of the experimental testing is to use experimental data to formulate drag coefficients of a prototype scaled OMNI-Max anchor under different configurations and with different attachments. The drag coefficient of the model-scaled anchor will be related to the prototype-scaled anchor through Reynolds number and Froude number scaling. The facility and equipment that were utilized for anchor testing and described in this thesis is based from research performed in Haynes Coastal Engineering Laboratory at Texas A&M University during the summer of 2010.

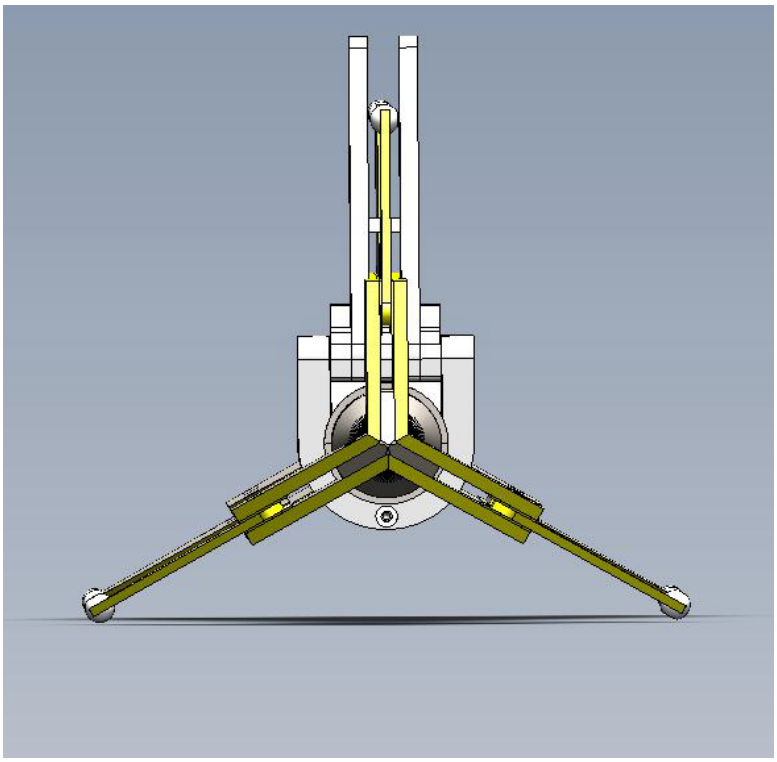

Figure 3. OMNI-Max Anchor Drawing - Front View (Drawing Courtesy of Texas A&M OWN Low Speed Wind Tunnel).

The tests performed included soil penetration testing, tow tank testing, and free fall velocity testing. The goal of the soil penetration testing was evaluation of the amount of penetration obtained under different anchor configurations. The fin position, drop height, and mooring arm position were adjusted to investigate which setting causes the least/most penetration, utilizing an artificial mud mixture. The second phase of testing was tow testing, which involved the tow/dredge carriage towing an OMNI-Max anchor model through a tow/dredge tank filled with water. The drag forces experienced by the anchor were recorded with an underwater force transducer. The final phase of testing was allowing the anchor to free fall into a deep pit where terminal velocity was measured using underwater cameras and anchor trajectory evaluated under different anchor configurations.

PREVIOUS RESEARCH

Torpedo-style mooring anchors are, relative to the other types of mooring anchors, a new method of anchor. Therefore, previous investigations focused on these anchors are relatively limited. However, the interaction between a dynamic fluid and an object has been researched extensively and provided a basis for evaluation of the OMNI-Max. The primary concerns involving torpedo anchor installation procedures is the amount of drag force acting on the anchor during free fall, the trajectory of the anchor during free fall, and the amount of penetration when the anchor impacts the seabed. This portion of the thesis will be divided into sections which pertain to different phases of testing and background knowledge for ease of reference.

Background

"Drag" is the term used by engineers and scientists, who study fluid dynamics, to describe the force on an object that resists the flow of fluid. This drag force, usually, occurs in the same orientation as the undisturbed flow and is described as a "dynamic force". This force occurs when moving fluid particles approach an object and must "slow down" which transfers the particles momentum to the object causing a force. Another stipulation, besides fluid velocity, to the fluid-structure interaction is that the size of the object, or area, exposed to the fluid is significant. For instance, a large area exposed to a dynamic fluid impedes more particles causing a high pressure. The equation to calculate drag force, seen as Equation (1), closely resembles equations to calculate particle kinetic energy in basic physics and follows the same form, with the inclusion of a drag coefficient.

$$F_D = \frac{1}{2} * C_D * \rho * V^2 * A_F \quad (1)$$

where C_D is the total drag coefficient, ρ is mass density of the fluid, V is the unobstructed fluid velocity, and A_F is the frontal, projected area exposed to the flow. This equation is applicable to air and liquid flow. However air is a compressible fluid which would require a pressure coefficient. Therefore, this pressure coefficient is ignored because water, where the OMNI-Max is deployed, may be assumed incompressible(Hoerner 1965).

Since the drag force equation may be applied to any fluid flow, it would be beneficial to characterize the flow using a nondimensional value because all Newtonian fluids (e.g. air, water, etc.) react in the same manner to external forces. Reynolds number is a nondimensional measure which depicts the ratio of inertia forces to viscous forces in a fluid flow. Therefore, this dimensionless ratio may be applied to any Newtonian fluid to relate fluid-structure interactions as long the ratio is equal. Reynolds number may be calculated by Equation (2).

$$\mathrm{Re} \equiv \frac{Vl}{\nu} \quad (2)$$

where V is the fluid velocity, l is a characteristic length scale, and ν is the kinematic viscosity of the fluid. The characteristic length is the term which may be used to relate model-scaled objects and prototype-scaled objects, if the object shape is similar. For example, if the size of the OMNI-Max anchor is shrunk, then the fluid velocity must increase or the viscosity of the fluid must decrease to obtain the same Reynolds number fluid flow. However, acquiring a “specialty” fluid that has the necessary viscosity is very

expensive; hence the use of wind tunnels to investigate fluid behavior around marine objects like submarines, boats, etc. Using this relation, Reynolds number scaling is the method that is primarily used for flow over immersed bodies, like torpedo-style, vertically loaded anchors.

The type of dynamic fluid flow encountered in torpedo-style anchor installation is sub-sonic, turbulent flow with an incompressible fluid. Therefore, the flow conditions are acceptable to use the Reynolds number similarity law, which is important when comparing prototype-scaled and model-scaled OMNI-Max anchors.

The total drag force may be broken down into two types, skin friction drag and pressure/form drag(Hoerner 1965). The OMNI-Max anchor experiences both types of drag, in varying amounts, during installation process. However, quantifying the amount of drag attributed to either skin friction drag or pressure/form drag is mainly dependent on the shape of the anchor and attachments (mooring ropes, recovery ropes, etc.). Therefore, investigations in determining how much the different modes of drag are contributing to the overall drag force acting on the anchor are reasonable. The preferred method of investigations is conducting a series of experimental tests.

Ultimately, the results found in testing should help build the computer model for prototype-scaled applications, so some mathematical extrapolation from model testing may be required. A suitable assumption may be made between the model-scaled anchor and the prototype-scaled anchor through the amount of pressure/form drag, because this type of drag is primarily dependent on the shape of an object. Assuming that the model-scaled anchor is the same shape, the ratio of pressure/form drag to overall drag should be

the same. This ratio has been researched extensively in ship modeling tests. Equations (3), (4), and (5) may be used to relate the model and prototype scaled anchors.

$$C_{D,\text{P-Model}} = C_{D,\text{Model}} - C_{D,\text{F-Model}}(\text{Re}_{\text{Model}}) \tag{3}$$

$$C_{D,\text{P-Prototype}} = C_{D,\text{P-Model}} \tag{4}$$

$$C_{D,\text{Prototype}} = C_{D,\text{F-Prototype}}(\text{Re}_{\text{Prototype}}) + C_{D,\text{P-Prototype}} \tag{5}$$

where P-Model indicates pressure/form drag experienced by the model, F-Model is the skin friction drag on the model, P-Prototype is the pressure/form drag encountered by the prototype, and F-Prototype is the skin friction drag expected by the prototype (Fernandes *et al*. 2006). To be able to separate the two different modes of drag, an equation that solves for one or the other is necessary. It should be noted that Re number is not multiplied into the equations, rather it is denoting that the term is a function of Re number. The International Towing Tank Conference in 1957 (ITTC 57) formulated an equation solving for the skin friction drag of ship models. Equation (6) is the ITTC 57 regression equation which was used to investigate skin friction drag of the anchor because the length to width ratio of the anchor is large. Equation (6) was developed from model testing of submarines and ships, which also have large length to width ratios and are subjected to larger skin drag than form drag, like a torpedo-style anchor. In addition, the equation is the result of integrating the fluid shear stresses along the surface of the object. However, when using this equation for model testing, it should be noted that Reynolds number flows greater than 10^6 are necessary because it was based on Froude number based experiments (Fernandes *et al*. 2006).

$$C_{D,F} = \frac{0.075}{(\log_{10} \mathrm{Re} - 2)^2} \tag{6}$$

Soil Penetration Testing

The soil penetration testing of the OMNI-Max anchor models requires the use of various geotechnical engineering concepts. The geotechnical aspect of the testing relates to the sediment/water mixture (mud) that the anchor will be penetrating. In prototype–scaled applications, the mud must be strong enough to support the required mooring loads of the facility, while weak enough to allow the anchor to penetrate the recommended full anchor-length beneath the mud surface (Zimmerman *et al*. 2009).

There are various environmental and internal forces involved with an object penetrating into mud. Figure 4 displays these different forces in a free body diagram. The driving force and weight of the object penetrate the object into the mud, while the adhesion force (F_{AD}), fluid inertial drag force (F_H) and bearing pressure force (F_{BE}) resist penetration. The total resistance to penetration (F) is calculated through Equation (7).

.

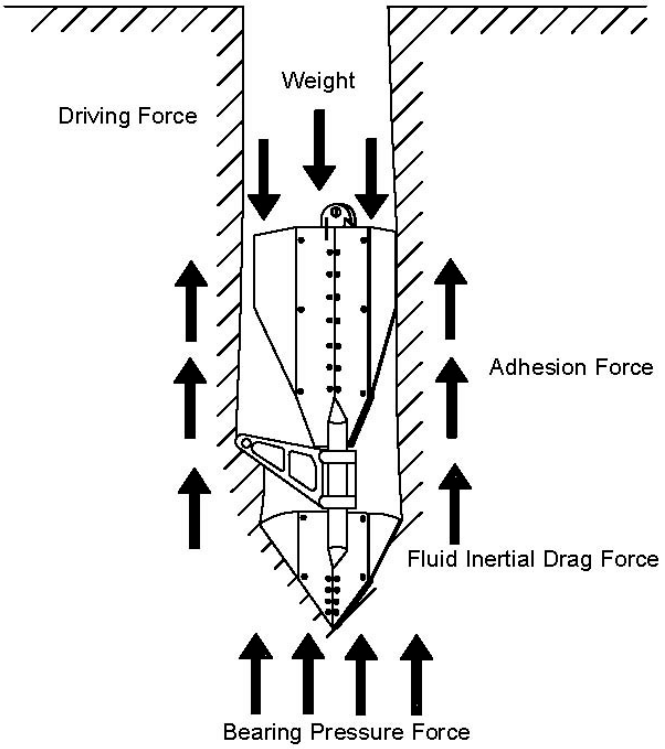

Figure 4. Forces Acting on a Penetrating Anchor.

$$F = S_c (F_{BE} + F_{AD}) + F_H \tag{7}$$

where S_c is the soil strain-rate effect, which is ratio of soil strength at some velocity to that of no velocity and is calculated by Equation (8).

$$Sc = \frac{\dfrac{F - F_H}{A_F}}{Su\left[N_C + \dfrac{\delta}{S_t}\left(\dfrac{A_S}{A_F} \right) \right]} \tag{8}$$

where S_U is the static undrained shear strength, N_C is the bearing capacity factor, δ is the side adhesion factor, S_t is the ratio of undisturbed to remolded static shear strengths, A_S is surface area of the object, and A_F is the frontal area of the object. F_H is the mud inertial drag force calculated with Equation (9)(True 1975).

$$F_H = \frac{1}{2}\rho C_D A_F V^2$$

(9)

where the terms are identical to Equation (1). The bearing pressure force is calculated with Equation (10)(True 1975).

$$F_{BE} = SuN_C A_F \tag{10}$$

and the adhesion force is by Equation (11)(True 1975).

$$F_{AD} = Su\delta \frac{A_S}{S_t} \tag{11}$$

so combining the previous equations for resistance force felt by the anchor, Equation (12) calculates the total resistance force(True 1975).

$$F = SuSc\left(N_C A_F + \frac{\delta A_S}{S_t} \right) + \frac{1}{2}\rho C_D A_F V^2 \tag{12}$$

The remaining forces that need to be evaluated are the internal forces of the penetrating object. The forces associated with the object are defined under the equations of motions, specifically Newton's second law. Equation (13) combines the objects motion and the resistance of the mud(True 1975).

$$M\frac{dv}{dt} = W^* + F_{DR} - F \tag{13}$$

where M is the mass of the penetrator and added mass, $^{dv}/_{dt}$ is the incremental change in velocity per unit time, W^* is the penetrator buoyant weight, F_{DR} is the driving force of the penetrator, and F is the total resistance of the soil.

It should be noted that these equations were developed with cylindrical objects where the shape is symmetric and soil factors such as side adhesion, bearing capacity, the strain-rate effect, and soil sensitivity are known. For the testing performed in this thesis, these soil parameters were not measured and the complex geometry of the OMNI-Max anchor is asymmetric and unique. Therefore, comparing the results from testing and results from these equations would prove inconsequential. However, there were presented to give the reader a better understanding of the forces involved.

A penetrating object is unique in that the resistant forces of the mud are dependent on the object itself. As the amount of penetration achieved by the anchor will be dependent on the soils' bearing pressure, side adhesion, and mud inertial drag. The bearing pressure force is built on mud strength, mud depth, and the manner in which the mud deforms. The bearing pressure is assumed behave like conventional static-bearing capacity calculated by plastic theory, which assumes the mud will not return back to its original state after stress is introduced. Additional factors may be included with the bearing pressure, such as the high rates of shear strain and viscous drag forces. The forces attributed to the side adhesion with the anchor are much less than the bearing pressure during penetration, due to the assumption that the momentum of the mud being separated by the penetrator will cause a small air gap between the mud and surface of the penetrator. This gap would reduce effective soil stress leaving a lower strength mud

immediately next to the penetrator, which is reflected by using a relatively low N_c value. The mud inertial drag is the resistance of the mud due to the kinetic motion of the anchor during penetration, primarily dependent on the anchor impact velocity. The mud inertial drag force is basically assumed to behave like hydrodynamic inertial drag in a fluid.

The strength of the mud was quantified through the use of a penetrometer. A penetrometer is one of the techniques used to investigate a soil's shear stress properties by a cone-shaped probe piercing though the soil and measuring the resistance. This technique works well with sands, consolidated clays, and other relatively stronger soils. However, for soft clays and mud, the accuracy of the measurements is suspect due to the low resistance of the mud on the cone. Therefore, a T-shaped probe, called a T-bar, was developed to increase the surface area of the probe to increase measurement accuracy by increasing the signal to noise ratio.

The T-bar penetrometer is a cylinder, with a length to diameter ratio of around 4, which is attached to the end of a pole. An image showcasing the T-bar used during OMNI-Max anchor testing is seen as Figure 5 as the blue object. On the other end of the pole is a load cell that records the amount of resistance force as the T-bar is penetrates the mud, generating a mud strength versus depth profile. The rate of penetration, surface roughness of the cylinder, and size of the cylinder are critical factors when converting the force measurements into soil shear strengths. The rate of penetration should be slow and steady, allowing the most measurements without imparting too much momentum into the soil. Equation (14) uses a bar factor to calculate undrained shear strength from force measurements(Stewart and Randolph 1994).

Figure 5. T-bar Penetrator.

$$P = N_b S_U d \tag{14}$$

where P is the force per unit length felt by the cylinder, N_b is the bar factor, S_U is the undrained shear strength of the soil, and d is the diameter of the cylinder. The bar factor is a function of an adhesion factor (α), which is related to the roughness of the cylinder. A higher bar factor would mean the surface of the cylinder is extremely rough. Conversely, a low bar factor indicates a very smooth cylinder with a low α. N_b ranges from 9 to 12 with a recommended value 10.5 for common applications. Research has shown that the bar factor is unaffected by the stress history or the level of stress present in the soil(Stewart and Randolph 1994).

Now that the undrained shear strength is found as a function of depth, calculating the soil strength experienced by the penetrating anchor is possible. A computer model has been developed by Delmar Systems, Inc. which forecasts the tip penetration of the OMNI-Max anchor as a function of anchor surface area, anchor bearing area, impact

speed, and anchor mass with mud effects. Equation (15) has been developed by Delmar Systems, Inc. that predicts tip penetration (D_p) as a function of undrained shear strength gradient (G_{SU}) with the assumption that the surface of the mud has an undrained shear strength of 50 psf (Zimmerman, Smith and Shelton 2009).

$$D_p = 0.46G_{Su}{}^2 - 11.6G_{Su} + 113 \tag{15}$$

However, the surface shear strength of the mud used during model testing of the OMNI-Max is much smaller and does not vary with depth as greatly compared to real-world seabed conditions. Therefore, the Equation (15) was not used, but a similar equation with different coefficients was developed after model testing.

A numerical approach was used to investigate deep penetrating anchors, similar to the OMNI-Max. A finite difference model was constructed with a basic, torpedo-style anchor geometry. An example of this type of anchor is shown as Figure 6. The OMNI-Max anchor and the generic anchor vary greatly in shape; however the same principles still apply in a numerical model. The model specifically addresses 5 issues, the 3-D effects of the flukes (not axially symmetric), impact at the mudline, mud strain-rate effects, mud deformation at mudline, and dynamic wave progression and radiation damping effects of the mud after impact. The 3-D effects of the flukes were analyzed by neglecting the flukes geometrically and factoring in their resistive effects analytically to simplify calculation and allow 2-D simulation. The boundaries of the numerical model

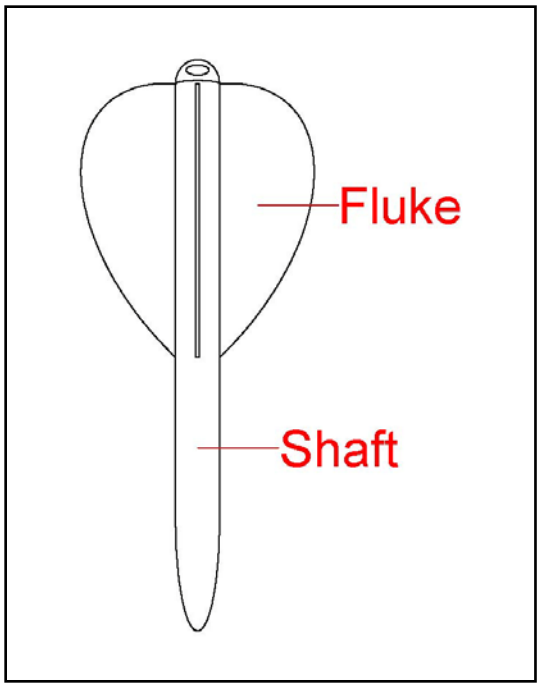

Figure 6. Generic Torpedo-Style Anchor.

are treated as a "strong box" where "fixed rollers" allowed motion of the mud vertically to address the dynamic wave progression issue. The interface between the anchor and surrounding mud was treated as rigid body and deformable body, respectively. By applying the equations of motion to the deformable body grid which follow a given shape function (i.e. anchor), then the deformable body and rigid body separate and deform autonomously. This approach addresses the issue of mud deformation at the mudline. The motion of the rigid body, anchor, is computed with the Equation (16) (Einav *et al.* 2003).

$$V(t+dt) = V(t) + \left(f - \frac{F_D(t)}{M} \right) dt \tag{16}$$

where M is the anchor mass, t is time, dt is incremental changes in time, and F_D is the total, vertical drag force calculated with Equation (17) (Einav *et al.* 2003).

$$F_D = S_f + S_b + N_f (F_f + F_b) \tag{17}$$

where S_f is the friction resistance of the shank, S_b is the vertical component of the normal-direction resistance felt by the shank, N_f is the amount of anchor flukes, and F_f and F_b are the friction resistance of a fluke and edge resistance of a fluke, respectively.

Anchor penetration into clay is the primary focus of the numerical modeling. Therefore, a rate-independent model and rate-dependent model have been evaluated. The rate-independent model entails a linear undrained shear strength gradient while the rate-dependent model addresses the strain rate issue, mentioned previously, by assuming a logarithmic increase in undrained shear strength due to strain rate effects caused by the intrusion of the anchor.

The results of the numerical model show that at the top of a fully penetrated fluke, the pore pressure of the soil is negative (a suction effect), which may affect the holding capacity of the anchor. This is attributed to the mud filling in the void left by the penetrating anchor. The model also indicates the penetration depth is primarily dependent on impact velocity; the anchor penetrates further when impact velocity is increased (Einav *et al.* 2003).

Physical modeling has also been performed on simple shaped deep penetrating anchors in lieu of numerical modeling. O'Loughlin *et al.* (2004) used a centrifuge testing technique to investigate methods in predicating anchor mooring performance. The centrifuge attempts to accurately reproduce the forces encountered in prototype-scaled

tests through accelerating the anchor faster with a higher “gravity” force in model-scaled tests, because the mud used in the centrifuge testing was natural mud found in the field. The natural mud excavated and placed in a centrifuge before testing was allowed to artificially consolidate the soil over a period of 4 days. The test anchor was then accelerated higher than gravity into the mud inside the centrifuge to evaluate penetration depth. It was determined that there is a linear increase in embedment depth with impact velocity and decreased surface area. Results also indicated that the anchor mass strongly influences impact velocity and embedment depth, and is a strong function of anchor tip geometry (O'Loughlin *et al.* 2004). However, these tests were conducted with generically-shaped, model anchors with lengths on the order of 100 millimeters. The OMNI-Max is uniquely shaped and has the ability to change shape through upper and lower fin setting and mooring arm position that effects penetration depth. Therefore, physical testing is recommended method of investigation.

Tow Tank Testing

Tow testing measures the force of fluid resistance, drag force, as the object is towed through water. The drag force is a function of a few different physical properties highlighted with Equation (18) (Swift *et al.* 2006).

$$F_D = f(L, V, \rho, \mu) \tag{18}$$

where L characterizes the shape of the object, and the remaining variables are previously defined. Therefore, by using dimensional analysis with the variables in Equation (18), two dimensionless parameters are determined, Reynolds number and drag coefficient. In most tow testing experiments, the Reynolds number is primarily a function of tow

carriage speed and the length scale of the towed object, while drag coefficient is a primarily a function of the shape of the object. Therefore, these dimensionless values are independent of one another and may be compared to evaluate the hydrodynamic performance of the object.

The drag coefficient is calculated by solving for C_D in Equation (1), and the result is depicted in Equation (19)(Fernandes and Mineiro 2007).

$$C_D = \frac{F_D}{\frac{1}{2}\rho A_F V^2} \tag{19}$$

The benefit of tow testing is that F_D may be measured accurately though the uses of relatively inexpensive force measuring devices. Drag coefficients for many simply shaped objects like plates, cones, cylinders, etc. have been evaluated and their drag coefficients are well published(Hoerner 1965). For example, previous work has shown that for spheres, the drag coefficient decreases drastically at a Reynolds number around 2.00E+05, then gradually increases and remains constant as the Reynolds number increases (Munson *et al.*1990) However, complex shapes have exhibited the same pattern of drag coefficient behavior, which requires consideration during testing of the OMNI-Max(Fernandes and Mineiro 2007).

Along with the drag coefficient, tow testing does have the ability to calculate the added mass associated with objects. This may be performed by measuring the drag force under constant accelerations and decelerations and comparing them to the drag force under constant velocity(Fernandes and Mineiro 2007). However, when evaluating the

drag coefficient for the OMNI-Max in tow testing, the model anchor was towed at a constant velocity, so the forces due to added mass were not present.

Tow tests have been performed with complex shapes, like the OMNI-Max. Testing performed by Fernandes *et al.* (2007) involved towing a sub-sea manifold through a water-filled tank. The manifold was oriented in three different directions to assess the complex shapes' drag coefficient as a function of flow orientation. The drag force was recorded with a linear load cell, placed on the tow carriage, and measuring the force imparted by the drag on the manifold through a stiff support arm. This manifold was towed at a constant speed and drag force was measured and used to calculate drag coefficient. Another instance of tow testing was performed by Swift *et al.* (2006) when the research focused on measuring the drag force on a bio-fowled net. A clean net was attached to a rope harness, and the rope was connected to a load cell on the tow carriage which recorded the drag forces. The clean net was swapped with a bio-fowled net and the test was repeated. The difference in force measurements is the drag force due to bio-fowling. The same concept will be used to evaluate affects of the mooring rope on drag force encountered by the OMNI-Max anchor.

The tow tank testing which was performed with the OMNI-Max anchor model is a classic example of tow tank testing. However, due to the OMNI-Max's complex shape, experiments need to be performed with small-scaled anchors models to better quantify the drag coefficient, with the anchor under different settings. It has been shown that models with a higher model to prototype scale ratio produce more precise drag coefficient estimates(Hoerner 1965). It has also been determined that models should be

towed deep enough to avoid free surface effects such as waves caused by the tow vehicle(Fernandes and Mineiro 2007).

For tow testing, the projected frontal area and surface area of the OMNI-Max anchor were varied by changing the fin position and mooring arm position. These slight changes in object shape affect the drag coefficient with varying degrees of magnitude. For the OMNI-Max tow testing, the density of the water remained constant while the projected, frontal area and velocity were varied.

Free Fall Testing

The free fall testing performed with the OMNI-Max anchor model is a key portion of the overall evaluation of anchor performance. The goal of the free-falling testing was the measurement of the terminal velocity of the anchor with different attachments and different settings, along with anchor trajectory.

A free-falling anchor is subjected to three distinct phases of motion, an acceleration phase, a deceleration phase, and a terminal velocity phase. The acceleration phase occurs from release until the anchor reaches maximum acceleration. The deceleration phase is defined between the maximum acceleration point and the point of terminal velocity, where any acceleration is negligible. The acceleration and deceleration periods contribute with a force acting on the anchor with the following term presented as Equation (20)

$$F_A = m_{virtual} * \frac{dV}{dt} \tag{20}$$

where $m_{virtual}$ is the mass of the anchor including the added mass from the displaced water and $^{dV}/_{dt}$ is the acceleration or deceleration of the anchor. Due to the complex shape of the anchor, the $m_{virtual}$ term was extremely difficult to estimate analytically. However, it may be estimated numerically, but such was beyond the scope of this research. In addition, the anchor velocity was measured as a function of depth not time. Therefore, Equation (21) was used to convert velocity as a function of depth to velocity as a function of time.

$$\frac{dV}{dt} = \frac{dD}{dt}\frac{dV}{dD} = V\frac{dV}{dD} \tag{21}$$

where D is anchor depth. Once this expression is found using a curve fit to the test data, Equation (22) is used to calculate drag coefficient as a function of velocity.

$$C_D = \frac{mg - \rho g V_{ANCHOR} - mV\dfrac{dV}{dD}}{\dfrac{1}{2}\rho V^2 A_F} \tag{22}$$

where m is the anchor mass, V_{ANCHOR} is the volume of water displaced by a submerged anchor. The anchor motion during acceleration, after release until terminal velocity, was not evaluated for each test case. Nevertheless, case 2 is presented in the results section depicting the drag coefficient as a function of anchor velocity, with various assumptions.

The basic physics of releasing a torpedo-style anchor underwater are relatively simple. The forces acting on an object free falling through a Newtonian fluid are balanced with Equation (23), assuming the object is travelling through a fluid of constant density and viscosity (Hartman and Yates 1993).

$$F_G - F_B - F_D = F_A \tag{23}$$

where F_G is the force imparted by gravitation, F_B is the buoyancy force of the object, F_D is the drag force, and F_A is the force due to acceleration. The force due to gravitation is the weight of the object, while the buoyancy force is found by calculating the weight of the fluid displaced by the object. This is done by calculating the difference between the dry weight and the apparent, immersed weight of the object. The force due to acceleration on the object is negligible when analyzing the object at terminal velocity. Therefore at terminal velocity, the weight of the object is equally balanced by the sum of the buoyancy forces and the resisting force of fluid flowing around the particle(Hartman and Yates 1993). A free body diagram of the force balance associated with Equation (20) is presented as Figure 7.

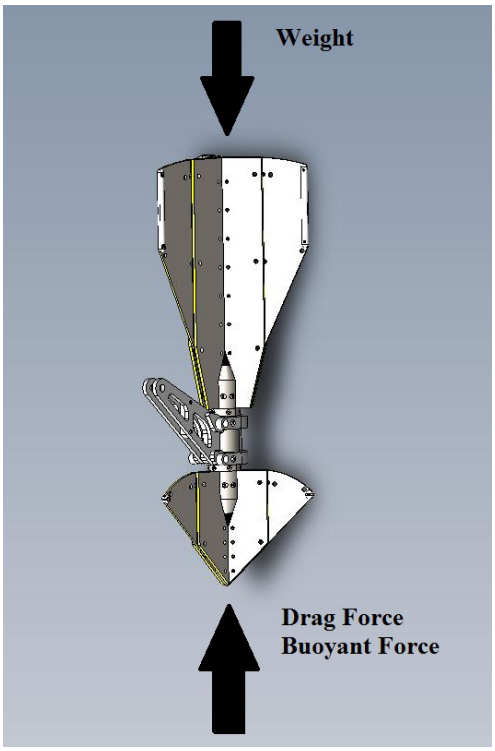

Figure 7. Free Body Diagram of Free Fall Testing Forces.

There are several different flow regimes encountered when an object is allowed to go into free fall. If the flow around the object is really slow (i.e. Re < 0.1) around spherical objects, then an analytical Stokes approximation may be resolved. However, the OMNI-Max is non-spherical and accelerates through this regime very quickly, so further investigation is unwarranted.

The next regime of fluid flow is a transitional region between a laminar, Stokes flow and a turbulent, Newtonian fluid flow. This regime exists between Re values of order 10^{-1} and 10^{3} for free falling spherical objects(Hartman and Yates 1993). For infinitely long cylinders placed in laminar flows, this transitional region lies between Re of 4 and 200 (Munson *et al.* 1990). Due to the scales used in the OMNI-Max anchor models, the use of water as the test fluid, and the expected terminal velocity of the anchor, this transitional regime of Reynolds number flows were evaluated after the anchor testing.

However, after the transitional regime of fluid flow lies turbulent fluid flow. This regime is encountered between Re of 200 and greater for cylinders placed in a laminar flow (Munson *et al*. 1990). For a free falling sphere, the turbulent flow regime exists at Re of 10^{3} and greater(Hartman and Yates 1993). Obviously, the object geometry highly influences the value of the Reynolds number flow with the chosen length scale, because the classic length scale used for both a sphere and cylinder is the diameter.

The drag forces experienced in the turbulent flow regime are represented by a drag coefficient, which is a complex function of Re number. This complexity is due to the behaviors of the boundary layer around the object under different flow velocities.

The boundary layer is a layer of viscous fluid, defined by a velocity profile starting from the surface of an object where the fluid velocity is zero, as defined by the no-slip condition, outwards toward a layer of fluid that is “unaffected” by the object. This boundary layer begins at the leading edge of an object facing a flow caused by separating fluid particles. The momentum caused by separation forms a fluid layer where the fluid velocity is less than unaffected fluid velocity. This fluid layer continues around the object until it separates from the object. This separation point is dependent on fluid flow velocity and the object geometry. For instance, when an undisturbed fluid flow encounters the leading edge of a cylinder, at very low velocities, the flow separates and traverses around the cylinder to meet at the trailing edge of the cylinder. When the flow velocity is increased, vorticity created within the boundary layer is accumulated towards the trailing edge of the cylinder due to advection. When enough fluid vorticity is acquired behind the cylinder, eddies are formed behind the cylinder. Initially, these eddies are small and contained behind the cylinder. However, as the flow velocity increases, the eddies are elongated behind the cylinder to a point where the eddies become unstable and cause a von Karman Vortex Street. As the fluid velocity increases even further, the created vortices become unstable and begin to oscillate towards either side of the cylinder causing lift forces; a phenomenon termed vortex induced vibrations. As the flow velocity increases further, separation of the boundary layer forms on the trailing edge of the cylinder, causing a pressure which is lower than the pressure at the leading edge of the cylinder. As this pressure gradient increases when further increases in fluid velocity are introduced, the boundary layer transitions from laminar to turbulent

causing a dramatic decrease the drag forces (and drag coefficient). As the flow velocity increases past the laminar to turbulent transition point, the separation point behind the cylinder traverses around the cylinder in the upstream direction, increasing the drag coefficient(Kundu and Cohen 2008). Figure 8 shows the behavior of drag coefficient as a function of Re number for various simple shapes.

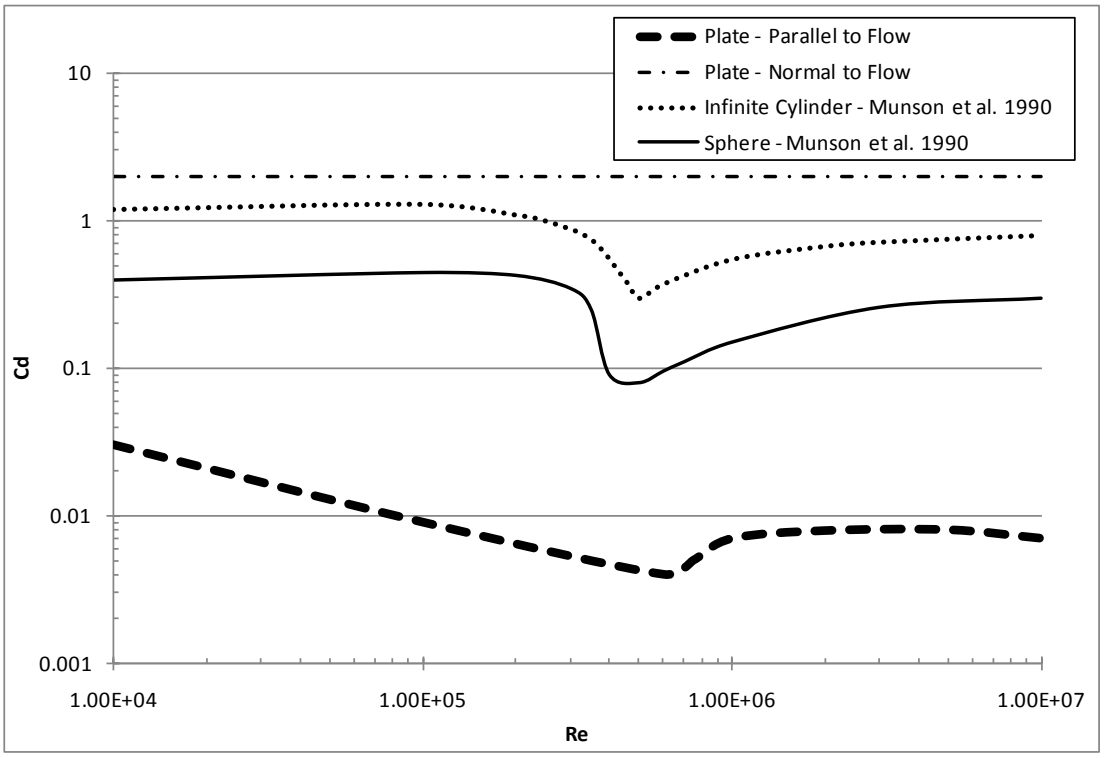

Figure 8. Drag Coefficient as a Function of Re Number for Various Simple Objects.

The drag coefficient then becomes primarily a function of Re. Figure 8 shows this dramatic dip in drag coefficient as Re is increased from about $3x10^5$ to approximately $2x10^6$ and how the drag coefficient appears to become linearly related with Re after a Re of $2x10^6$. Relating this phenomena to the free fall testing, the expected Re number flows

around the OMNI-Max anchor at terminal velocity is higher than the upper bound of the transition zone. Therefore, the calculated anchor drag coefficients should be linearly related to Re.

The geometry of the OMNI-Max anchor is hydro-dynamically streamlined and very unique. Therefore, attaching any type of measurement tool, like a device to record velocity or depth, would adversely impact the drag forces, buoyancy forces, and overall anchor weight. Consequently, velocity measurements were obtained externally through the use of underwater cameras to track the anchor motions.

The cameras are going to use the same basic principles as particle image velocimetry (PIV). PIV is a technique that measures the velocity of particles, contained within a fluid flow, with a camera. The particles (tracers) are neutrally buoyant and seeded within a fluid and illuminated with a pulse laser. The laser pulses a beam towards a series of mirrors which illuminates a thin sheet of tracers within the fluid. While the tracer particles are illuminated, a camera positioned perpendicular to the illuminated sheet creates an image by capturing the amount of laser light reflected off each particle. The illumination and image recording process is repeated for the next image (frame). Therefore, the rate at which the camera records frames is known (frames per unit time), and then the change in time is identified between frames. If the particles are moved due to fluid flow, the distance the tracer particle travels is calculated by calibrating using a camera pixel per unit length ratio. Consequently, the velocity of each particle is calculated by simple dividing the distance the particle travelled between frames and the change in time between frames (Bradley *et al.* 2002).

The same principle may be applied to any moving object, like a free falling anchor. Testing of generic torpedo-style was performed by Fernandes *et al.* (2006). A torpedo anchor was released in a basin which was 49.2 ft deep and tracked using underwater cameras. The primary goal of this research was to investigate the effects on anchor velocity and trajectory of different mooring ropes. The anchor did not reach terminal velocity. Therefore, mathematical extrapolation was conducted to estimate terminal velocity. Various mooring ropes were connected to the rear of the anchor and to a safety spring to prevent the anchor from impacting the tank floor. The anchor shape was not altered throughout the testing, with the exception of an axisymmetric ring placed on the rear of the anchor to improve anchor stabilization. Four different camera positions with various depths and distances away from the anchor were explored to track the trajectory. The research results indicated the use of stabilizing fins on the anchor body and addition of a rear line affected drag and trajectory. The model anchor without the mooring line had an estimated terminal velocity of 51.67 fps and drag coefficient of 0.5. The anchor with a mooring line had a estimated prototype scale drag coefficient equal to 0.33.

The OMNI-Max testing will not include a safety spring, but rather a mat of sand bags which will prevent the anchor impacting hard concrete. Also, due to the physical limits of the testing facility, the sediment pit size in the towing tank, camera positions were not altered. However, tracking a free-falling anchor with cameras to measure anchor velocity has been conducted.

EXPERIMENTAL SET-UP AND PROCEDURE

Facility

The OMNI-Max anchor was subjected to three testing phases in the Haynes Coastal Engineering Laboratory at Texas A&M University in College Station, Texas. The facility utilized in the laboratory was the dredge/towing tank located on the South end of the building. Figure 9 shows the dimensions (in ft) and layout of the tank looking from the North side of the building toward the South side of the building.

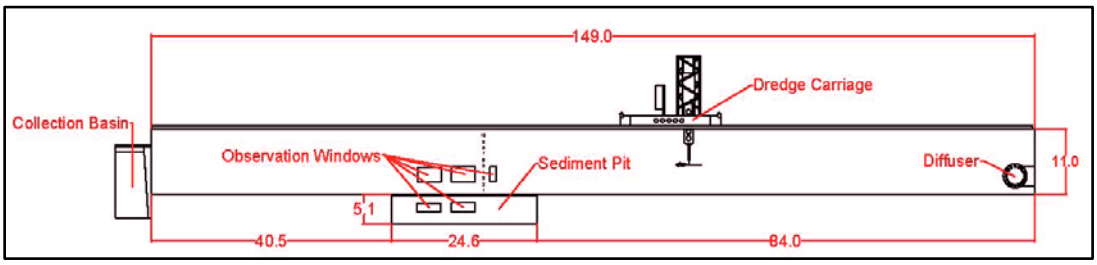

Figure 9. Towing/Dredge Tank Schematic and Dimensions (All Dimensions are in Feet).

The width of the tank from the diffuser to the collection basin, including the sediment pit, is 12 ft. The tank has the ability to generate currents, with a maximum discharge rate of 35,000 gallons per minute from the diffuser (West side of the building) towards the collection basin (East side of the building). The diffuser is a 36 in diameter steel pipe that provides the water for the artificial current to enter the tank powered by four water pumps. The collection basin is separated from the tank with a concrete wall and by aluminum weir gates. The staggered gates move up and down independently through a worm gear drive. The lower gate may be raised, evacuating the entire

tow/dredge tank of water. A water depth of 10 ft is the maximum amount allowed by the tow/dredge tank. The higher gate may be lowered, which regulates the water depth between 5 ft and 10 ft, without having to open the lower weir gate. These features of the tank are utilized for testing, but serve a supporting role by providing and holding the water needed for testing. An image of the tank looking from West to East is shown as Figure 10.

Figure 10. Tow/Dredge Tank - Looking East.

The features of the tank that are used for testing are the tow/dredge carriage, the sediment pit, and the main tank. The tow/dredge carriage is an electrically driven, computer-controlled, railed platform that moves East or West, above the tank. The

carriage has a maximum speed of 200 cm/s (6.55 ft/s). The graphical interface used to control the carriage movement is shown as Figure 11.

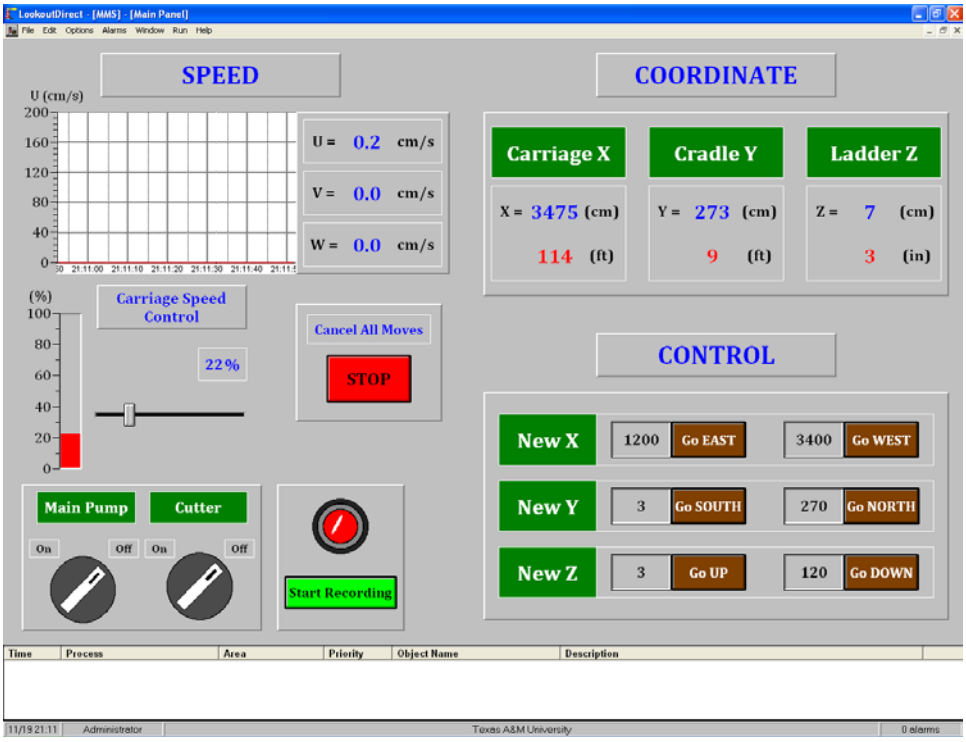

Figure 11. Towing/Dredge Carriage Control Interface.

The movements of the carriage are documented by recording the X, Y, and Z position of the tow/dredge carriage along the rail, ladder cradle, and dredge ladder, respectively. The dredging portion of the carriage is available through a reproduction of a 1/6 scale, cutter-suction dredge(Young 2009). The cutter head is fastened to an articulating arm which pivots on the lower end of the dredge ladder. The ladder is connected to the carriage by a cradle. The dredge pump and cutter head are driven by electric motors. Further details on the capabilities and instrumentation of the dredging features of the

carriage, though impressive, are not included in this report due to the irrelevancy with anchor testing. However, the carriage, cradle, and ladder are the backbone for the tow testing phase of the anchor. Figure 12 shows an image of the carriage, cradle, and ladder of the dredge/tow carriage.

Figure 12. Towing/Dredge Carriage During Typical Anchor Towing Test.

The ladder is separated into an upper section and a lower section, in which both sections move up and down, in the Z direction, using cylinders. The ladder is connected to the cradle through a force gauge located at the apex of the cradle. The upper section of

the ladder then continues through the bottom of the cradle and connects with the lower section of the ladder. For the tow testing phase, the lower section of the ladder, along with the articulating arm and cutter head were removed. Figure 13 shows the removed portions of the dredge ladder placed in a storage cradle.

Figure 13. Articulating Arm and Lower Section of Dredge Ladder on Storage Cradle.

Soil Penetration Testing

Soil Penetration Testing Set-Up

A feature of dredge/towing tank that was crucial to OMNI-Max anchor testing is the sediment pit. The sediment pit has dimensions of 25 ft long, 12 ft wide, and a depth of 5 ft. A 6 in layer of sand was placed on the pit bottom, and approximately 4 ft of artificial mud was placed in the pit above the sand layer, for approximately 1500 ft^3 of material by volume. The mud was a bentonite/sand mixture. Therefore, the maximum possible amount of OMNI-Max anchor penetration allowed by the test facility was 4.5 ft. This depth was never reached throughout the testing period. One of the sediment pits' steel plate covers was used as a work platform and placed over the pit to allow researchers to access the testing sites without disturbing the mud. A 2 in by 12 in wooden board was also used as a bridge to access the steel plate work platform. An aluminum tank and a water hose were utilized as a cleaning station to wash the anchor after each test as to ensure repeatable results by keeping the anchor mass constant. The mud as placed in the sediment pit and wooden board are shown in Figure 14.

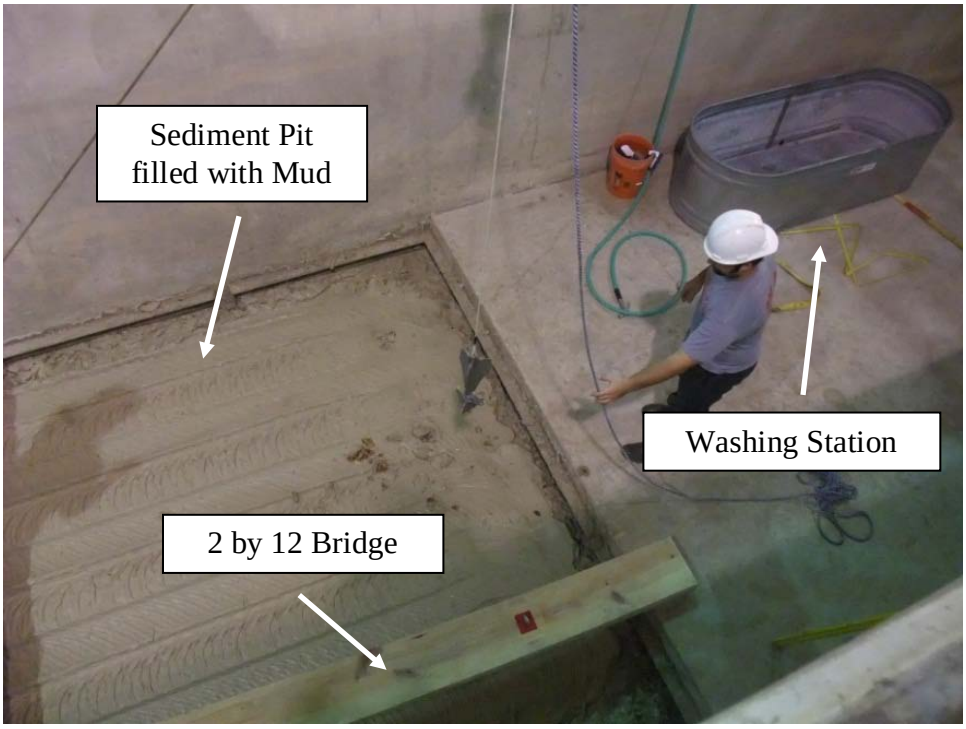

Figure 14. Soil Penetration Testing Facility.

The soil medium used for testing is an artificial laboratory mud composed of sand, bentonite, and water. The mud mixture was 51.6 % sand and 48.4% bentonite. The water content of the laboratory mud was 112.7%, by weight, with an average bulk density of 88.1 lb/ft^3. A sample of the laboratory mud was analyzed by the geotechnical engineering laboratory at Texas A&M to determine the bulk density, water content, and percent of sediment types, and the results are tabulated in Table 1. The testing was conducted by Dr. Charles Aubeny and Mr. Ryan Beemer and was greatly appreciated.

Table 1. Laboratory Mud Specifications Used During Testing.

Property	Laboratory Mud Sample
Average Bulk Density (lb/ft^3)	88.1
Water Content (%)	112.7
Fines (%)	48.4 (bentonite)
Coarse (%)	51.6 (sand)

The release mechanism used was a Peck & Hale H44-3 ram hook and is shown in Figure 15. The hook releases using approximately 15 pounds of pull using a rope connected to the hook. The release hook was attached to a shackle, and the shackle was connected to the 3-ton laboratory overhead crane. Due to the tension imparted on the hook when triggering the release, a tag line was attached to the shackle to counteract the tension force. This release system was constantly lubricated and had excellent mobility and high repeatability during the testing.

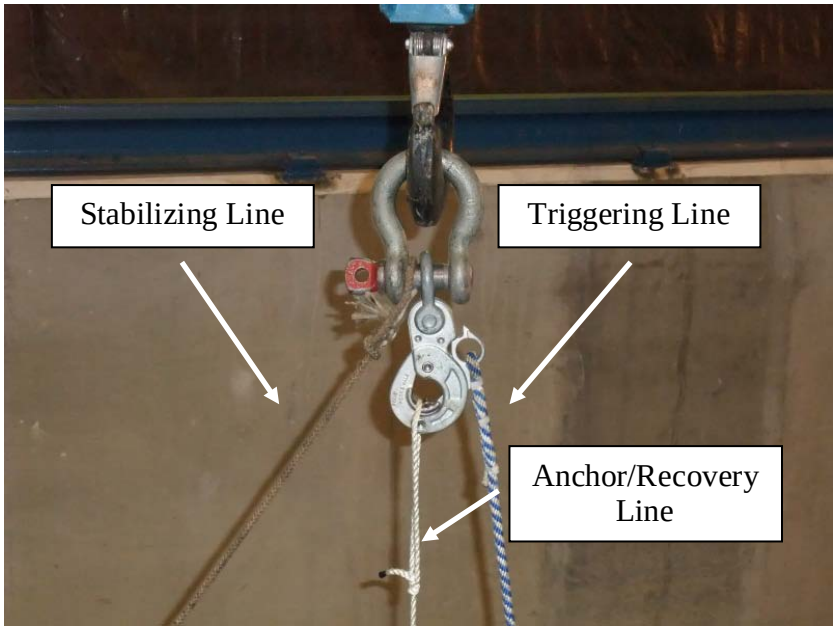

Figure 15. Release Hook Used During Soil Penetration Testing.

The strength of the mud used in the testing had to be quantified to relate penetration depth and mud strength. T-bar testing was performed to determine the undrained shear strength of the mud. A view of the T-bar rig, pre-test, is depicted in Figure 16. The load cell used to measure the resistance of the mud during penetration is shown as Figure 17. The 100 lb capacity load cell was placed between a hinge mechanism which was rigidly attached to the upper section of the dredge ladder and the square tubing supporting to the T-bar head. The T-bar was slowly lowered into the mud by lowering the upper section of the dredge ladder and the force was logged by recording the excitation voltage produced by the load cell. Before testing, the load cell was calibrated using known weights of lead bricks. Figure 16 is the first of six T-bar tests performed to obtain the undrained shear strength of soil as a function of depth.

Figure 16. T-bar Before Penetration into Mud.

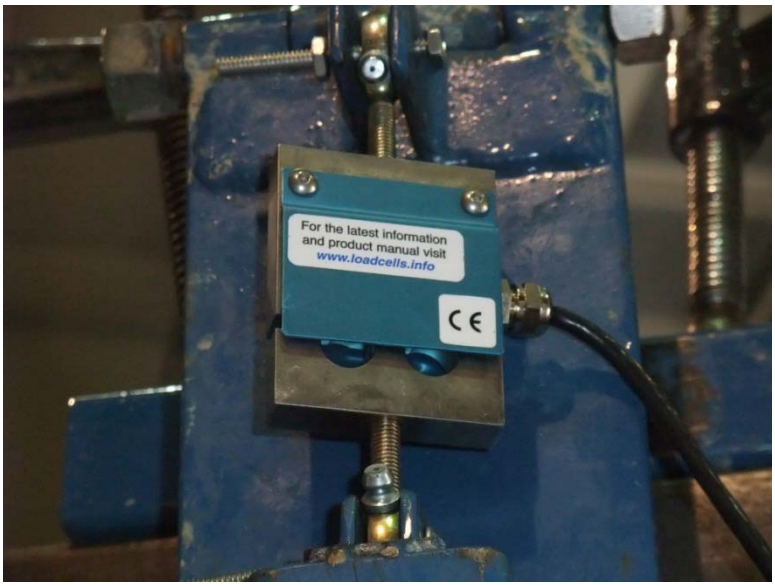

Figure 17. Force Load Cell Used During T-bar Testing.

Soil Penetration Testing Procedure

The testing was performed as follows:

1. Hang the OMNI-Max Anchor on the release hook with recovery line
2. Raise crane hook into height necessary for the tip of the anchor nose to be at the desired height above mudline
3. Position the anchor over the drop zone
4. Steady the anchor
5. The spotter puts tension on the support line
6. Pull the release rope until the hook releases anchor
7. Position the wooden board over the anchor for retrieval
8. Using the recovery line connected to the rear of the anchor, record the length of line below the mud surface

9. Remove the anchor from the mud
10. Measure the distance from the rear of any three of the anchors' tail fins to the marked position on the line
11. Wash the anchor for subsequent test

Tow Tank Testing

Tow Tank Testing Set-Up

In place of the lower section of the ladder, an attachment to the upper section of the dredge ladder was fabricated to mount a force transducer and the anchor model. Another term used to describe the force transducer is a dynamometer, and are used interchangeably. The entire attachment is referred to as the towing rig. The towing rig is shown in Figure 18. The rig is composed of various components such as the base plate, the main riser, the force transducer, the faring, the secondary riser, and the counter weight. The entire rig is hollow steel tubing and fastened together with MIG welds. A photograph of the rig, as used during all testing, is shown as Figure 19.

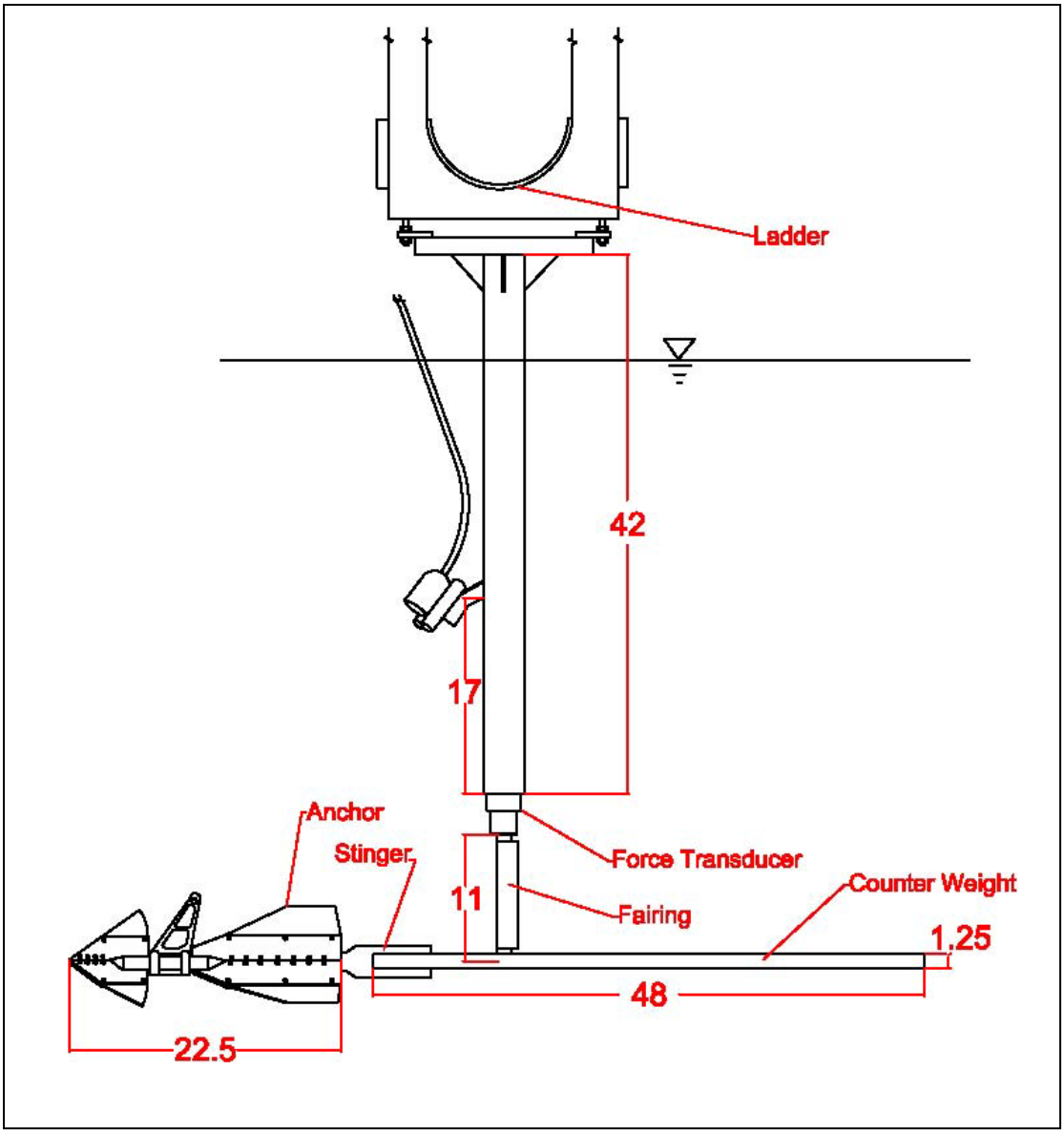

Figure 18. Towing Rig Schematic and Specifications (Dimensions in Inches).

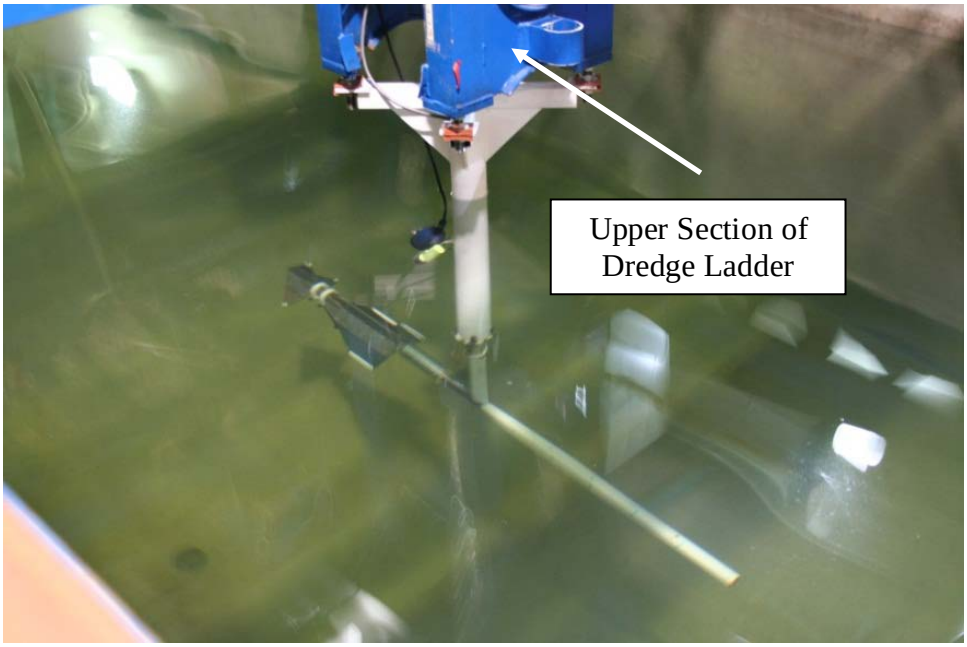

Figure 19. Towing Rig Attached to Upper Section of the Dredge Ladder.

The base plate is formed by two pieces of square steel tubing that connect the main riser to the upper section of the ladder. Steel tabs with holes were welded to the four ends of the tubing where bolts mounted on the upper section of the dredge ladder may be utilized. The tabs were sandwiched between two pieces of hard rubber, two washers, and two nuts. The use of two nuts allowed the entire rig to be adjusted to a level and straight orientation. The hard rubber pieces steadied the rig by insulating it from vibrations generated by the movement of the carriage and isolated the force transducer from electrical interference coming from any electronics on the carriage. The rubber was stiff enough to assume that the deflection due to compression of the rubber when drag forces were present on the submerged potion of the rig was negligible. A schematic of the connection is shown as Figure 20.

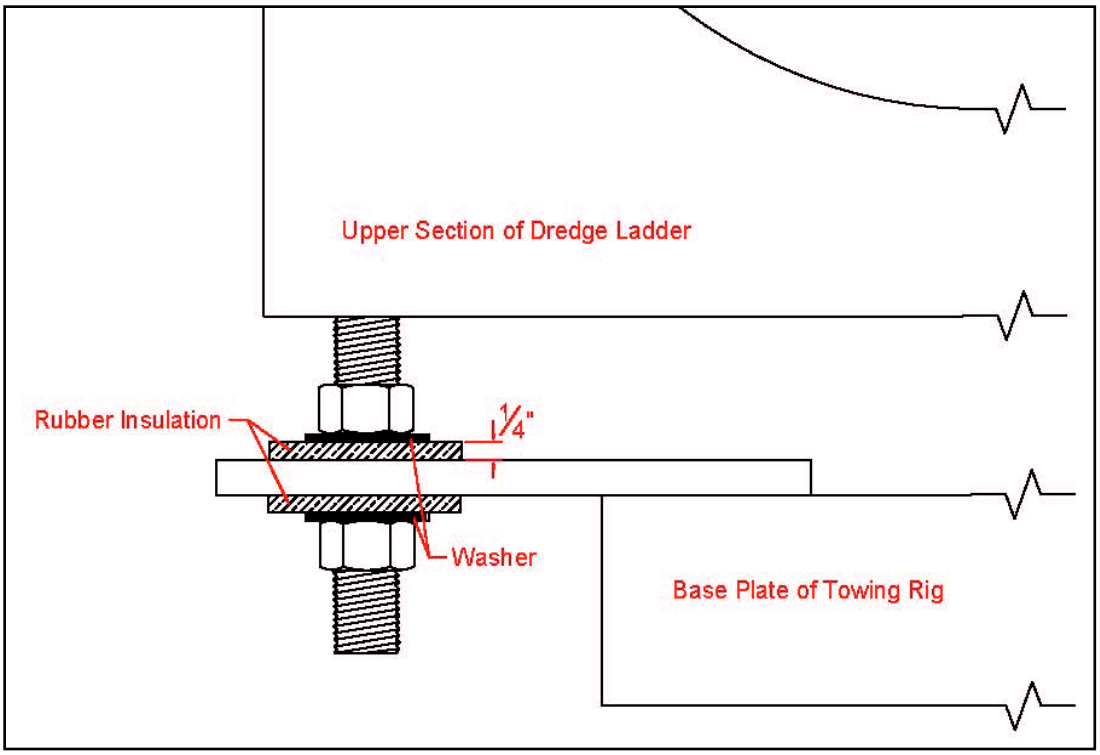

Figure 20. Towing Rig and Dredge Ladder Connection Schematic.

The main riser was welded to the base plate and reinforced with triangular gusset plates to minimize deflection and vibrations caused by drag forces. The main riser is 3 inches in diameter and 42 inches in length. The riser was notched near the base plate to allow the passage of the data cable connected the force transducer and the data collection desktop computer. Also located on the main riser is an underwater video camera with a light pod. The video camera was used to document each test run to ensure good data was being recorded without incident. The location of the camera is 3 ft above and 1 ft behind the anchor, which was deemed far enough as to not interfere with the drag force measurements. A second desktop computer was used to view and record the images taken by the camera at a rate of 30 Hz. A second underwater camera was placed in a

stationary location near the sediment to obtain a second point of view of the testing. An example of the view seen by the stationary camera is seen as Figure 21. On the bottom end of the main riser, four bolts were welded to attach the plate on which the dynamometer is mounted. A photograph of the camera mounted to the main riser is shown in Figure 22.

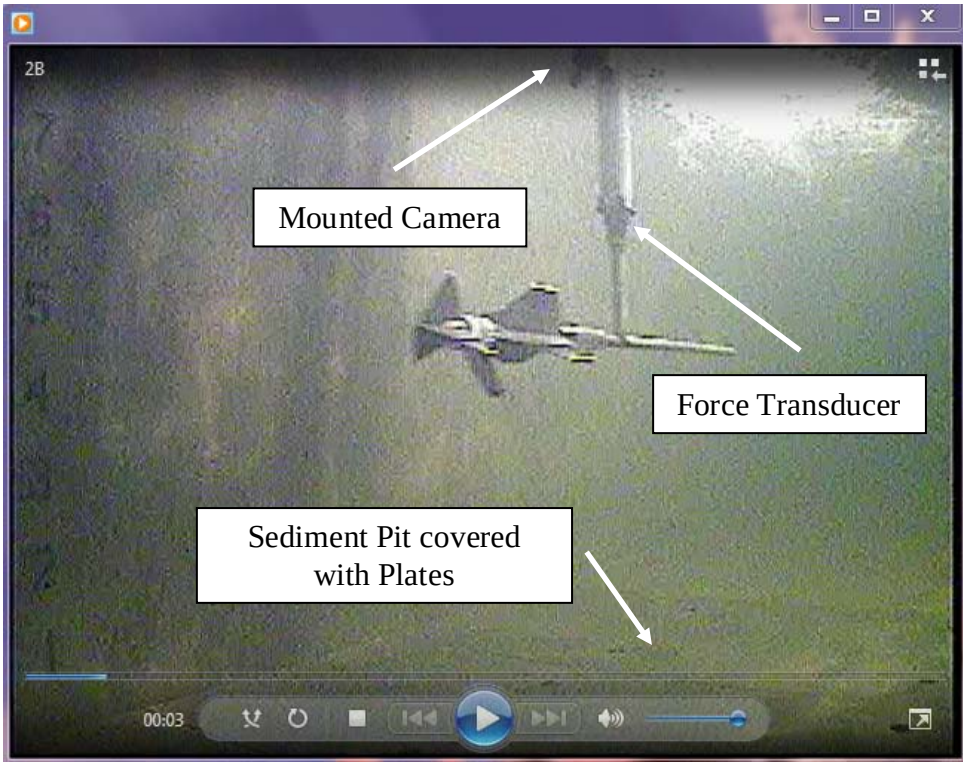

Figure 21. View of Stationary Underwater Camera During Towing Tests.

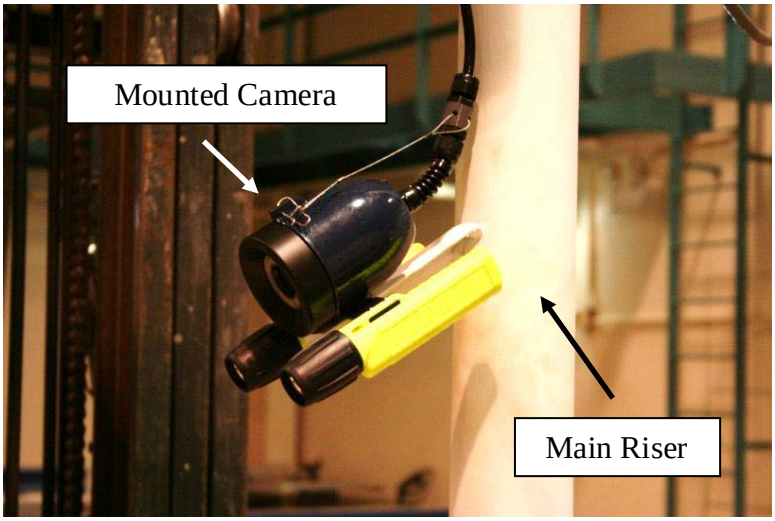

Figure 22. Mounted Underwater Video Camera Used During Towing Tests.

A mounting plate was used to fasten the lower end of the main riser and the dynamometer. The force transducer, or dynamometer, is a UDW3 underwater force transducer that has a maximum 500 in-lb moment capacity and a product of Advanced Mechanical Technology Inc. (AMTI). The transducer is 3.5 in long and 2.97 in wide for the upper portion and 2.25 in wide for the lower portion. The sensor has six channels of output, three moment channels and three force channels. The measurement elements of the transducer are attached to a central cylindrical strain element with strain gages attached around the diameter. The effective measurement center of the transducer is measured from the bottom plate of the transducer and is -0.00359 in on the X-axis, 0.0178 in on the Y-axis, and 1.77 in on the Z-axis. The capacities, sensitivities, and accuracies of the transducer are summarized in Table 2. The transducer was positioned where the positive Y-axis is facing in the same direction of the anchor (East); the positive X-axis is positioned towards the left side of the anchor when looking from the

stern of the anchor (North); and the negative Z-axis is positioned toward the tank bottom. The plate allowed adjustment of the lower portions of the rig to be aligned with the centerline of the tank, as to minimize the moment about the Z axis. The values for accuracy are calculated from an equation given in the transducer user's manual and Figure 24 depicts the sign convention graphically.

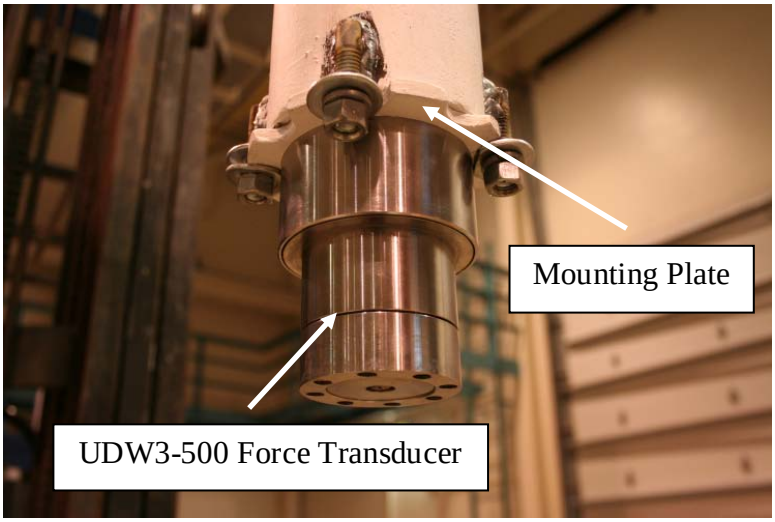

Figure 23. UDW3-500 Force Transducer and Mounting Plate Attached to Main Riser.

Table 2. UDW3-500 Force Transducer Sensitivity/Accuracy.

Model UDW3	Loading Capacity	Sensitivity/Accuracy		
		microVolt/Volt (lb)	Force/Moment	microVolt/Volt (in-lb)
Fx	250 lb	5.9568	±0.067 lb	-
Fy	250 lb	5.9612	±0.067 lb	-
Fz	500 lb	1.5541	±0.257 lb	-
Mx	500 in-lb	-	±0.047 in-lb	8.5527
My	500 in-lb	-	±0.047 in-lb	8.5445
Mz	250 in-lb	-	±0.069 in-lb	5.7924

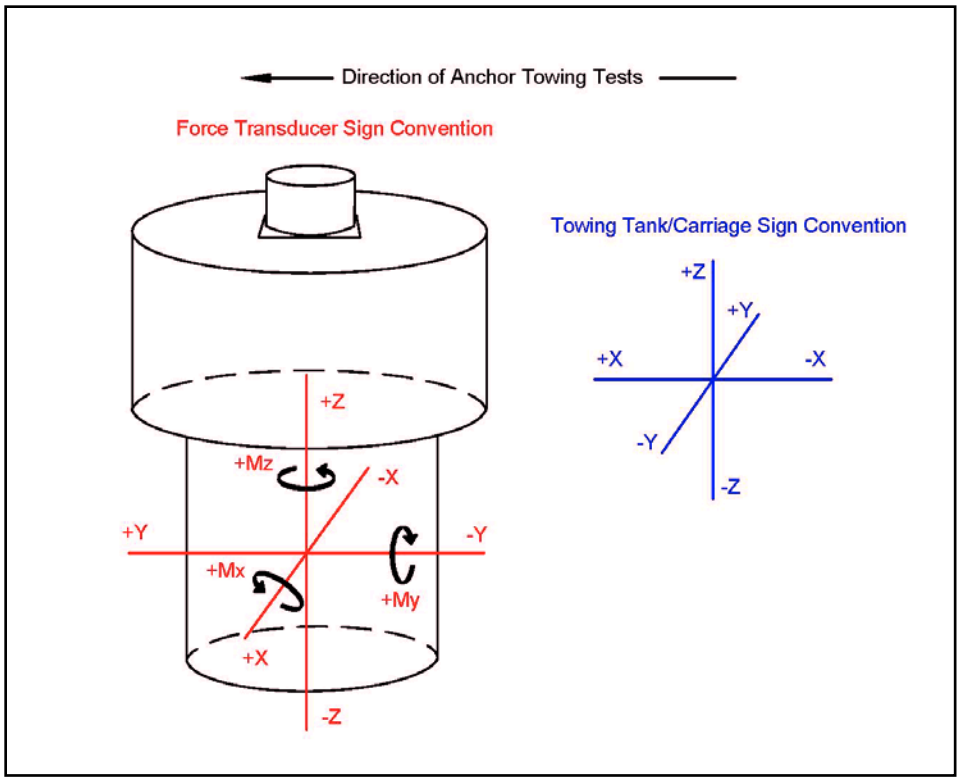

Figure 24. Sign Conventions for Carriage and Force Transducer.

The lower structure of the test rig has three main components, the horizontal pipe containing a counterweight, the vertical pipe, and the fairing. The vertical pipe connects the dynamometer to the horizontal pipe and has a diameter of 1.25 in and a length of 10.375 in. The connection between the vertical pipe and horizontal pipe is welded, and the connection between the vertical pipe and flange bracket, which bolts to the dynamometer, is also welded. The horizontal pipe is 48 in long and has a diameter 1.25 in. A 48 in long and 1 in diameter solid steel pipe was inserted into the horizontal pipe as a counterweight for providing a counter moment opposite of the anchor, preventing overload of the transducer and increasing transducer accuracy. The portion of the

horizontal pipe that is connected to the anchor is 12 in long, so 36 in of pipe consists of the tail. Therefore, the model anchor is on a moment arm of 11 in from the bottom plane of the dynamometer. A fairing was placed on the vertical pipe to minimize additional moment and vortex induced vibration (VIV) caused by fluid drag. Preliminary test runs, without the anchor, have been performed to quantify the amount of drag force caused by the lower portion of the rig. The rig induced drag force was subtracted from the drag force measured during testing, resulting in drag force due to the anchor. The lower portion of the structure is shown as Figure 25.

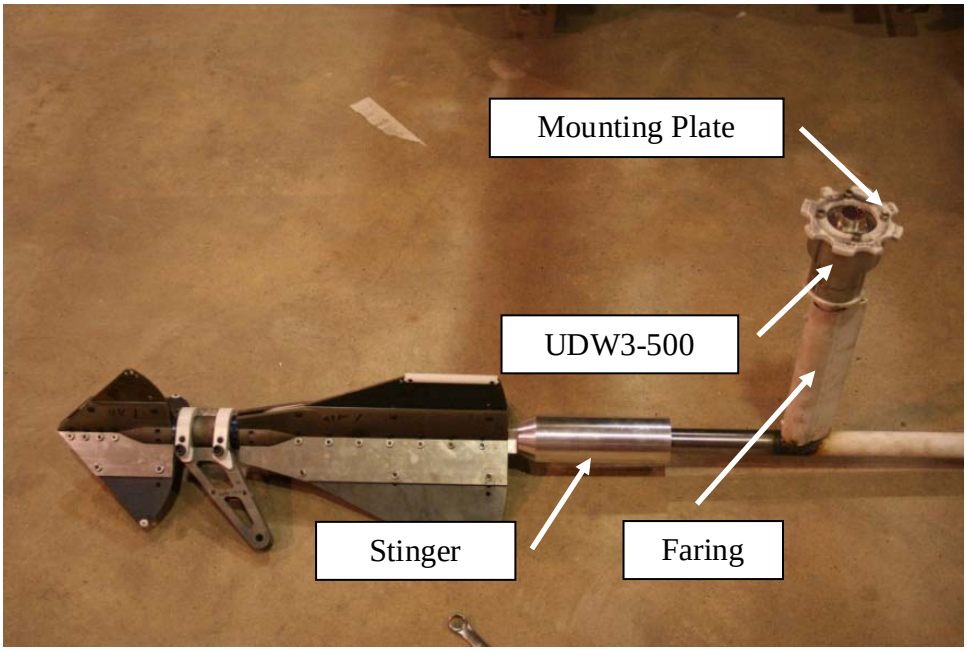

Figure 25. Lower Portion of Towing Rig with Anchor and UDW3-500 Sensor Attached.

Tow Tank Testing Procedure

The testing was performed as follows:

1. Position stinger with attached anchor onto the horizontal pipe of towing test rig
2. Clear obstructions from tow carriage path
3. Start the LabView program to record measurements from the force transducer
4. Start recording of the underwater camera video feed
5. Start the dredge carriage
6. Start the test run by accelerating the carriage towards a constant velocity
7. End the test run by decelerating/stopping the carriage
8. Board the carriage
9. Stop recording and save the underwater camera video
10. Stop recording and save the force transducer data
11. Return the carriage to the starting position
12. Reset the anchor for the next test

Free Fall Testing

Free Fall Testing Set-Up

The objective of the testing was to observe the fall trajectories, measure the fall velocity (terminal velocity), and observe the effects of various attachments upon the anchors' trajectory. The tow/dredge tank was filled with the maximum amount of water (15 ft from the bottom of the sediment pit), and sand-filled bags were placed on the bottom of the sediment pit to arrest the free falling anchor. A striped board was also hung as a background reference during testing. The tow/dredge carriage was utilized through a cantilevered platform and arm, from which the anchor was released. The velocity and trajectory were tracked and measured using two underwater video cameras.

The steel model anchor was attached to a release and recovery lines with plastic, recovery pad eyes built by the Texas A&M Wind Tunnel.

A group of sand-filled bags were placed on the floor of the sediment pit to arrest the 1/15 scale model anchor. The bags have a maximum capacity of approximately 22.5 ft^3 of material, or 0.83 yd^3. However, the bags were only half-filled with sand because of weight limitations associated with the degradation of the polyethylene mesh bag material. Therefore, the anchor had only a depth of 13 ft to obtain terminal velocity, because a half-filled bag of sand occupied 2 ft of depth. The bags were placed in the pit using the overhead crane and a spreader bar. The observation windows in the sediment pit were boarded up to prevent the anchor from cracking or breaking the windows. The arrangement of bags on the sediment pit bottom is shown in Figure 26.

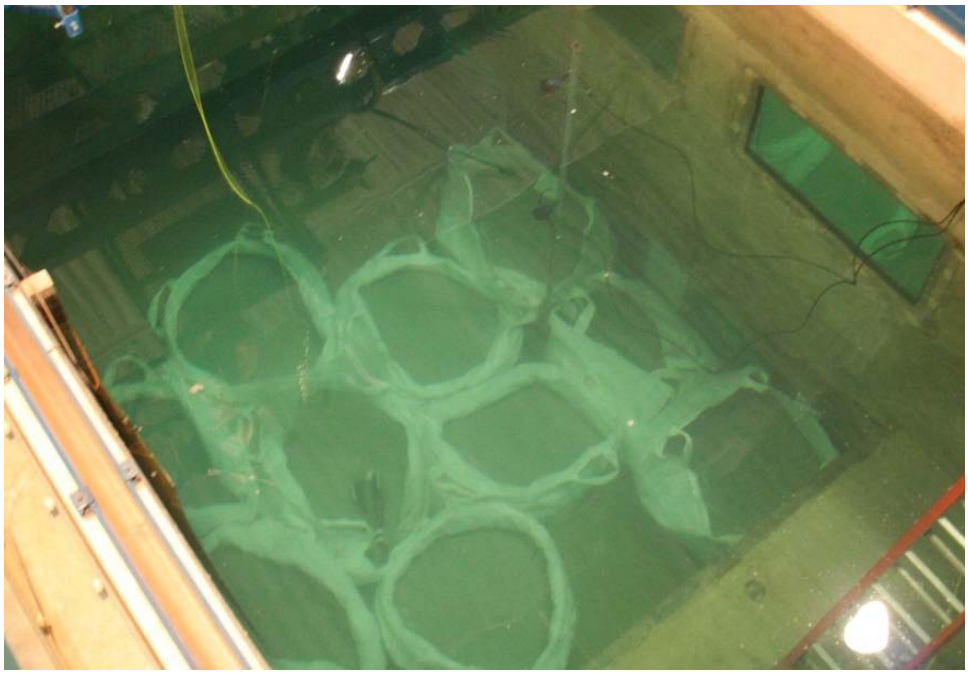

Figure 26. Sand Bag Arrangement Used During Free Fall Testing in the Sediment Pit.

Before each test, the anchor was lowered from a platform that was attached to the front of the dredge carriage. The platform was constructed with expanded metal and square steel tubing. The platform provided the researchers the ability to perform the anchor release procedure without having to enter the water. Welded to the sides of the platform were receiving brackets. The North bracket was used to support a steel cantilevered arm with a bolted hook. The arm was approximately 3 ft high and the hook was approximately 6 ft above the water surface. The hook was used to hold a steel chain. Attached to the end of the chain was a steel carabineer. The carabineer held one of the looped ends of the monofilament release line. The South bracket was used to support a steel platform holding a variable speed drill. The drill was used as the motor for the recovery winch. The winch was a capstan style winch with a 2 ft long steel cylinder attached to the drill. Looping the recovery line of the anchor around the cylinder and keeping it taught allowed the anchor to be raised or lowered safely.

The model anchor was hung above the sand bags using 200 lb test nylon fishing line and 100 lb test monofilament fishing line. The monofilament was cut into approximately 2 ft long lengths and loops were knotted onto each end. One loop was held by the carabineer and the other end was fastened to a short portion of nylon line. The other end of the short portion of nylon line was tied to a swivel. A swivel was used to minimize rotation of the model anchor, caused by the natural braiding of the nylon fishing line. Due to the loops being tied onto the monofilament line into somewhat inconsistent sizes, maintaining a constant initial anchor depth was achieved by adjusting the chain link placed on the hook. Using the chain, the anchor was lowered beneath the

water surface, where the upper fins' tail edge was slightly underwater. When the anchor was positioned into the right depth, a boat hook was used to steady the anchor and position the mooring arm into a consistent direction, either West or East. The anchor was released by burning through the monofilament line with a lighter. A recovery line consisting of the nylon fishing line was thrown in the water immediately before each test. The recovery line did not appear to affect the anchor's fall and was thrown as to not cause knots or snags, which might affect anchor velocity. An illustration depicting the release mechanism is shown as Figure 27 where the green line is the nylon line and the black line is the monofilament.

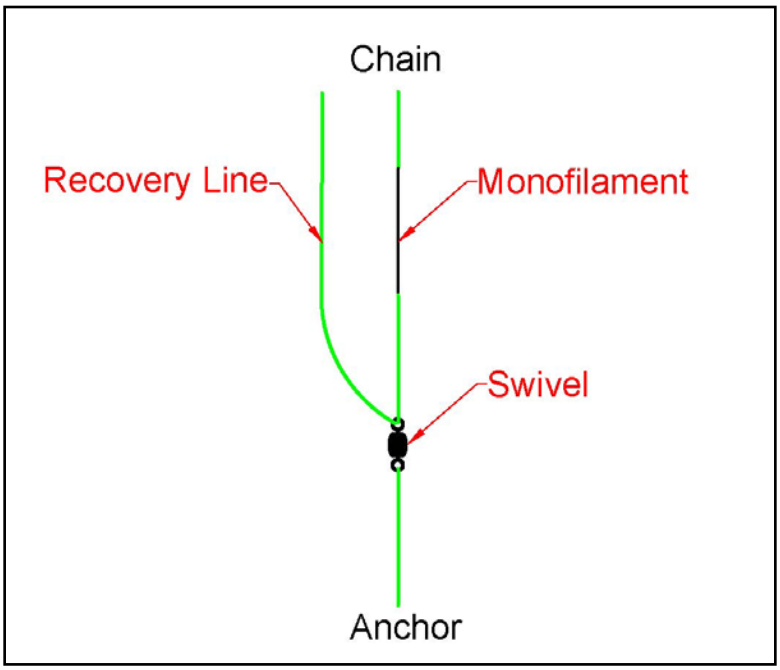

Figure 27. Free Fall Testing Release Mechanism Diagram.

The cameras used to record images of the fall of the anchor through the water column were the same cameras used to document the towing tests. The cameras were mounted on a 12 ft long pole with one camera being 5.45 ft above the sediment pit bottom and the second camera being 10.95 ft above the sediment pit bottom. The cameras were positioned on the North side of the tow tank facing Southerly. On the South side of the tank, a 10 ft long and 5 ft wide galvanized metal plate was hung by cables attached to the Southern dredge carriage rail. The plate was painted white with 3 in black stripes from the top to the bottom. In addition, a series of black stripes were painted lengthwise along the plate in 1.5 in increments to gauge the lateral travel of the anchor as it fell. The experimental layout with dimensions and locations is shown as Figure 28. The board and view seen by the shallow camera is depicted in Figure 29.

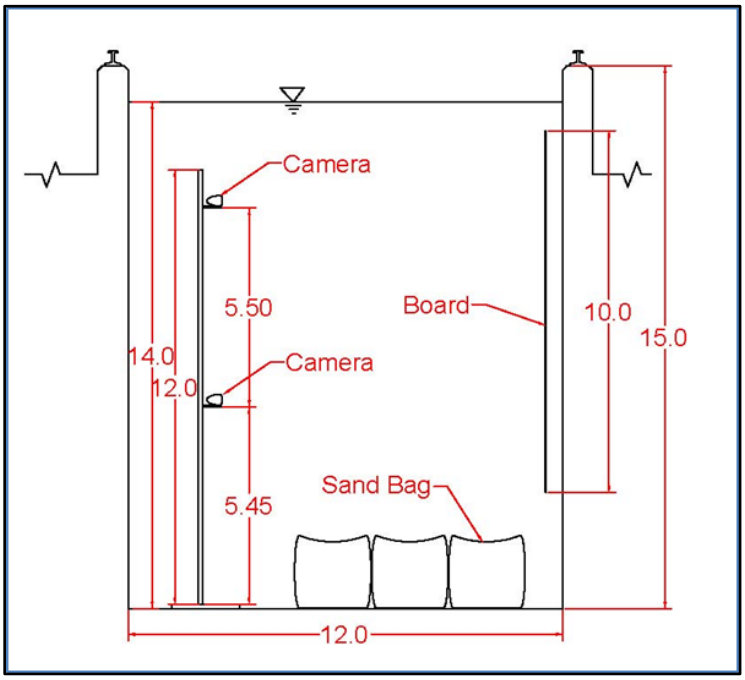

Figure 28. Free Fall Testing Tank Schematic and Diagram (Dimension in Ft).

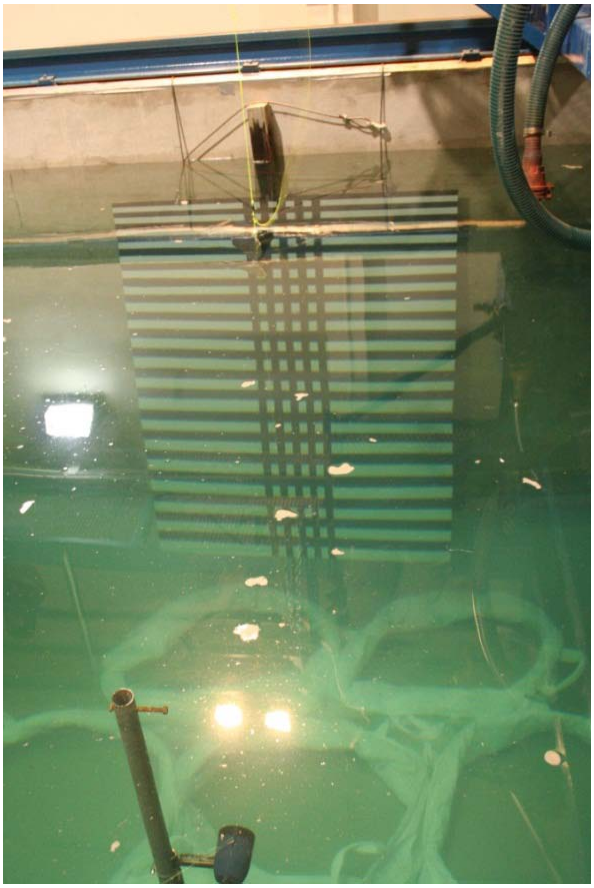

Figure 29. Free Fall Testing Background Board and Camera.

Free Fall Testing Procedure

The procedure for the free fall testing was as follows:

1. Set-up anchor for the specified test
2. Fasten the loop on the monofilament line to the loop on the nylon line tied on the swivel on rear of the anchor
3. Clip the other end of the monofilament line into chained carabineer
4. Lower the anchor using the nylon recovery line looped around the capstan winch until the monofilament line takes the weight of the anchor

5. Position the recovery line for deployment
6. Using chain, lower the anchor until the rear tail fins are slightly beneath the water surface
7. Using the boat hook, steady the anchor into a stationary state and position the mooring arm towards the East or West direction
8. Begin recording on the underwater video cameras
9. Toss the recovery line onto the surface on the water in such a way to prevent entanglement
10. Using the butane lighter to burn the monofilament line, releasing the anchor
11. Stop recording on the underwater video cameras
12. Fish recovery line using the boat hook
13. Recover the anchor using the capstan winch

RESULTS AND DISCUSSION

The model testing performed on the OMNI-Max anchor produced quality data with limited costs. The penetration depth was sufficient enough for the anchor to be buried entirely, the tow testing provided quality drag force measurements and the free fall testing results showed the anchor reached terminal velocity. Table 3 depicts the values used for calculations with reference to each model anchors' mooring arm being in-line with the upper and lower fins. Table 4 highlights the physical parameters used for calculations with each model anchors' mooring arm being between the upper and lower fins. Table 5 summarizes the physical properties of the mooring ropes utilized during testing. An image of both ropes is presented as Figure 30. It should be noted that the yellow mooring rope was placed in its natural state for Figure 30 and not tailored to create bends.

Table 3. Model Anchor Specifications with Mooring Arm In-Line with Fins.

Item	Surface Area (in^2)			Frontal Area (in^2)		
	Fully Extended	Middle Setting	Fully Retracted	Fully Extended	Middle Setting	Fully Retracted
1/24 Scale Anchor	162.33	154.71	146.56	6.51	6.41	6.29
1/15 Scale Anchor	475.97	458.38	439.73	13.55	13.34	13.09

Table 4. Model Anchor Specifications with Mooring Arm between Fins.

Item	Surface Area (in^2)			Frontal Area (in^2)		
	Fully Extended	Middle Setting	Fully Retracted	Fully Extended	Middle Setting	Fully Retracted
1/24 Scale Anchor	162.33	154.71	146.56	6.83	6.73	6.60
1/15 Scale Anchor	475.97	458.38	439.73	14.21	14.00	13.73

Table 5. Model Mooring Rope Specifications.

Item	Material	Length (ft)	Width (in)	Dry Weight (lbf)	Wet Weight (lbf)	Buoyant Force (lbf)
White Mooring Rope	Braided Cotton	22.5	$^1/_4$	0.583	0 (Floated)	0.583
Yellow Mooring Rope	Braided Plastic	7	$^3/_8$	0.083	0 (Floated)	0.083

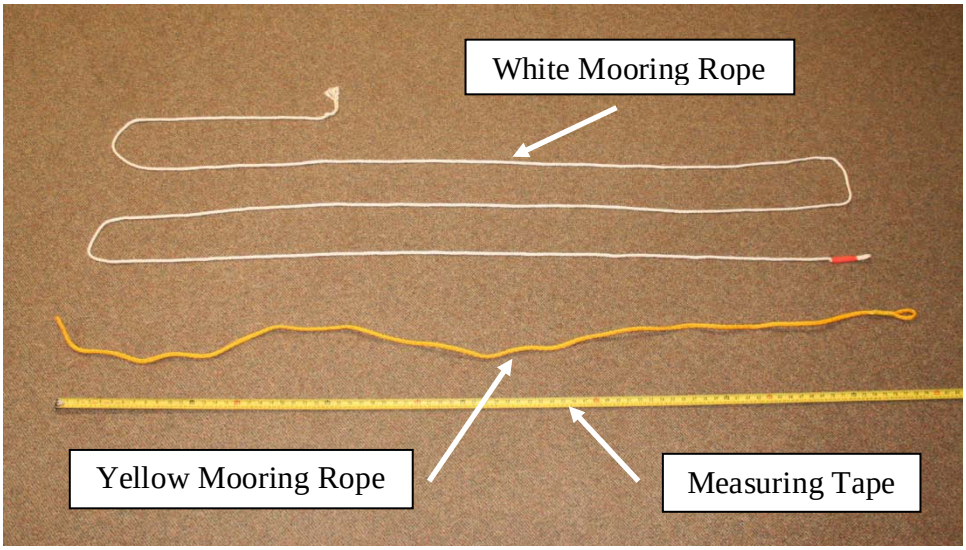

Figure 30. Model Ropes Used During Testing.

The fluid used during testing was fresh water. The physical properties of the water which relate to anchor testing are summarized in Table 6.

Table 6. Fluid Properties.

Property	Model Testing Values	Expected Prototype Values
Density (slugs/ft^3)	1.94	1.99
Water Temperature (Fahrenheit)	70	60
Kinematic Viscosity (ft^2/s)	0.00001052	0.0000126

Soil Penetration Testing

Soil Penetration Testing Results

The 1/24 scale model OMNI-Max anchor was utilized for penetration depth testing. The anchor fully penetrated into the mud for each test. Tests are related by the fin setting, mooring arm position, and are referred to as a test "case" where each case has an initial and repeated test. The fin position, release height, and mooring arm position were varied and defined for each test case to evaluate penetration depth (D_P). Figure 31 shows an image of the anchor just before release and the recovery rope. Figure 32 shows an image of a typical crater created by the anchor.

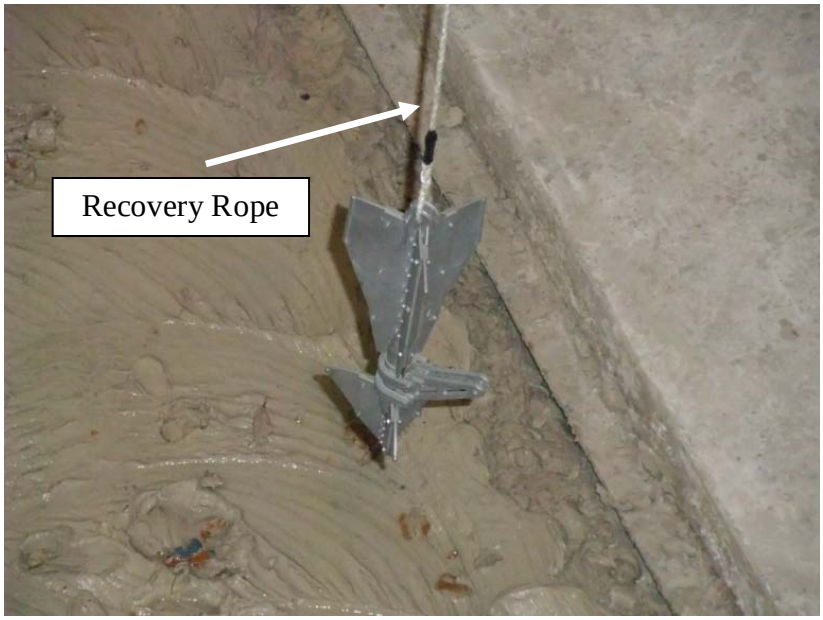

Figure 31. OMNI-Max Anchor (1/24 Scale) Just Before Soil Penetration Test.

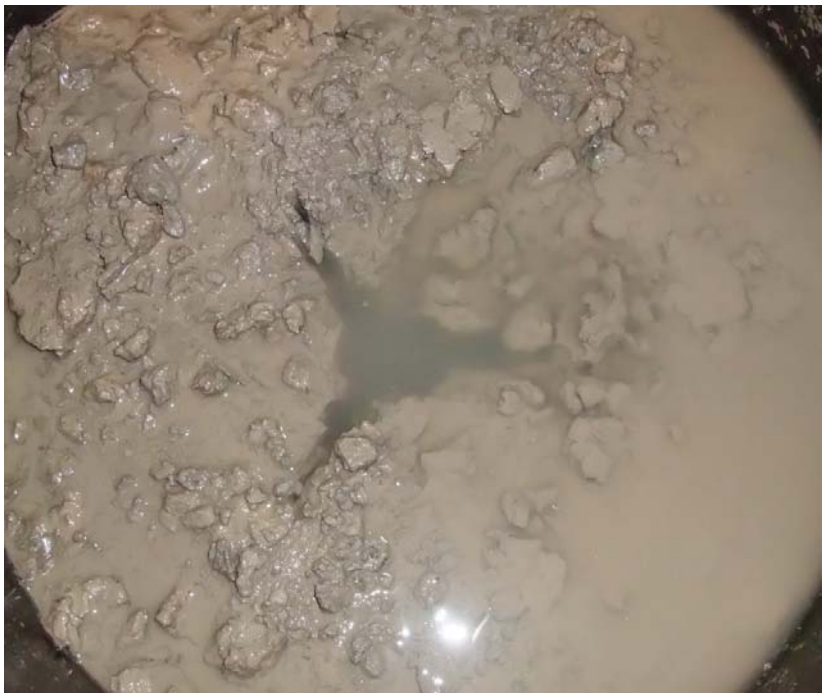

Figure 32. Typical Impact Crater After Anchor is Removed.

The first group of test cases investigated the relationship between the anchor release height and subsequent penetration depth. Tests 1, 2, and 3 were referred to as "Case A" and involved the anchor fins being set into the fully extended position and the mooring arm placed in-line with the fins, while being released from 4 ft above the mudline. Tests 4, 5, and 6 were referred to as "Case B" and placed the anchor fins in the fully extended position and the mooring arm between the fins, while being released from 4 ft above the mudline. Tests 7, 8, and 9 were referred to as "Case C" and were repeats of the test conditions of 4, 5, and 6 with the exception of the anchor being released 6 ft above the mudline. Tests 10, 11, and 12 were referred to as "Case D" with the anchor being placed in the same settings as tests 4, 5, and 6. However, the release height was increased to 8 ft above the mudline. Tests 2 and 3 were repetitions of test 1, tests 5 and 6 were repetitions of test 4, tests 8 and 9 were repetitions of test 7, and tests 11 and 12 were repetitions of test 10.

The second group of test cases investigated the relationship between fin position and penetration depth. Tests 13 and 14 were referred to as "Case E" and involved the anchor fins being set into the middle position while the mooring arm was placed in-line with the fins. Tests 15 and 16 were referred to as "Case F" required the fins set into the middle setting, but the mooring arm was placed between the fins. Tests 17 and 18 were referred to as "Case G" called for the fins to be placed in the fully retracted position and the mooring arm placed in-line with the fins. Finally, tests 19 and 20 were referred to as "Case H" and specified the fins to be placed in the fully retracted setting and the mooring arm placed between the fins. Tests 13 through 20 were conducted at a 4 ft

release height above the mudline and involved one repetition for each case. Table 7 summarizes the test case conditions.

Table 7. Soil Penetration Testing - Test Descriptions.

Case	Test	Release Height (ft)	Lower Fins			Upper Fins			Mooring Arm Position	
			Fully Extended	Middle Setting	Fully Retracted	Fully Extended	Middle Setting	Fully Retracted	In-Line with Fins	Between Fins
A	1	4	X			X			X	
	2	4	X			X			X	
	3	4	X			X			X	
B	4	4	X			X				X
	5	4	X			X				X
	6	4	X			X				X
C	7	6	X			X				X
	8	6	X			X				X
	9	6	X			X				X
D	10	8	X			X				X
	11	8	X			X				X
	12	8	X			X				X
E	13	4		X			X		X	
	14	4		X			X		X	
F	15	4		X			X			X
	16	4		X			X			X
G	17	4			X			X	X	
	18	4			X			X	X	
H	19	4			X			X		X
	20	4			X			X		X

The penetration depths of each test case were averaged. This averaging was justified because each test was performed within close proximity to the other tests within their corresponding case. The justification for performing the close proximity was to minimize variations of undrained shear strength (S_U) affecting the penetration resistance experienced by the anchor. For instance, if the mud were slightly stronger (a higher S_U) in one test resulting in a lower penetration depth, the averaged penetration depth would

be skewed and penetration depth comparisons would be affected. The S_U of the mud was measured using T-bar tests and the locations of the tests are seen in Figure 33.

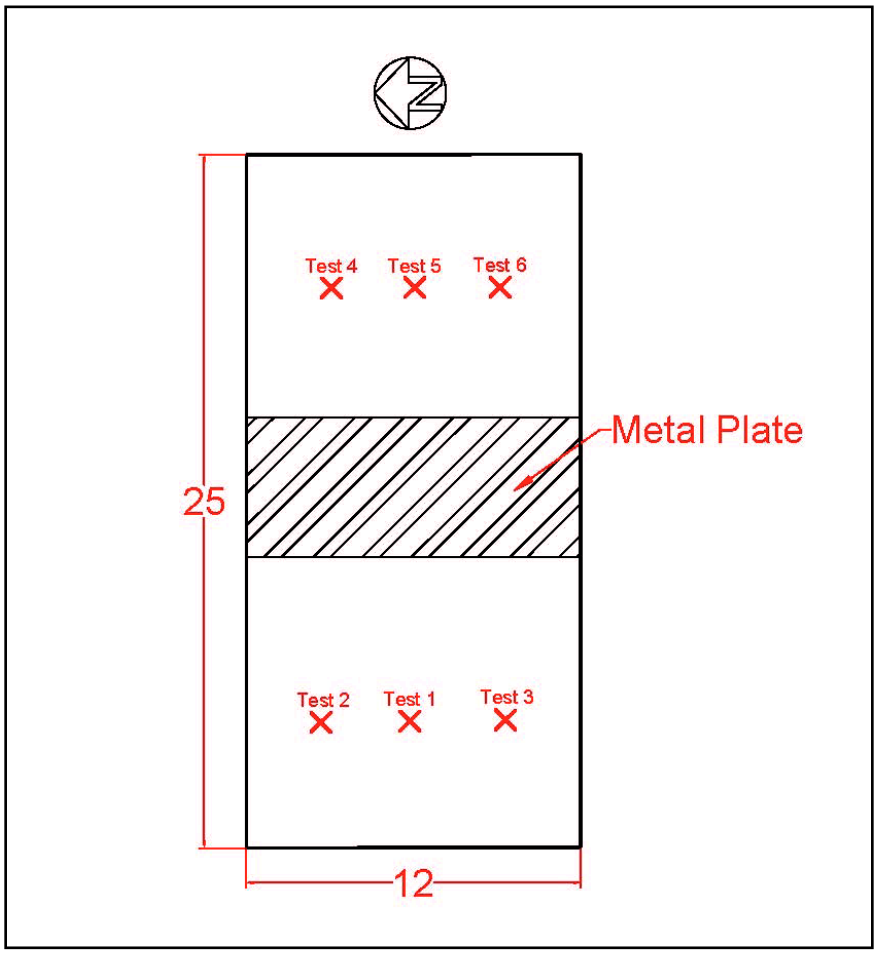

Figure 33. T-bar Test Locations in Sediment Pit (Dimensions in Feet).

The T-bar was lowered into six locations around the sediment pit and the force measurements were recorded as a function of the depth. The T-bar was lowered at a constant rate of 0.025 ft/s while obtaining measurements at a rate of 25 Hz. The force measurements were then converted to S_U as a function of depth using Equation (14). A

bar factor of 10.5 and the T-bar cylindrical area of 0.2947 ft^2 were implemented into Equation (14). The results of the testing may be seen as Figure 34.

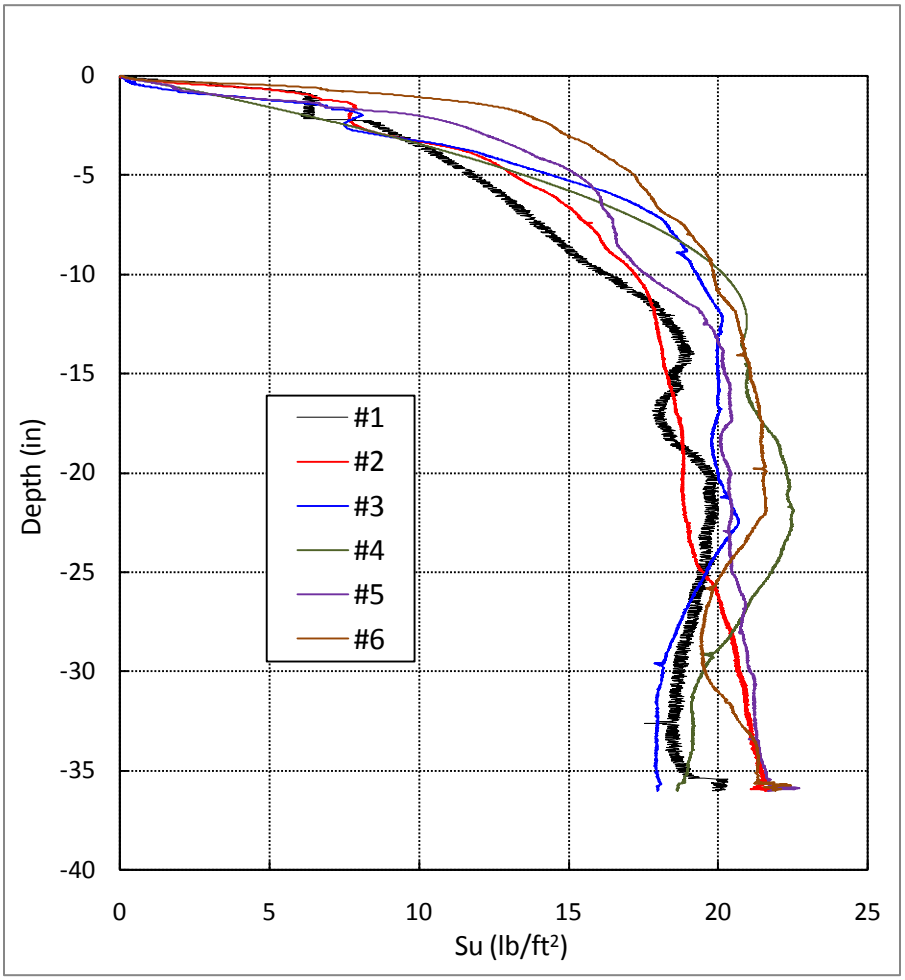

Figure 34. T-bar Testing Results - Undrained Shear Strength as a Function of Depth.

The T-bar testing results show a high increase in S_U from the mudline to approximately 4 in beneath the mudline for all test locations. This increase is attributed to the cylinder beginning to be immersed into the mud and measuring no force to

measuring relatively substantial force. After the cylinder is fully immersed at approximately 4 in, S_U increases at a slightly slower rate due to the consolidation of the mud. After around 10 in of depth, S_U stays relatively constant until 3 ft (36 in) beneath the mudline, where the test finishes. The cause of the undrained shear strength gradient being high above the 10 in depth is due to the mud being mixed before the anchor and T-bar testing began. The mixing disturbed the consolidation process and homogenized the undrained shear strength of the mud below a depth of 10 in. This is highlighted in Table 8 and Table 9 where an incremental difference in S_U is divided by the corresponding depth to find the undrained shear strength gradients (G_{Su}). Because of the high variability of G_{Su}, a relationship between the penetration depth and the G_{Su} of the soil was investigated for the model testing.

Table 8. Undrained Shear Strength Gradients - T-bar Test Locations 1, 2, & 3.

Depth (in)	T-bar Test 1			T-bar Test 2			T-bar Test 3		
	S_U	Difference	G_{Su}	S_U	Difference	G_{Su}	S_U	Difference	G_{Su}
0-3	9.36	9.36	37.5	8.92	8.92	35.7	8.71	8.71	34.8
3-6	12.92	3.56	14.2	14.42	5.49	22.0	16.53	7.82	31.3
6-9	15.33	2.41	9.6	16.48	2.06	8.2	18.78	2.25	9.0
9-12	17.96	2.63	10.5	17.89	1.41	5.7	20.12	1.35	5.4
12-15	18.65	0.70	2.8	18.30	0.41	1.6	19.98	-0.15	-0.6
15-18	18.49	-0.17	-0.7	18.80	0.51	2.0	19.82	-0.16	-0.6
18-21	19.48	1.00	4.0	18.80	-0.01	0.0	20.23	0.42	1.7
21-24	19.41	-0.07	-0.3	19.19	0.40	1.6	19.97	-0.27	-1.1
24-27	19.38	-0.03	-0.1	20.17	0.98	3.9	18.85	-1.11	-4.5
27-30	18.54	-0.84	-3.4	20.69	0.52	2.1	18.14	-0.71	-2.9
30-33	18.57	0.03	0.1	21.09	0.40	1.6	17.94	-0.20	-0.8
33-36	19.85	1.28	5.1	21.56	0.47	1.9	17.98	0.04	0.2

Table 9. Undrained Shear Strength Gradients - T-bar Test Locations 4, 5, & 6.

Depth (in)	T-bar Test 4			T-bar Test 5			T-bar Test 6		
	S_U	Difference	G_{Su}	S_U	Difference	G_{Su}	S_U	Difference	G_{Su}
0-3	8.92	8.92	35.7	12.25	12.25	49.0	14.96	14.96	59.8
3-6	15.39	6.46	25.9	16.02	3.77	15.1	17.69	2.73	10.9
6-9	19.39	4.00	16.0	16.89	0.87	3.5	19.62	1.93	7.7
9-12	20.93	1.54	6.2	19.46	2.57	10.3	20.58	0.96	3.9
12-15	20.98	0.05	0.2	20.21	0.75	3.0	21.07	0.49	2.0
15-18	21.75	0.77	3.1	20.10	-0.11	-0.4	21.47	0.40	1.6
18-21	22.32	0.57	2.3	20.34	0.24	1.0	21.56	0.09	0.4
21-24	22.09	-0.22	-0.9	20.40	0.06	0.2	20.62	-0.94	-3.8
24-27	20.88	-1.21	-4.9	20.86	0.47	1.9	19.59	-1.03	-4.1
27-30	19.50	-1.38	-5.5	21.07	0.21	0.8	19.54	-0.05	-0.2
30-33	19.16	-0.34	-1.4	21.28	0.21	0.8	20.96	1.41	5.7
33-36	18.65	-0.51	-2.0	21.67	0.39	1.6	21.91	0.96	3.8

The nearest T-bar test location was noted for each anchor test case. A simple average of S_U was taken from the mudline to the depth where the anchor tip penetrated. G_{Su} was then calculated by taking that average and dividing by the penetration depth in ft. This value represents the average force of resistance experienced during penetration. Calculation of G_{Su} is seen in Equation (24).

$$G_{Su} = \frac{\sum_{Mudline}^{D_P} S_U}{\frac{n}{D_P}} \tag{24}$$

where n is the amount of S_U measurements from the mudline to D_P. This is a reasonable assessment because if the anchor penetrates deeper into the mud, a high D_P decreases G_{Su}, which signifies a lower averaged value of S_U, which allows higher penetrations. In addition, if the D_P was low, then G_{Su} increases, signifying a high S_U for the soil which is

better at resisting penetration. It should be noted that resources pertaining to nonlinear shear strength gradients are extremely limited and require further research.

Table 10. Soil Penetration Testing – Test Results.

Case	Test	A_F (in^2)	Nearest T-bar Test	G_{Su} (psf/ft)	D_P (in)	$\overline{D_P}$ (in)
A	1	5.96	2	8.48	21.50	21.75
	2				22.75	
	3				21.00	
B	4	6.28	2	9.03	21.00	20.08
	5				19.75	
	6				19.50	
C	7	6.28	3	8.60	24.75	23.67
	8				23.50	
	9				22.75	
D	10	6.28	3	7.49	26.50	27.75
	11				27.75	
	12				29.00	
E	13	5.87	1	8.86	19.75	19.75
	14				19.75	
F	15	6.19	1	8.68	20.50	20.38
	16				20.25	
G	17	5.74	4	10.19	19.50	19.63
	18				19.75	
H	19	6.06	4	10.36	19.50	19.13
	20				18.75	

Table 10 summarizes the results of the soil penetration testing of the OMNI-Max anchor. The average tip penetration of each case was plotted against its corresponding undrained shear strength gradient and is shown as Figure 35. A 2nd order polynomial trend line was fit to the data and produced Equation (25) with a reasonably high R^2 value of 0.89.

$$D_P = 1.55G_{Su}{}^2 - 30.67G_{Su} + 170.4 \quad (25)$$

The differences between Equation (25) and Equation (15) are the coefficients that fit the line to the data. This is attributed to the difference in surface S_U and G_{Su} encountered in the Gulf of Mexico mud and the artificial, laboratory mud. Equation (15) also predicts the penetration depth by feet, which influences the coefficients. However, both equations show that as G_{Su} decreases, the penetration depth increases. It should be noted that both the prototype and model penetrated about 1.5 anchor lengths, justifying scalability.

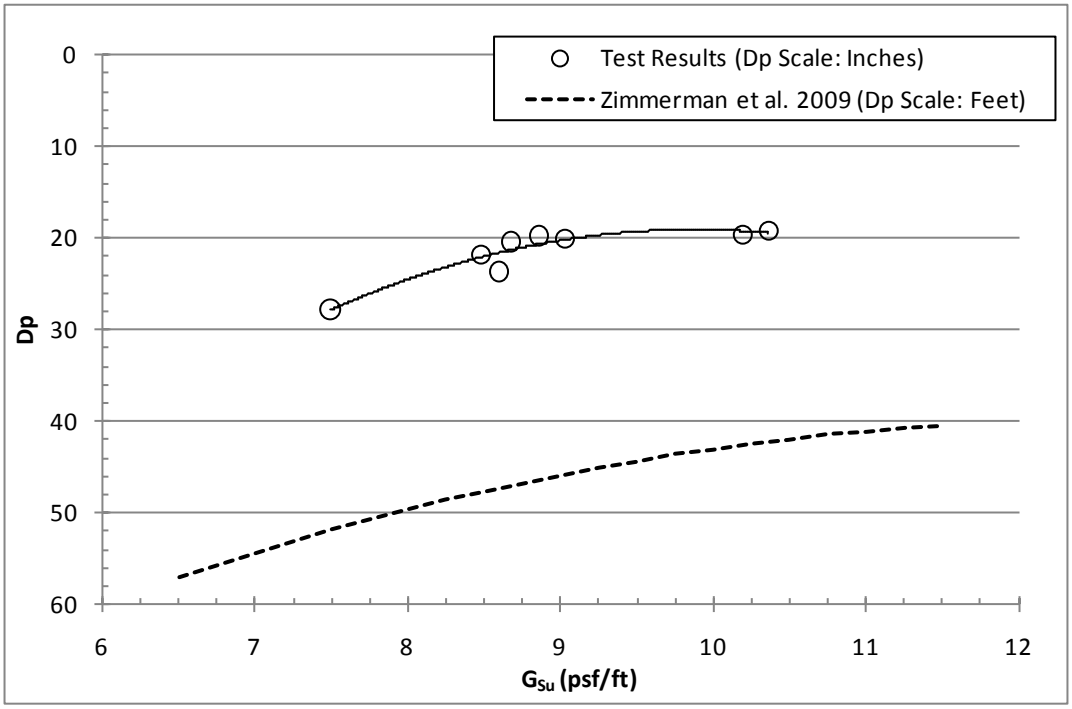

Figure 35. Penetration Depth as a Function of Undrained Shear Strength Gradients.

The results also confirm relationships between the fin position, mooring arm position, and release height with the penetration depth. The most apparent relation is the

increase in penetration depth as release height is increased. Case B, C, and D placed the anchor fins in the fully extended position and the mooring arm between the fins. The cases also occurred within close proximity in the sediment pit, which negates influences caused by differences in G_{Su}. The penetration depth increased 15.1% and 14.7% when the height was increased by 33% and 25%, respectively. These increases in D_P are due to the increased impact velocity, because the anchor had more time to accelerate with gravity. Preliminary model anchor testing resulted in estimating that the terminal velocity of the model anchor was obtained from a release height around 22 ft above the mudline. Therefore, terminal velocity was not reached for cases B, C, and D. The impact velocity was estimated by neglecting drag and buoyancy when the anchor is falling through the air. A plot of the testing penetration depths as a function of impact velocity is shown in Figure 36.

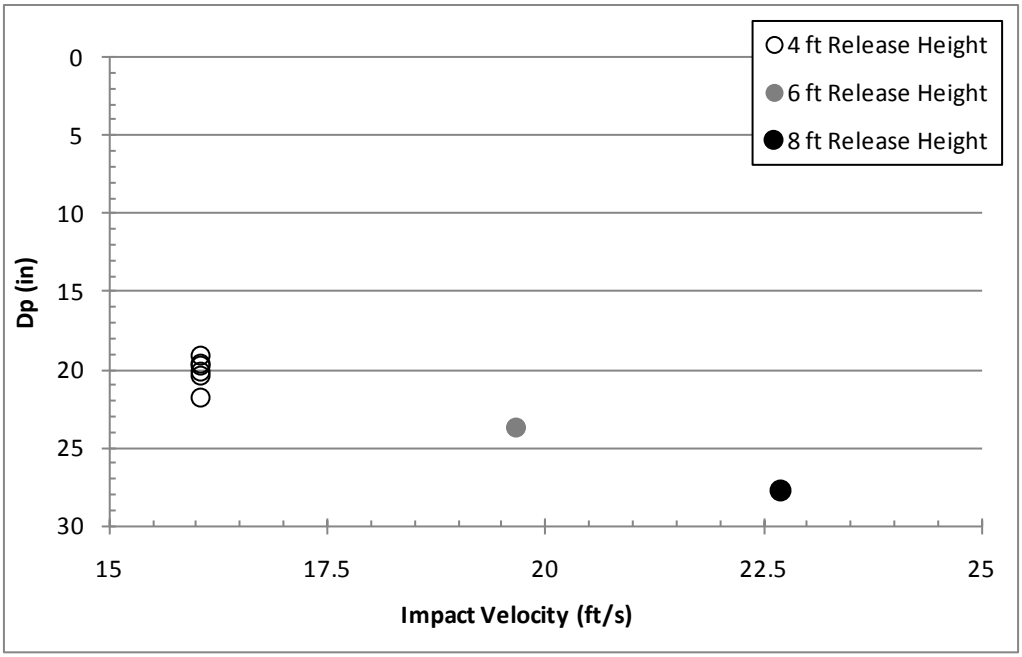

Figure 36. Penetration Depth as a Function of Impact Velocity.

There is a slight relation between fin position and mooring arm position with penetration depth. The penetration depth decreased 7.6% when the mooring arm was moved from I/L to B/T, with the fins fully extended. However, D_P increased 3.1% when the mooring arm was moved from I/L to B/T, with the upper and lower fins placed in the middle setting. Penetration depth decreased 2.5% when the mooring arm was changed from in-line to between the fins when the fins were placed in the fully retracted position. Therefore, the mooring arm position only affects the penetration depth an average of 4.4%, which is on the order of less than a third of anchor length. This leads to the conclusion that the mooring arm position is negligible in terms of penetration depth.

The fin position also appears to have a slight influence on penetration depth. When the mooring arm was placed between the fins, the penetration depth increased

1.4% and decreased 6.1% when the fins were switched from fully extended to the middle setting and then from the middle setting to fully retracted, respectively. However, when the mooring arm was placed in line with the fins, the penetration depth decreased 9.2% and 0.6% when the fins were placed into the middle setting from fully extended, and then set into the fully retracted setting from the middle setting, respectively. Therefore, the observed trend is that penetration depth decreases as the fins are retracted. This is interesting because a lower frontal area means a lower resistance force encountered by the anchor calculated by Equation (12), resulting in theoretically higher penetration depths. When relating the range of variation in penetration depths to model anchor length, the effects due to fin position on penetration depth are less than 20% of the model anchor length, which is relatively small. Therefore, fin position affects the penetration depth by at most 3 in for the model anchor and 6.6 ft for prototype anchors as shown in Figure 37.

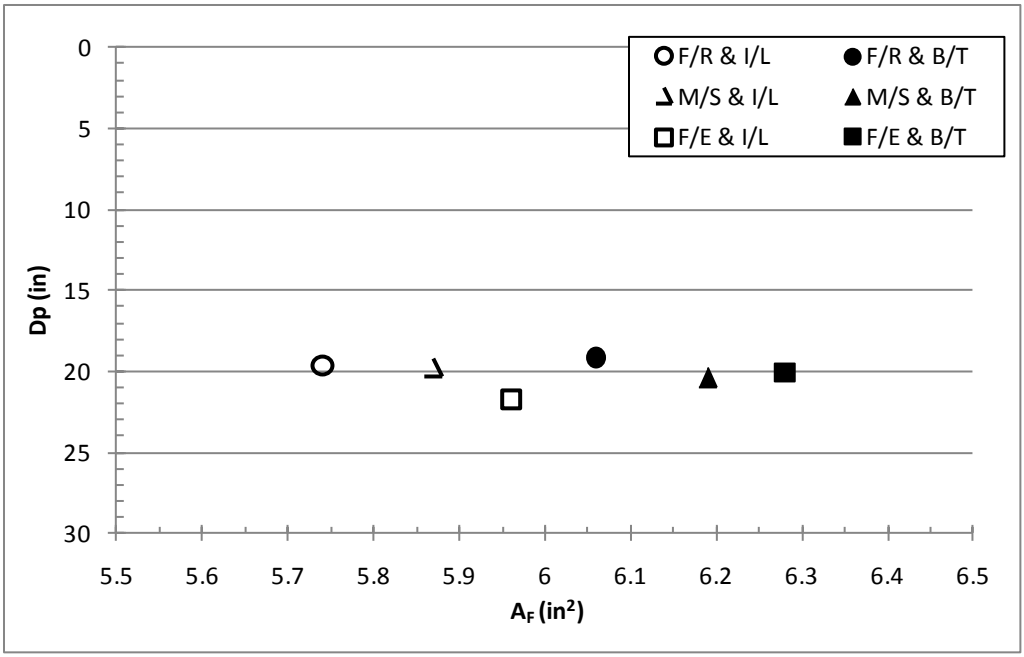

Figure 37. Penetration Depth as a Function of Fin Setting and Mooring Arm Position.

Soil Penetration Testing Discussion and Experimental Error

The penetration testing showed fairly consistent effects of fin position, mooring arm position, and release height on overall penetration depth. The testing showed that the mooring arm position slightly affected the penetration depth by increasing D_P when the arm was moved from in-line with the fins to between the fins. The results of the testing also indicate that the fin position marginally increased D_P when the fins were varied from the fully extended position to fully retracted position. Finally, the penetration depth increased when release height was increased.

However, a few sources of experiential error have been considered. The first source of some error being that the artificial mud mixture was not completely homogeneous throughout the sediment pit. This is significant when the different settings

on the anchor have a range of the frontal area from 6.83 in^2 to 6.29 in^2 and a range in surface area from 162.33 in^2 to 146.56 in^2, a difference of 7.9% and 9.7%, respectively. Because the anchor geometry changes less than 10%, to investigate the anchors shape effect on penetration depth is difficult when the testing mud is not perfectly homogeneous.

A second possible source of error is the precision of the measurements taken for penetration depth. After each anchor test was completed, the recovery line, which protruded from the impact crater, was used as a gauge for penetration depth. The mudline "plane" was noted on the recovery line and the distance between the upper fins' trailing edges and the mudlines' intersection with the line was measured with 0.25 inch precision. Since the range of D_P was only a few inches for the same release height, the lack of high precision measurements might have missed some effects.

A third source of error is judging where the mudline intersection occurred with the recovery rope. The anchor creates an impact crater with slight ridges formed around the hole caused by displaced mud. Therefore, the intersection of the pre-test mudline and the recovery rope is dependent on human judgment. To minimize the inherent error associated with human judgment, the same person recovered and measured the amount of penetration after each test.

As with all experimental testing, there is room for improvement to enhance accuracy of the tests. The first recommendation was to homogenize the testing mud by thorough, complete mixing. Therefore, any differences in penetration depth would be a result of anchor geometry and not a result of varying resistive mud forces. The second

recommendation was to develop a more precise measurement tool which could be placed on the mud surface and measure the distance to a point on the penetrated anchor. The third recommendation is to increase the quantity of tests. Test cases with one or two repetitions are somewhat inconclusive with so many variables inherent with studies involving mud. Increasing the repetitions to 10 or 12, though tedious, improves confidence in the results while increasing testing time and costs. A fourth recommendation is to increase the release height, incrementally, for each differing anchor setting, which would result in a better sense of anchor performance with respect to penetration depth.

Tow Testing

Tow Testing Results

The 1/15 model scale OMNI-Max anchor was utilized for tow testing. The testing investigated the relationship between anchor geometry, rope attachments, and drag coefficient. The fin settings, tow velocity, and mooring arm position were varied, as well as the inclusion of a rope on the mooring arm was tested. The towing tests were clustered into three major groups defined by upper and lower fin position; fully extended, middle setting, and fully retracted. Each of these groups had four distinct categories defined by mooring arm position and the addition of a rope on the mooring arm; the mooring arm in-line with the fins, with or without mooring rope, or the mooring arm between the fins, with or without mooring rope. Each category was evaluated with 6 different velocities ranging from 1.73 fps to 6.55 fps. An additional, repetitive test was performed for each velocity except for 1.73 fps because it was such a slow velocity that

a repetitive, accurate measurements could not be taken. This is due to the low signal to noise ratio exhibited during this velocity. The signal is defined as the drag force acting on the anchor via an induced voltage transmitted by the force transducer and the noise being fluctuations in voltage due to carriage vibrations and force transducer sensitivity. A description of each test case is outlined in Table 11.

Table 11. Tow Testing - Test Descriptions.

Test	Lower Fins			Upper Fins			Mooring Arm Position		Attachments
	Fully Extended	Middle Setting	Fully Retracted	Fully Extended	Middle Setting	Fully Retracted	In-Line with Fins	Between Fins	
1	X			X			X		-
2	X			X				X	-
3	X			X			X		Mooring Rope
4	X			X				X	Mooring Rope
5		X			X		X		-
6		X			X			X	-
7		X			X		X		Mooring Rope
8		X			X			X	Mooring Rope
9			X			X	X		-
10			X			X		X	-
11			X			X	X		Mooring Rope
12			X			X		X	Mooring Rope

For each velocity case, the carriage performed three tow tests with only the stinger attached to the testing rig, for a total of 18 test runs. These preliminary runs measured the drag force associated with the stinger and lower portion of the test rig,

which was eventually subtracted from the measured drag force during the actual test run. Figure 38 shows the stinger connecting the anchor to the tow testing rig. The difference was the drag force directly due to the anchor. Measurements of voltage through the Mx channel were taken as a function of time by the force transducer. The time-series of measurements had a repetitive pattern involving the acceleration, constant speed, and deceleration period. An example of the measurement time-series is shown in Figure 39.

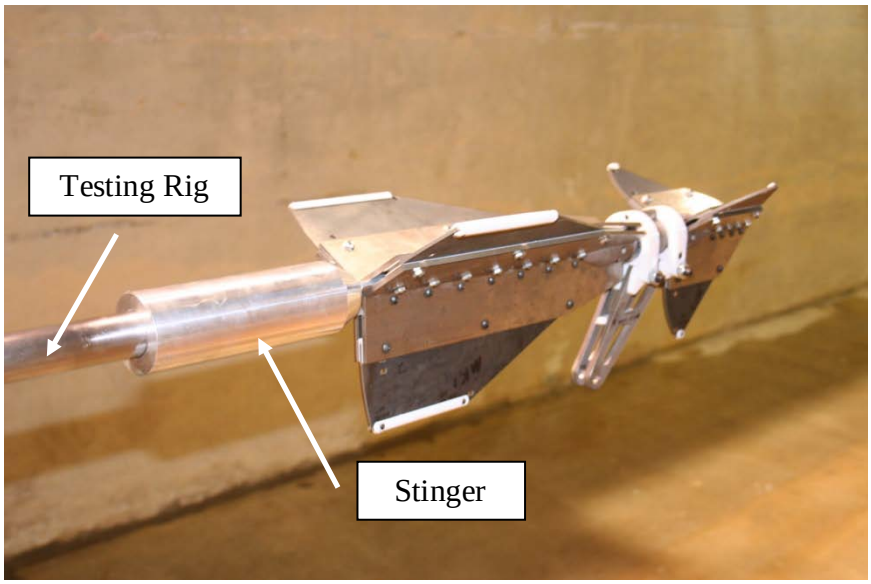

Figure 38. Stinger and Testing Rig Used in Towing Tests.

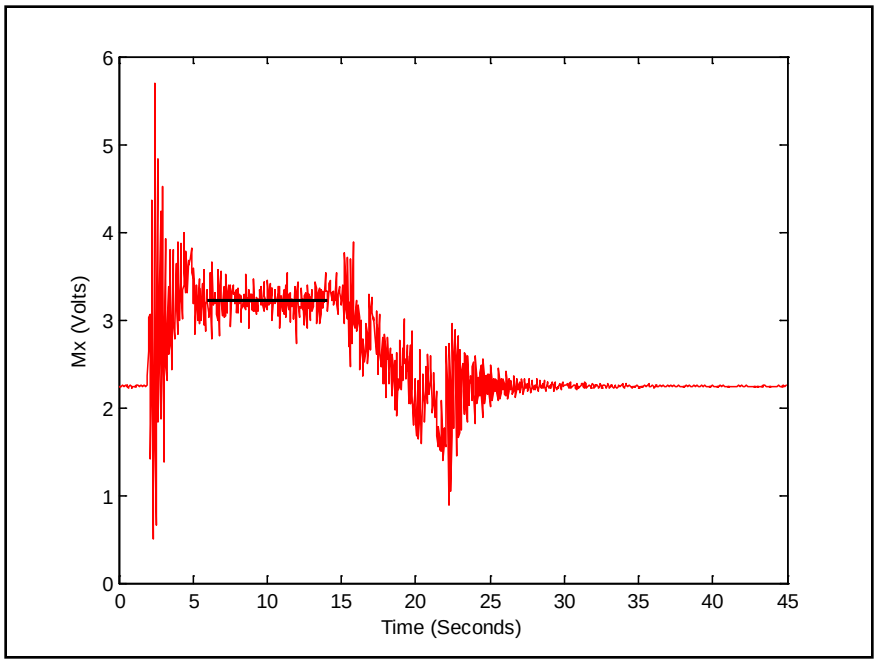

Figure 39. Typical Mx Time-Series for 5.01 fps Tow Test.

An average of the voltage readings was taken during the constant speed period, which is represented by the black line starting at 6 s and ending at 14 s for Figure 39. The acceleration period is signified by the large amplitude spike before the constant velocity period, while the deceleration period is marked by the next substantial spike of voltage before the readings begin to decrease. Once the carriage stops, a decaying resonant period of voltage appears resulting from the oscillatory motion of the testing rig due to momentum. The measurements were taken at a rate of 25 Hz and test runs were recorded for 45 s. Typical plots for an Mx time-series measurement for the remaining five velocities are presented as Figure 40 through Figure 44.

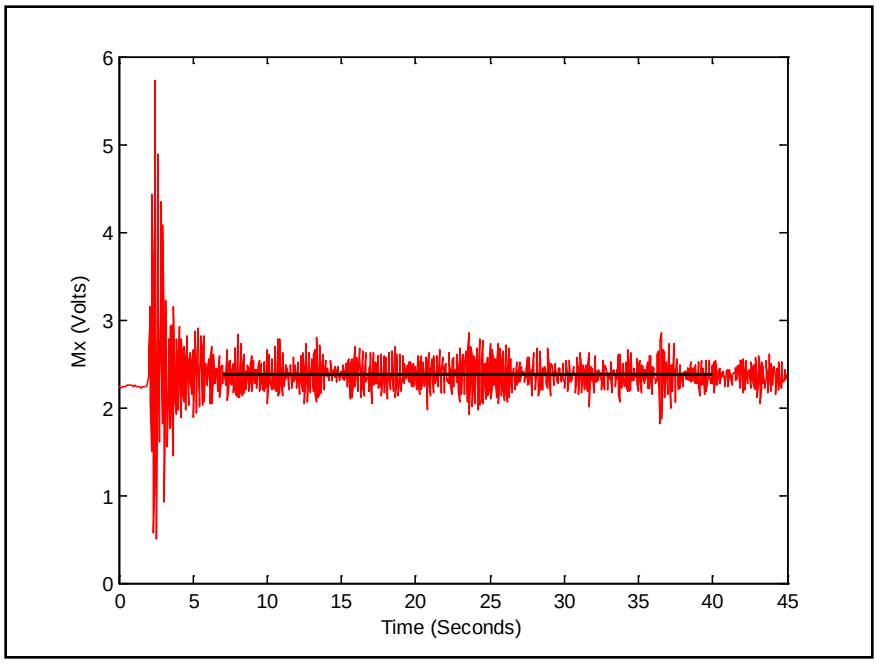

Figure 40. Typical Mx Time-Series for 1.73 fps Tow Test.

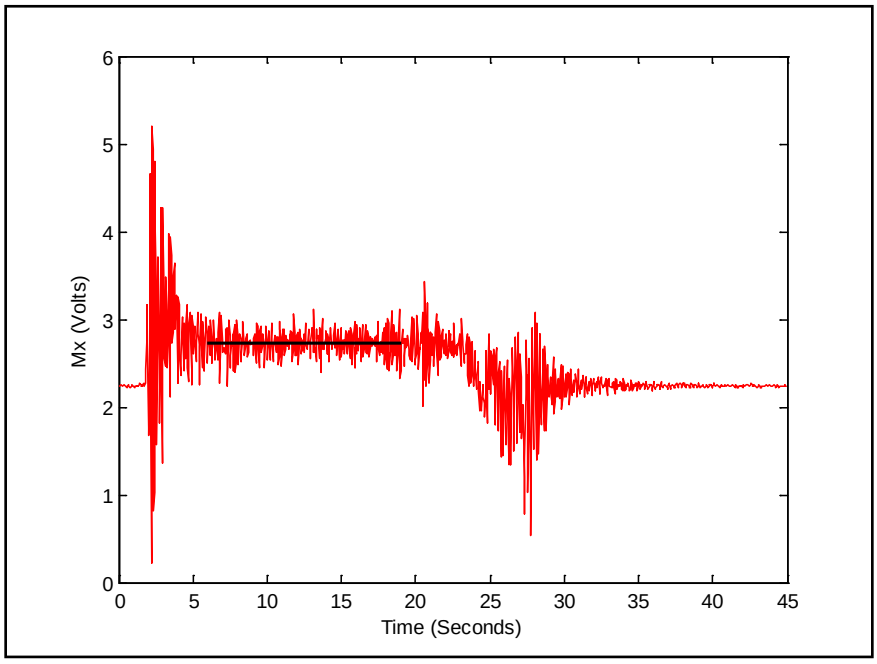

Figure 41. Typical Mx Time-Series for 3.41 fps Tow Test.

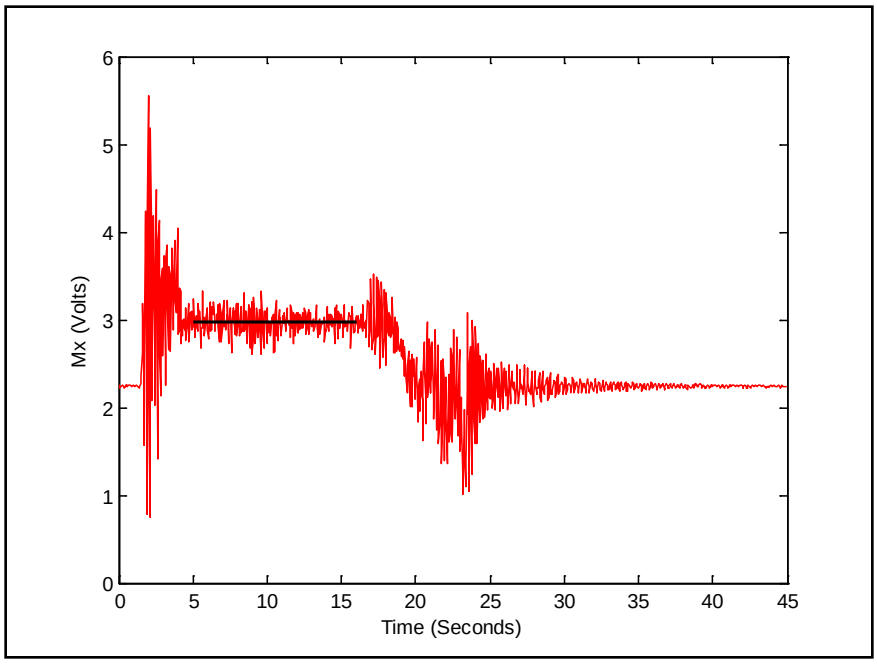

Figure 42. Typical Mx Time-Series for 4.21 fps Tow Test.

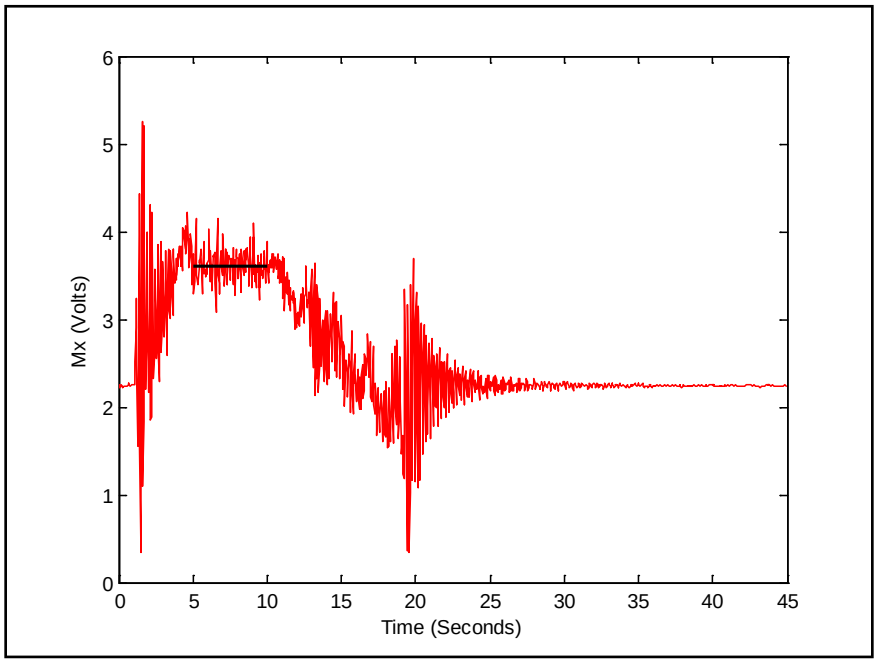

Figure 43. Typical Mx Time-Series for 5.91 fps Tow Test.

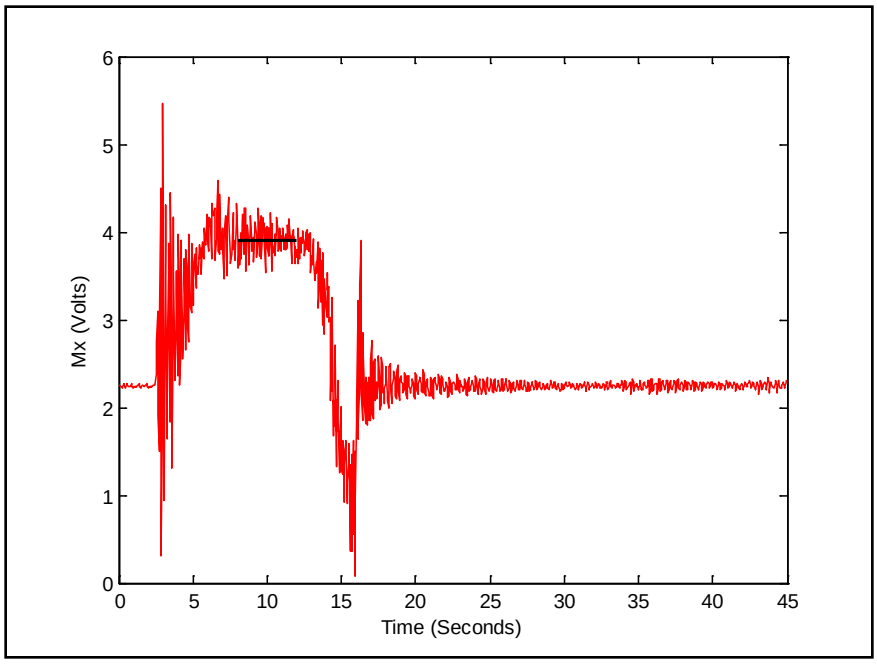

Figure 44. Typical Mx Time-Series for 6.55 fps Tow Test.

Once these averages were recorded and subtracted from the corresponding averages for the stinger and lower section of the testing rig, the resulting voltage required conversion into a moment. The voltage to moment conversion rate was obtained with calibration of the force transducer for moment about the X-axis defined on the force transducer. This was achieved by placing a shackle of a known weight on the counter-weight of the lower section of the test rig. A plot of the recordings is presented as Figure 45, and a linear trend line was fit to the voltage measurements of the Mx channel. Equation (26) is the calibration equation, with a R^2 value of 0.999, used to convert voltages to moments. The shackle was placed along the counterweight in 6 in increments and the voltages of all six channels of the transducer were recorded. An image taken during calibration is presented as Figure 46.

$$Mx = 0.0211(V) - 0.0036 \quad (26)$$

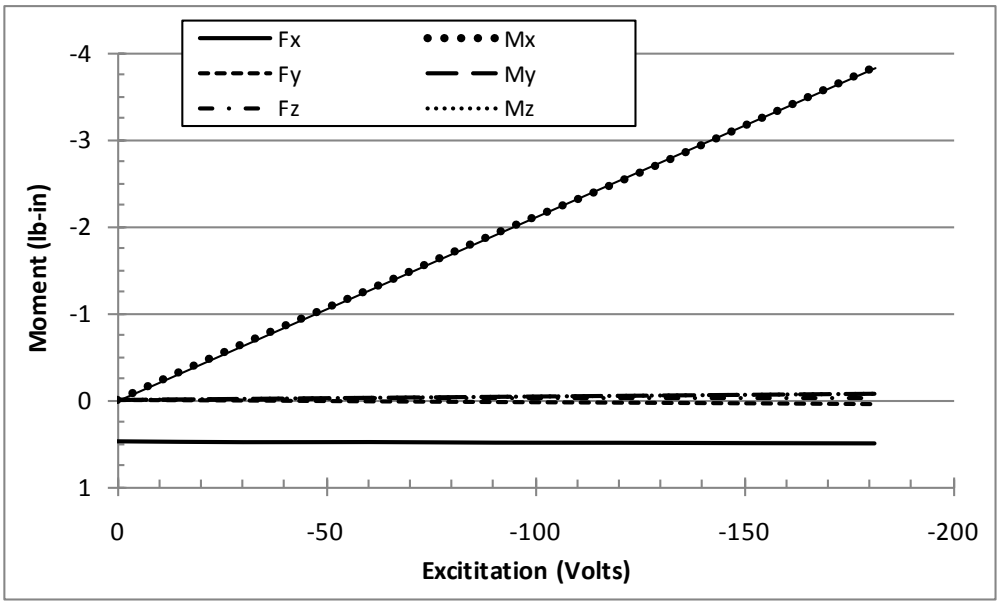

Figure 45. Calibration of Force Transducer for Tow Testing.

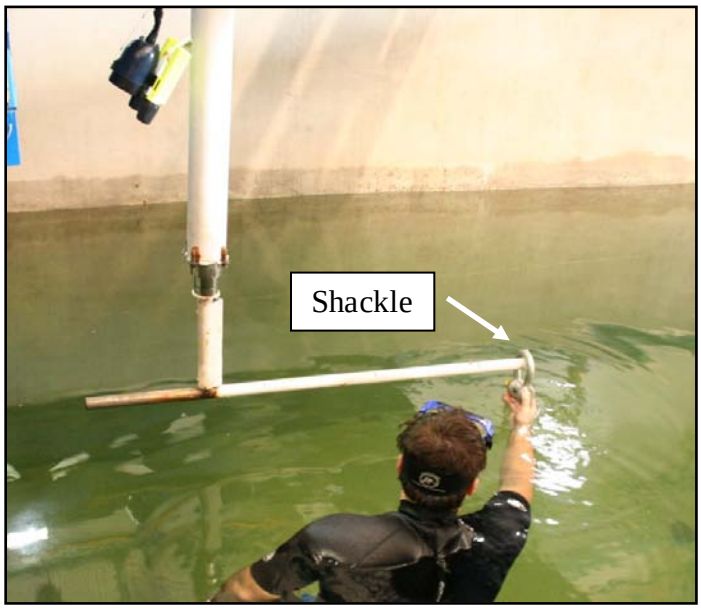

Figure 46. Calibration of Tow Testing Force Transducer.

Once the moment due to drag force was calculated, the known distance from centerline of the anchor to the effective center of the force transducer is divided into the Mx to determine drag force. Therefore, Equation (19) was implemented to calculate the drag coefficient. The results are summarized in Table 12.

Table 12. Tow Testing - Test Results.

Test	V_C (fps)	Re	A_F (in^2)	F_D (lb)	C_D
1	1.73	3.08E+05	13.55	0.12	0.45
	3.41	6.08E+05		0.85	0.80
	4.21	7.51E+05		1.52	0.94
	5.01	8.93E+05		2.12	0.93
	5.95	1.06E+06		3.05	0.94
	6.55	1.17E+06		3.54	0.91
2	1.73	3.08E+05	14.21	0.16	0.58
	3.41	6.08E+05		0.77	0.69
	4.21	7.51E+05		1.27	0.75
	5.01	8.93E+05		1.74	0.73
	5.95	1.06E+06		2.50	0.74
	6.55	1.17E+06		3.01	0.73
3	1.73	3.08E+05	13.55	0.27	1.00
	3.41	6.08E+05		1.09	1.03
	4.21	7.51E+05		1.78	1.10
	5.01	8.93E+05		2.47	1.08
	5.95	1.06E+06		3.37	1.04
	6.55	1.17E+06		4.06	1.04
4	1.73	3.08E+05	14.21	0.22	0.78
	3.41	6.08E+05		0.91	0.82
	4.21	7.51E+05		1.41	0.83
	5.01	8.93E+05		2.07	0.86
	5.95	1.06E+06		2.92	0.86
	6.55	1.17E+06		3.41	0.83
5	1.73	3.08E+05	13.34	0.16	0.59
	3.41	6.08E+05		0.90	0.87
	4.21	7.51E+05		1.48	0.93
	5.01	8.93E+05		2.25	1.00
	5.95	1.06E+06		3.26	1.02
	6.55	1.17E+06		3.92	1.02
6	1.73	3.08E+05	14.00	0.21	0.76
	3.41	6.08E+05		0.98	0.89
	4.21	7.51E+05		1.55	0.93
	5.01	8.93E+05		2.26	0.96
	5.95	1.06E+06		3.18	0.95
	6.55	1.17E+06		3.85	0.95

Table 12. Continued.

Test	V_C (fps)	Re	A_F (in^2)	F_D (lb)	C_D
7	1.73	3.08E+05	13.34	0.30	1.11
	3.41	6.08E+05		1.12	1.08
	4.21	7.51E+05		1.76	1.11
	5.01	8.93E+05		2.51	1.11
	5.95	1.06E+06		3.58	1.12
	6.55	1.17E+06		4.22	1.10
8	1.73	3.08E+05	14.00	0.28	1.01
	3.41	6.08E+05		1.11	1.01
	4.21	7.51E+05		1.82	1.09
	5.01	8.93E+05		2.66	1.13
	5.95	1.06E+06		3.67	1.10
	6.55	1.17E+06		4.40	1.09
9	1.73	3.08E+05	13.09	0.07	0.25
	3.41	6.08E+05		0.78	0.76
	4.21	7.51E+05		1.31	0.84
	5.01	8.93E+05		1.98	0.90
	5.95	1.06E+06		2.76	0.88
	6.55	1.17E+06		3.35	0.89
10	1.73	3.08E+05	13.73	0.11	0.41
	3.41	6.08E+05		0.71	0.66
	4.21	7.51E+05		1.15	0.70
	5.01	8.93E+05		1.75	0.76
	5.95	1.06E+06		2.48	0.76
	6.55	1.17E+06		2.97	0.75
11	1.73	3.08E+05	13.09	0.22	0.84
	3.41	6.08E+05		0.99	0.96
	4.21	7.51E+05		1.54	0.99
	5.01	8.93E+05		2.31	1.04
	5.95	1.06E+06		3.19	1.02
	6.55	1.17E+06		3.83	1.01
12	1.73	3.08E+05	13.73	0.18	0.65
	3.41	6.08E+05		0.86	0.80
	4.21	7.51E+05		1.39	0.85
	5.01	8.93E+05		2.06	0.89
	5.95	1.06E+06		2.86	0.87
	6.55	1.17E+06		3.32	0.84

The data provided insight on the relationships between drag coefficient and anchor geometry. The first investigated correlation was the mooring arm position and drag coefficient. Figure 47 shows the plot comparing drag coefficients as a function of Re for the fins fully extended and the mooring arm in-line and between fins. The drag

coefficient is higher by an average of 19.3% when the arm is in-line (I/L) when compared to between the fins (B/T). Except for the slowest towing velocity (V_C) of 1.73 fps, the drag coefficient for B/T is higher by 22% compared to I/L.

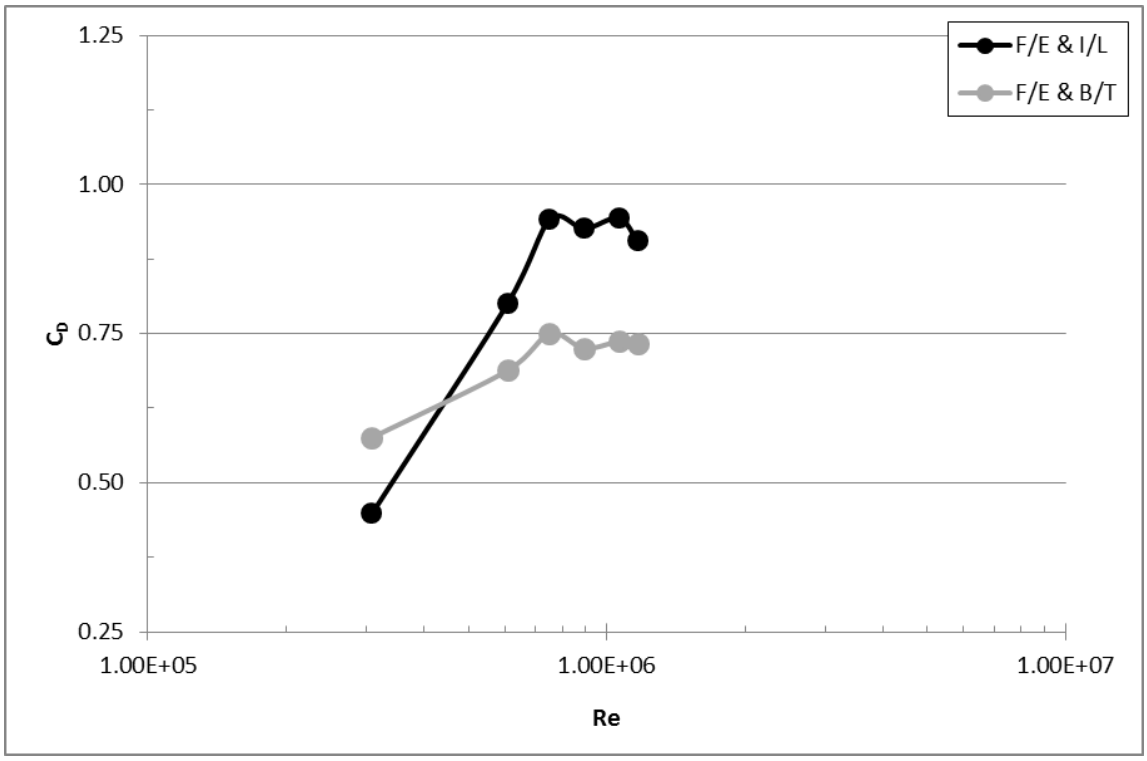

Figure 47. Drag Coefficient as a Function of Re – F/E with Mooring Arm I/L & B/T.

The next case comparison is when the fins are placed in the middle setting and the mooring arm is varied between I/L and B/T. The drag coefficient, again, is lower by 22% and 3% when the mooring arm is placed I/L from B/T at slower velocities, 1.73 and 3.41 fps, respectively. However, the drag coefficient is higher by an average of 5% when the arm is I/L compared to B/T when the velocity is increased from 4.21 fps through 6.55 fps. Figure 48 shows a plot of the results.

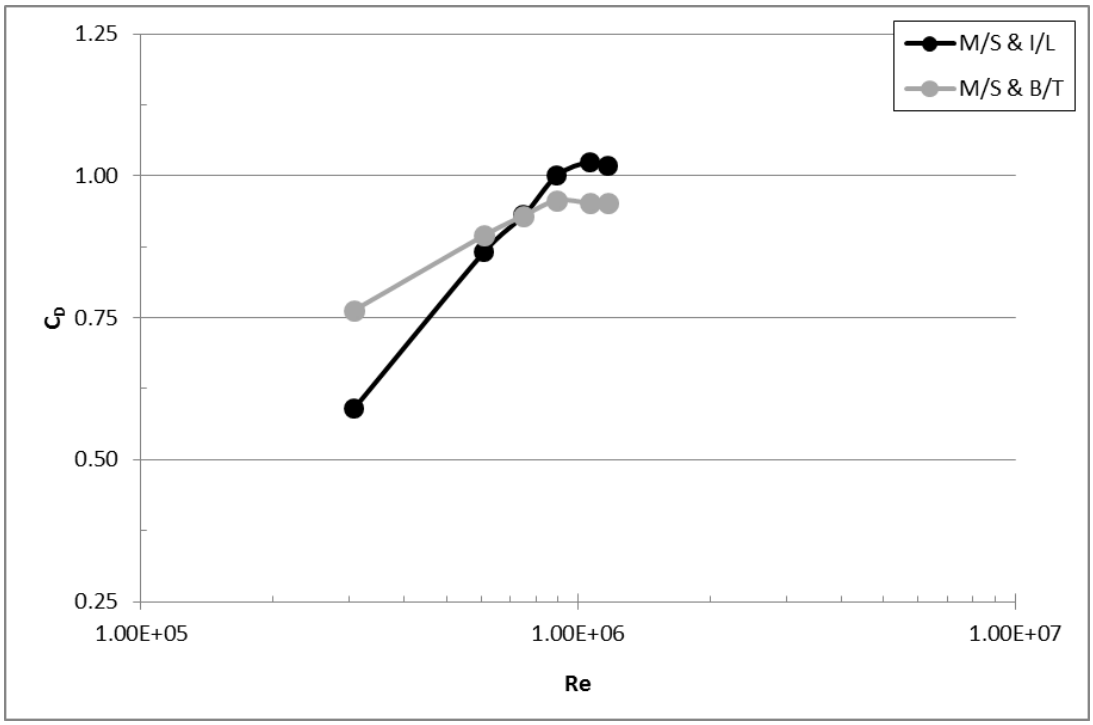

Figure 48. Drag Coefficient as a Function of Re – M/S with Mooring Arm I/L & B/T.

The final comparison between mooring arm position is when the fins are fully retracted, and shown in Figure 49. At the slowest tow velocity, the drag coefficient is 38% lower when the mooring arm is positioned to I/L from B/T. However, the drag coefficient is higher by an average of 15% when the arm is changed from B/T to I/L. It was surmised that the drag coefficient of the anchor increases, by a 13% average, when the arm is placed B/T compared to I/L. In addition, the result curves appear to level off towards a constant value of C_D for increasing Re number flows.

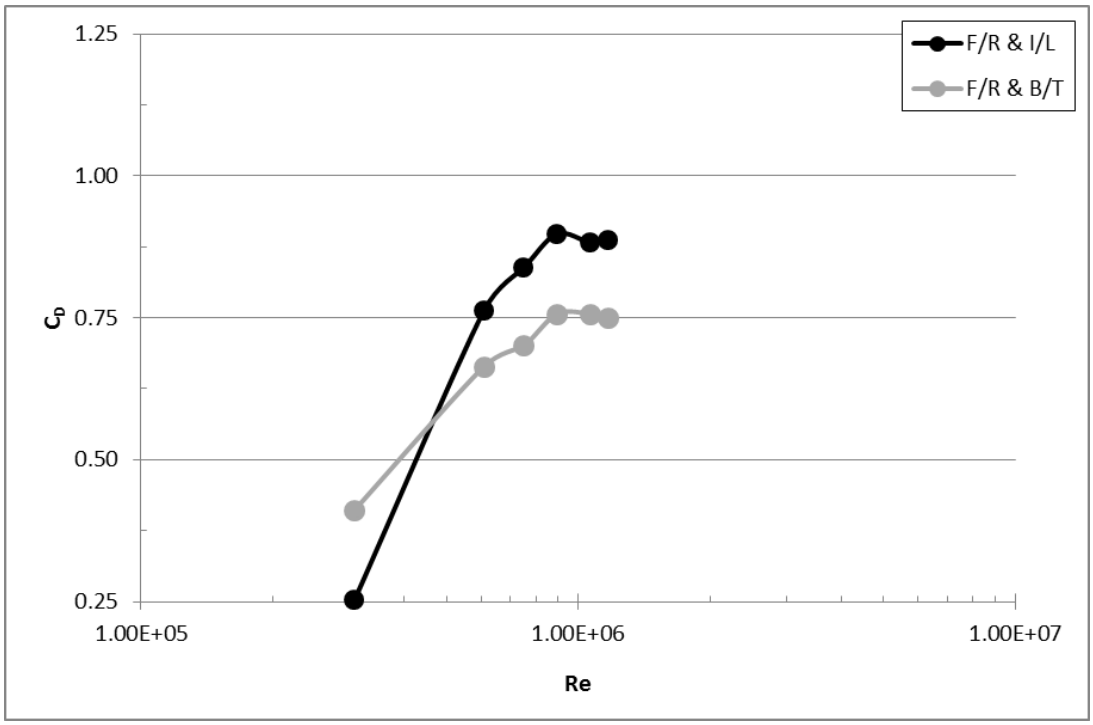

Figure 49. Drag Coefficient as a Function of Re – F/R with Mooring Arm I/L & B/T.

The next relationship investigated is the influence of fin position on the drag coefficient. Figure 50 shows the difference in drag coefficient when the mooring arm is I/L and the fin position is varied. For the tow velocity of 1.73 fps, the fins placed into the M/S had the highest drag coefficient of 0.59 while F/E and F/R were 24% and 57% lower, respectively. As Re number increased, the M/S had a consistently higher drag coefficient than compared to F/E and F/R, while F/R had steadily the lowest drag coefficient. When comparing average drag coefficients for the three highest tow velocities, the C_D for F/E was 4.3% higher than F/R and M/S C_D was 8% higher than F/E. These relatively low differences are expected because of the slight changes in anchor geometry.

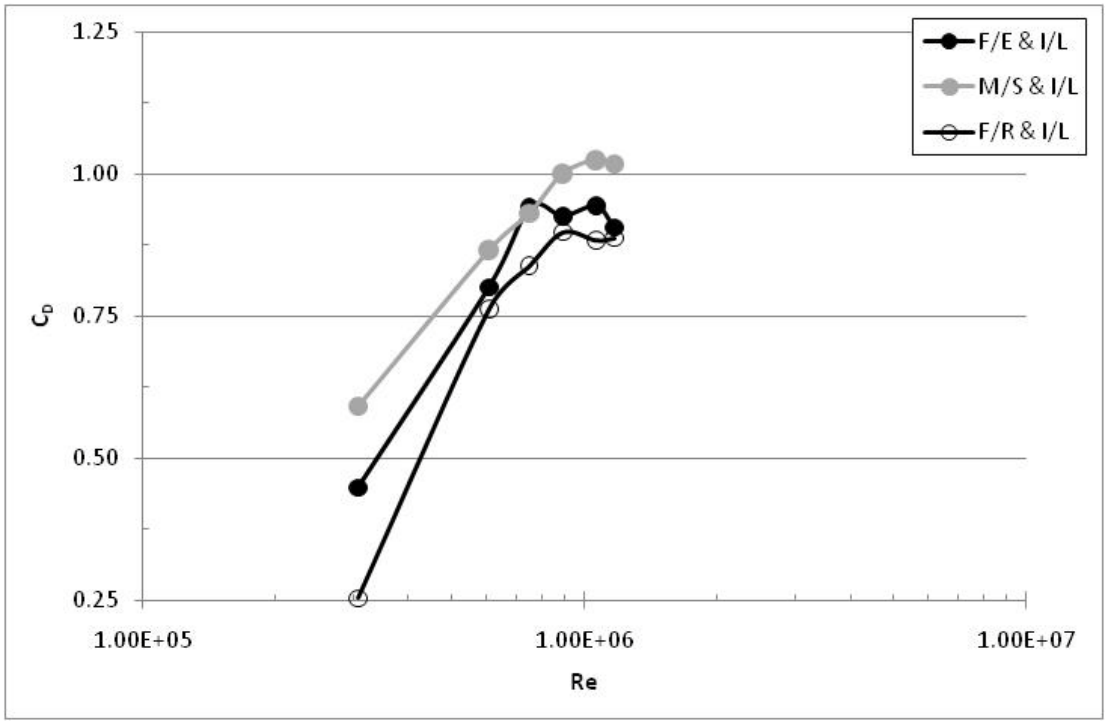

Figure 50. Drag Coefficient as a Function of Re – I/L with Fins F/E, M/S, & F/R.

Figure 51 depicts a plot comparing drag coefficients as a function of Re number when the mooring arm is B/T and the fins are changed between F/E, M/S, and F/R. As with the results for the mooring arm I/L, the fins placed in the M/S had consistently higher drag coefficients when the mooring arm was B/T. In addition, the F/E and F/R settings resulted in similar values of C_D as Re increased, with only an average 3% difference between the highest velocities. However when the fins were placed in the M/S, the drag coefficient for the upper velocities was 21% higher compared to F/E and F/R. When comparing the drag coefficients of the fins between I/L and B/T mooing arm positions for higher velocities, the F/E and B/T anchor setting had the lowest average

drag coefficient of 0.73 and M/S and I/L had the highest value of drag coefficient of 1.01, a difference of 28%.

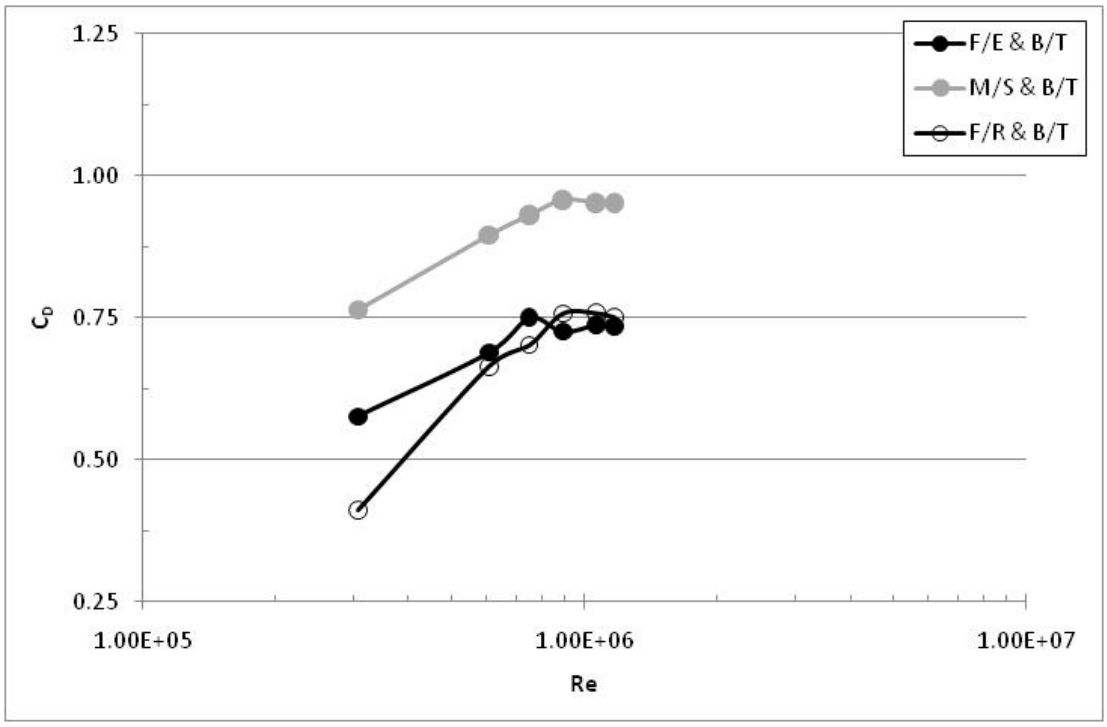

Figure 51. Drag Coefficient as a Function of Re – B/T with Fins F/E, M/S, & F/R.

The third relationship investigated was the effect of attaching the yellow mooring rope on the mooring arm of the anchor. The plastic nylon material naturally leaves bends in the line and at slow towing test velocities; the low drag forces acting on the rope are not strong enough to deform the rope into a straight line. Therefore, the natural bends in the rope form more frictional, frontal area, increasing the drag coefficient considerably at low velocities when compared to increases at high velocities. The bends are pictured, previously, in Figure 30.

Figure 52 shows a plot of drag coefficient as a function of Re when the anchor is set into F/E and I/L with the mooring rope attached. The rope increases the drag coefficient by 55% at 1.73 fps, which is attributed to the rope not deforming into a straight line behind the mooring arm. At higher velocities, the mooring rope increases the drag coefficient of the anchor by 12%. The curves also seem to follow the same pattern of increasing and then decreasing and then beginning to level.

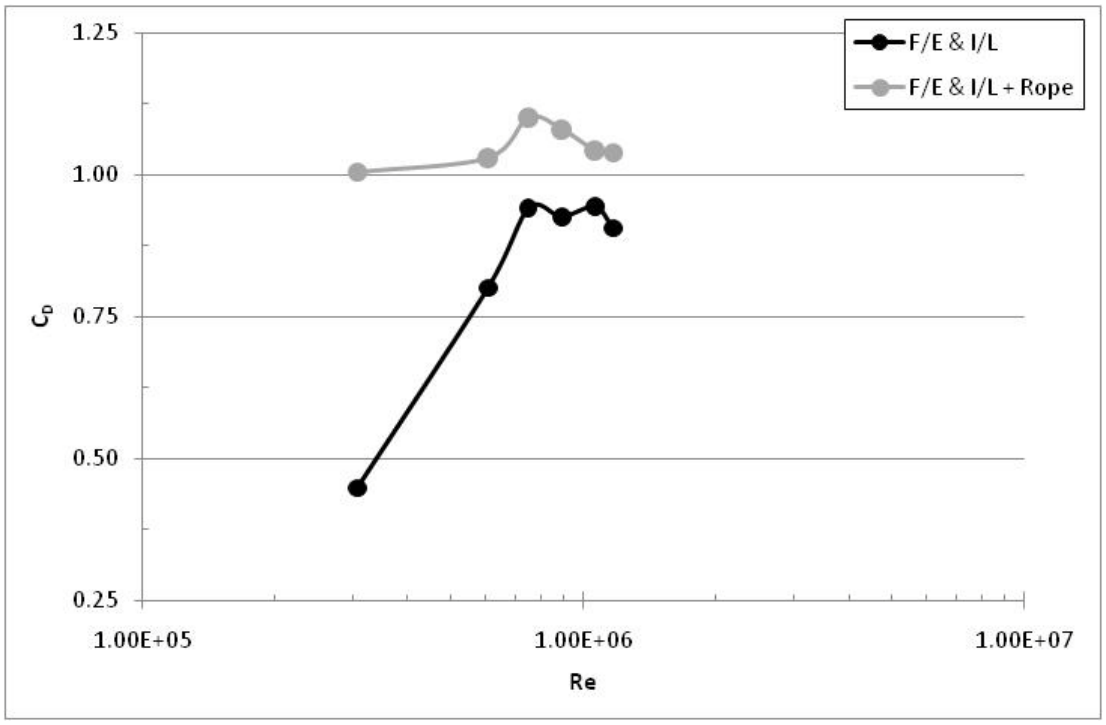

Figure 52. Drag Coefficient as a Function of Re – F/E & I/L with Mooring Rope.

Figure 53 depicts a plot of the drag coefficient as a function of Re number when the fins are placed into the M/S and the mooring arm is I/L with the mooring rope added. For the slowest velocity of 1.73 fps, the mooring rope increases the drag coefficient by

47%. However, when Re is increased, the mooring rope only increases the drag coefficient by an average of 12%. In addition, the curves for both drag coefficients appear to follow the same sequence of peaking and approaching near level as Re increases.

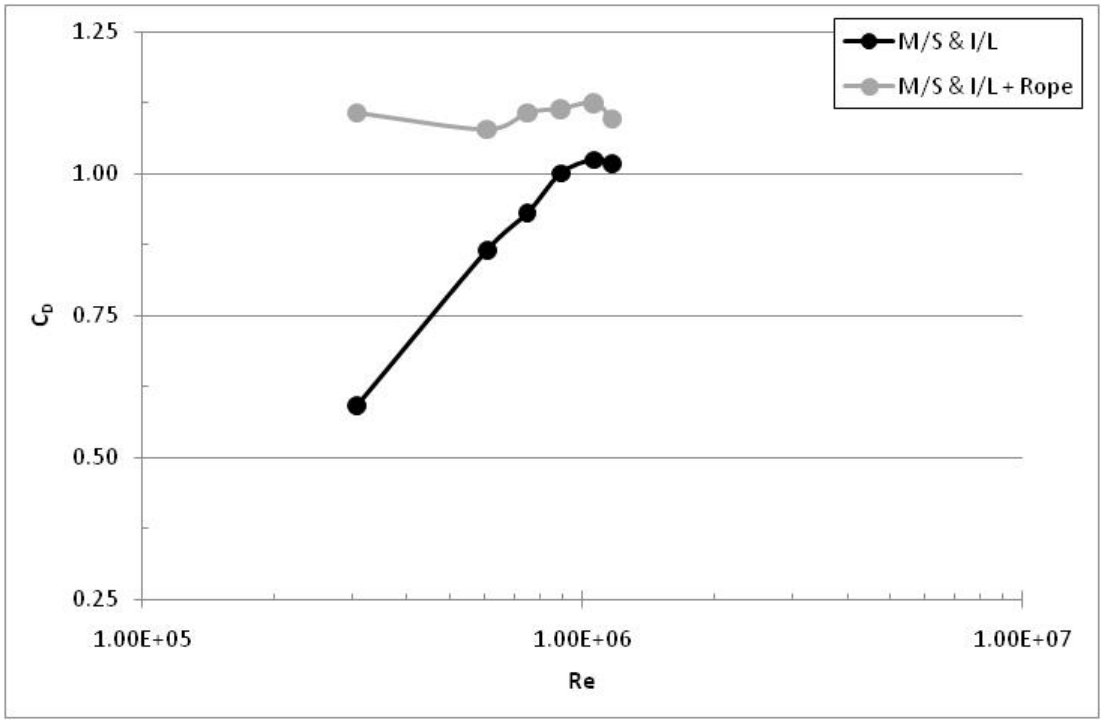

Figure 53. Drag Coefficient as a Function of Re – M/S & I/L with Mooring Rope.

Figure 54 presents a plot of drag coefficient as a function of Re number when the anchor is placed into the F/R and I/L setting with the addition of a mooring rope. The drag coefficient increase by 70% when the mooring rope is added for a tow velocity of 1.73 fps, which is the largest increase when the mooring rope is added. The mooring rope increases the drag coefficient an average of 15% for the remaining tow velocities,

and the drag coefficient pattern of each curve are very similar for tow velocities greater than 1.73 fps.

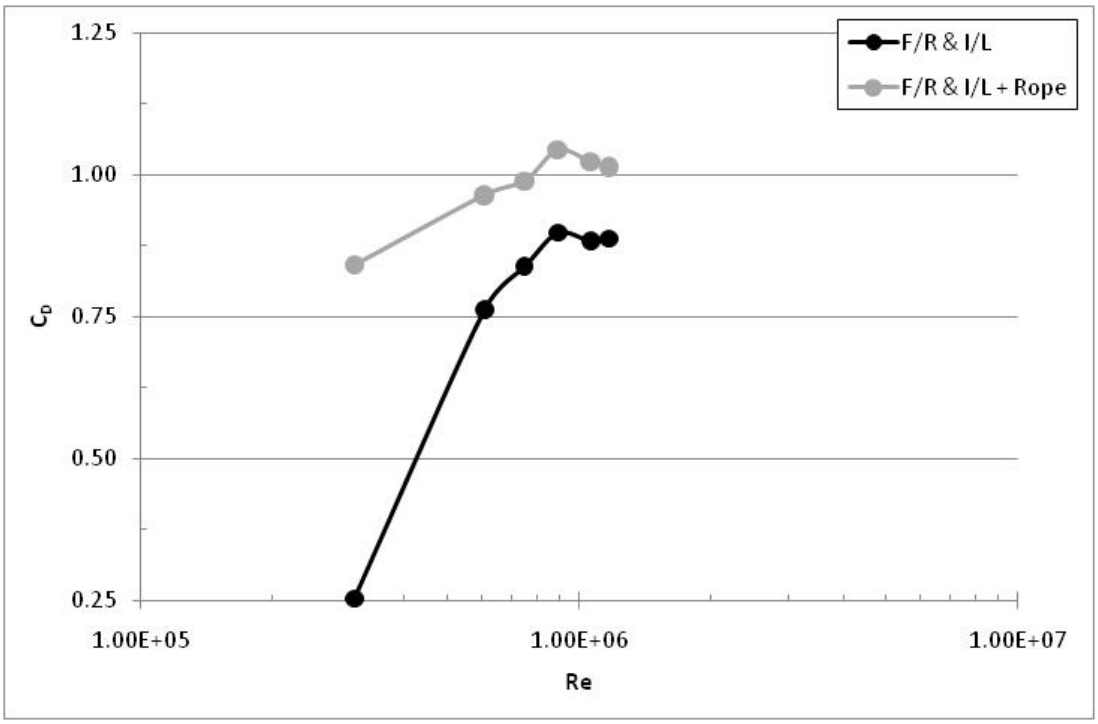

Figure 54. Drag Coefficient as a Function of Re – F/R & I/L with Mooring Rope.

Figure 55 is a plot of the total drag coefficient as a function of Re number when the anchor is set into F/E and B/T with the addition of the mooring rope. The drag coefficient does not increase as dramatically at the slowest tow velocity when compared to the mooring arm being I/L. However, the C_D difference between attaching the rope and not having the rope is still the largest at 1.73 fps compared to higher tow velocities. The drag coefficient value increases 26% and 14% for 1.73 fps and the average of the

remaining, higher velocities, respectively. As with the mooring arm I/L, the curves appear to follow the same trend when the mooring arm is B/T.

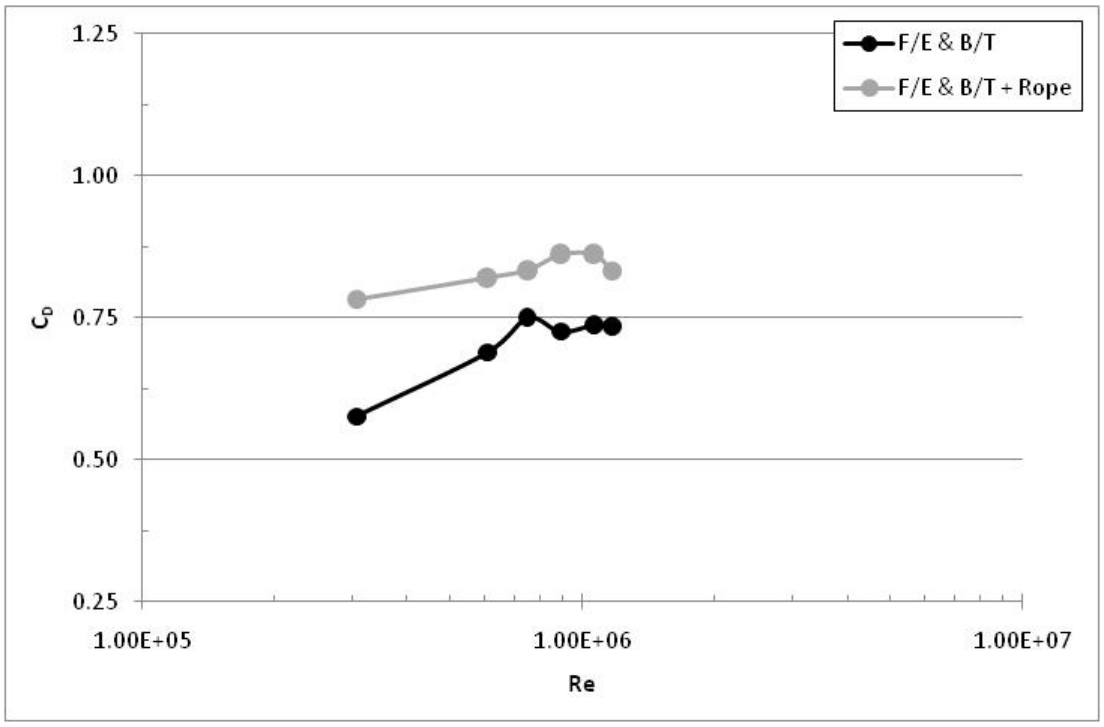

Figure 55. Drag Coefficient as a Function of Re – F/E & B/T with Mooring Rope.

Figure 56 shows a plot of drag coefficient as a function of Re number when the anchor is set to M/S and B/T with the inclusion of the mooring rope. A similar trend of incremental increases in drag coefficient results is noticed as Re number increases. For the higher tow velocities, 3.41 fps through 6.55 fps, the mooring rope increases the average drag coefficient by 13% compared to the anchor without the rope attached. At the lowest velocity, the addition of the mooring rope increases the drag coefficient by 25%.

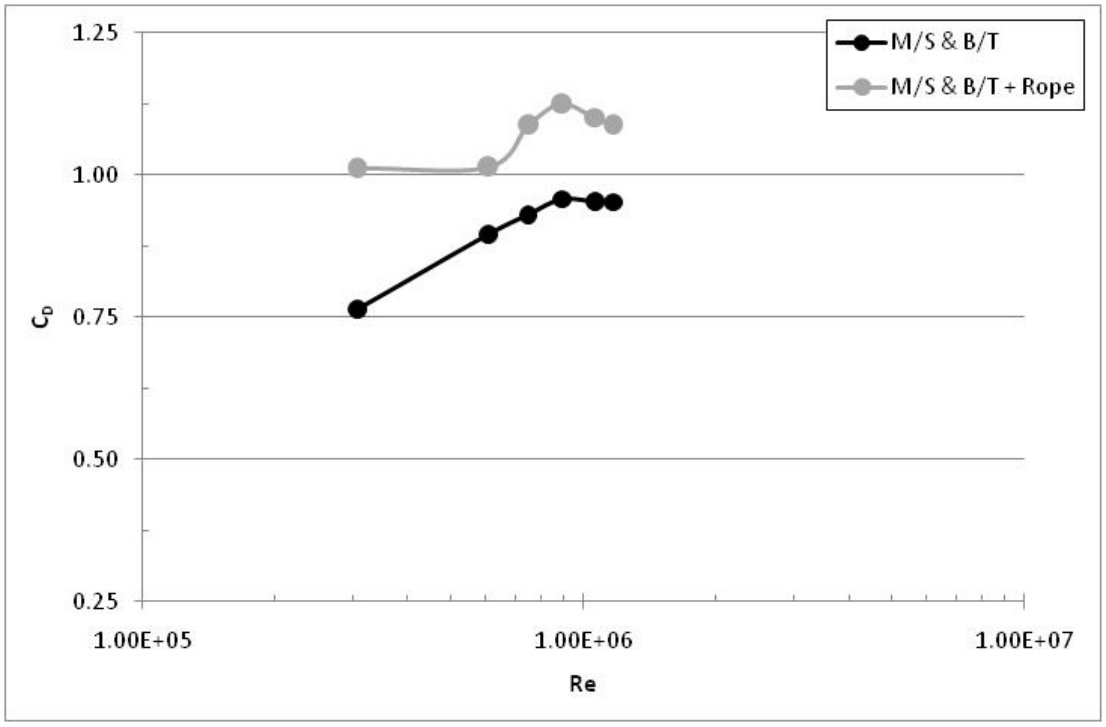

Figure 56. Drag Coefficient as a Function of Re – M/S & B/T with Mooring Rope.

Figure 57 shows the effect of the mooring rope on drag coefficient when it is attached to the mooring arm and the anchor is set into the F/R and B/T position and Re number is increased. The dramatic increase drag coefficient at the lowest tow velocity is not as apparent compared to the other cases. However, the difference is still the largest, a 36% increase when the rope is attached compared to when it is unattached. A change of 15% is the average amount of increase in drag coefficient for the higher velocities when the rope is attached. The results for drag coefficient, in this particular case, show a very similar pattern of gradually increasing, leveling off, and then slightly decreasing at the maximum tow velocity.

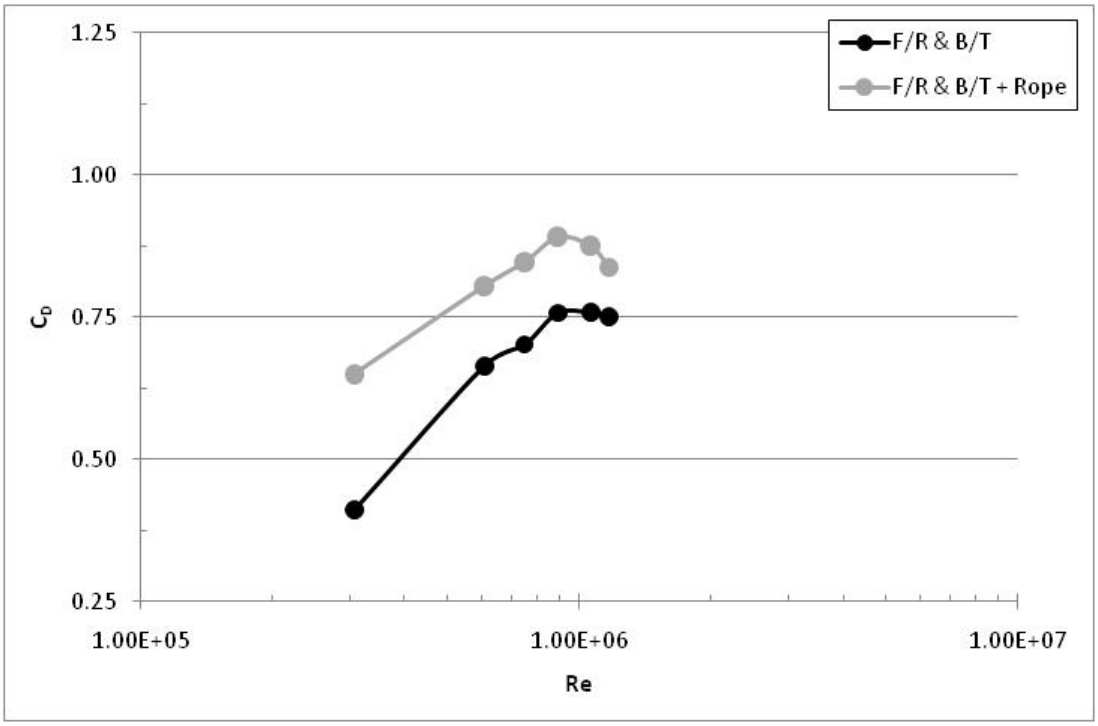

Figure 57. Drag Coefficient as a Function of Re – F/R & B/T with Mooring Rope.

Figure 58 plots a preliminary towing test result to validate the experimentation technique. The cylindrical, T-bar penetrator was attached to the front of the testing rig and towed at the same velocities as the anchor tests. An image of the T-bar is presented as Figure 5. The length scale required to calculate Re was the cylinder diameter of 3.5 in The resulting drag coefficient curve is very smooth which indicates good performance in terms of repeatability. Figure 59 compares the results obtained in the testing to results for cylinders and spheres published in Munson *et al.* (1990). The data points obtained in testing lie very near the drag coefficient curve for a sphere.

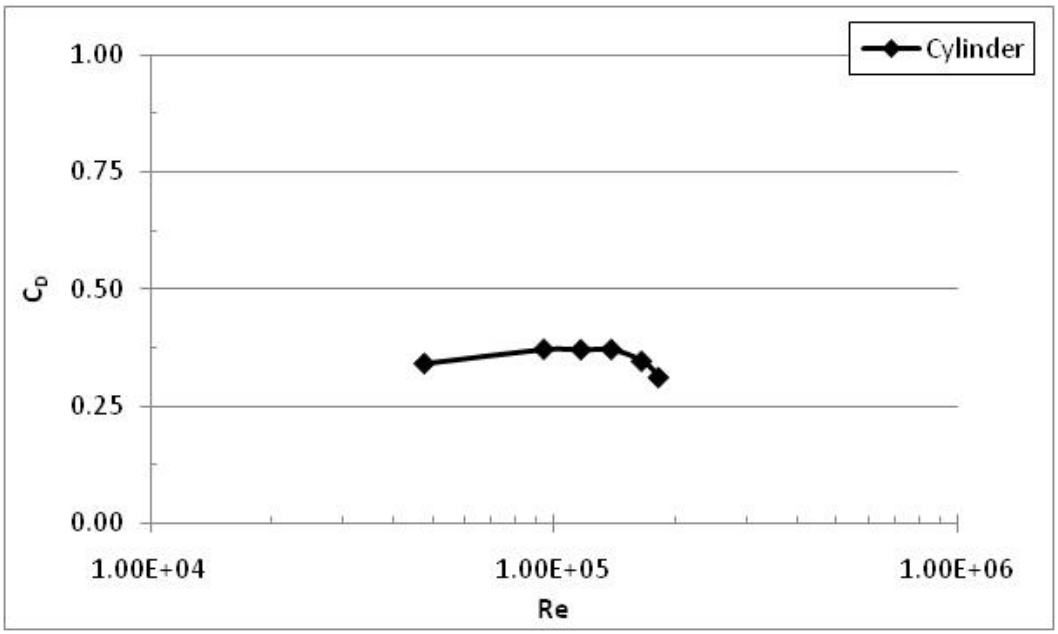

Figure 58. Drag Coefficient as a Function of Re - Cylinder.

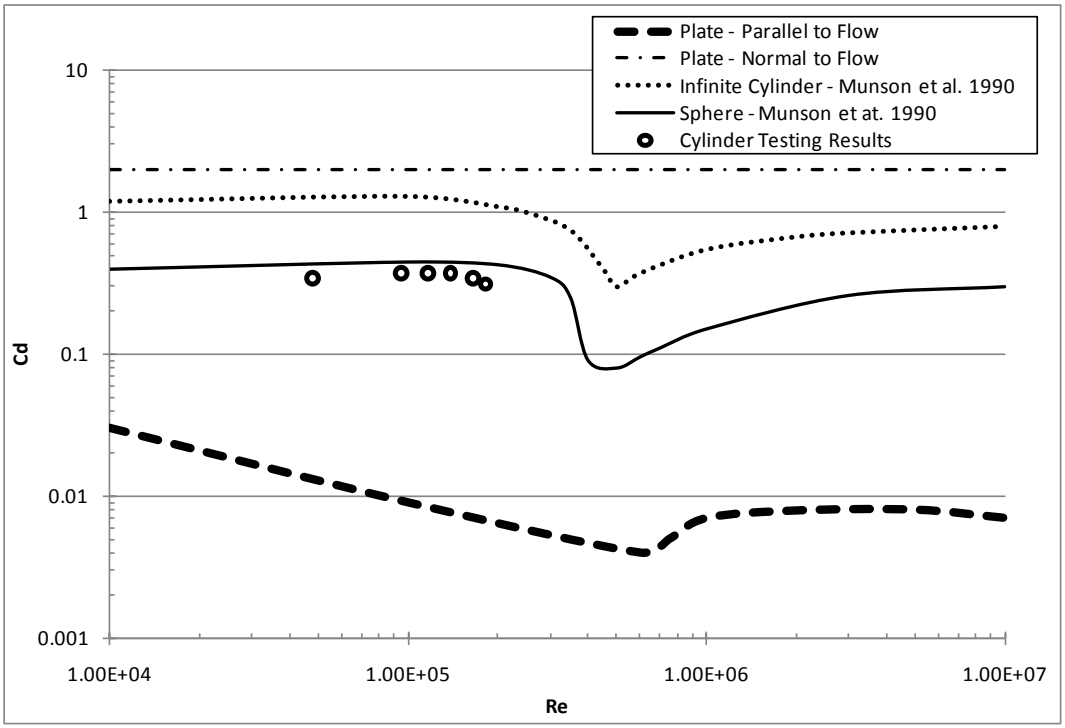

Figure 59. Drag Coefficient as a Function of Re – Cylinder Results Compared to Theoretical Curves.

Tow Testing Discussion and Experimental Error

Overall, the tow testing phase of testing the OMNI-Max resulted in quality data which gave more insight to the relationships between drag coefficient and anchor geometry. The differences between the mooring arm position, fin position, and the addition of the mooring rope with drag coefficient are evaluated. In addition, experimental error and possible improvements are discussed as well.

The observed trend when comparing the mooring arm position is that the higher drag coefficient switches from B/T to I/L as Re increased. This trend may be explained by the relationships between drag force due to friction, drag force due to pressure, and the when the boundary layer around the anchor becomes turbulent. The drag force on the anchor is dominated by skin friction drag at slow speeds. As the carriage velocity increases and pressure drag force becomes more of a factor, the drag force due to pressure drag increases faster when the mooring arm is I/L. This may be attributed to the turbulent vortices caused by the flow around the arm and interfering with the boundary layer on the upper fin behind the arm, triggering the boundary layer around the fin to become turbulent quicker, and causing more drag faster. This is justifiable because the tow testing occurred within the range of Re number where the boundary layer around cylinders, spheres, parallel plates, etc. transitions from laminar to turbulent. This transition is observed by the dip in drag coefficient when the drag coefficient is a function of Re number. The effects on drag due to a different separation point of the boundary layer behind the affected fin are negligible because of the slenderness of the fin itself.

The relationship between fin position and drag coefficient is interesting because when the fins were placed into the M/S, the C_D was consistently the highest. This may be explained by the fins contribution in the amount of pressure drag or friction drag for each fin setting. For fins in F/E position, the tips of the upper fins are parallel to the upstream flow, which contributes the least amount of pressure drag for each setting. However, F/E fins create the most surface area which increases the amount of friction drag. When the fins are retracted into the F/R position, the angle between the tips on the upper fins and the undisturbed streamlines is the largest. Therefore, this setting causes the most pressure drag because of the increased amount of wake. Conversely, the F/R setting retains the least amount of fin surface area, which results in the least amount of friction drag. Subsequently, when the fins of the anchor are placed into the middle setting, the friction drag and pressure drag are contributing to drag induced by the fins on the anchor. Therefore, this setting repeatedly produced a higher drag coefficient. A relation between friction drag and pressure drag as contributed by fin position is presented as Figure 60.

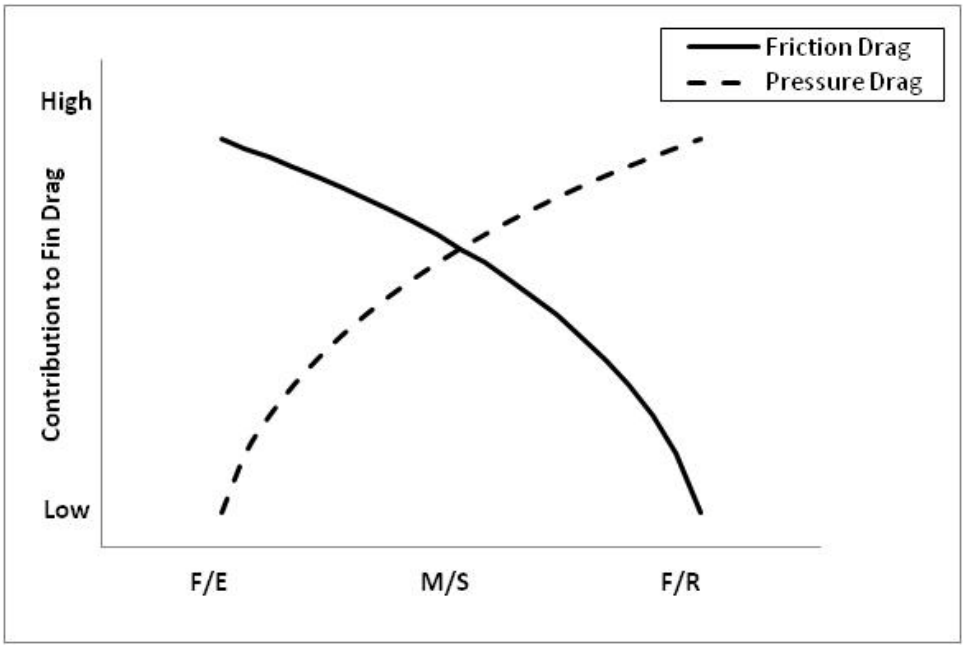

Figure 60. Drag Contribution According to Fin Setting.

When the mooring rope was attached to the mooring arm, the drag coefficient increased for every case. However, C_D increased the most when the anchor and rope were being towed at the slowest velocity of 1.73 fps. This is due to the natural bends in the yellow rope creating more projected area which generates an relatively high pressure drag contribution at slow speeds. When the rope began to straighten-out as the tow velocity was increased, the drag coefficient increased an average of 13.5% for all anchor settings. Therefore, the type of drag force induced on the anchor by the mooring rope at the higher velocities was predominately skin friction drag, because the projected frontal area of the rope is much smaller than the surface area when deformed into a straight line. A close resemblance in drag coefficient curves arose for each test case, when comparing

curves with or without the rope, which indicates a somewhat linear increase in drag coefficient.

The test results obtained with the head of the T-bar substantiates that the testing rig performed well. The 12.125 in long and 3.5 in diameter cylinder produced drag coefficients very similar to that of a sphere, and not a cylinder, at the same Re number. However, the drag coefficients used to formulate the cylinder curve in Figure 59 were calculated on the basis that the cylinder is infinitely long. Conversely, the T-bar head, being finite, allows fluid to pass around the ends of the cylinder, reducing the wake effects, which reduces the drag force and subsequently the drag coefficient (Munson *et al.* 1990). In addition, the T-bar head length to diameter ratio is approximately 4, which is somewhat close to the shape of a sphere in terms of boundary layers and hydrodynamic wake. Therefore, the drag coefficient curve of the T-bar head being close to that of a sphere is reasonable.

The error associated with this phase of experimental anchor testing was introduced at various points. Misaligning the anchor, repositioning the anchor, and vibrations caused by the moving tow/dredge carriage introduced possible measurement errors which affected the results.

The first problem that arose is the anchor was not properly aligned on the testing rig. If the centerline of the anchor is not parallel to the centerline of the tow tank during testing, the total drag force would be divided into different transducer channels. For example, if the anchor were slightly angled in the +X direction, the drag force would be divided into +Mz and +Mx. In addition, the slight angle would dramatically increase the

amount of drag force because of a relatively large increase in projected frontal area, resulting in erroneous drag force measurement.

Therefore, all six channels of the force transducer were monitored and recorded for data quality assurance. When the data was analyzed, the channel measuring the moment about the Y axis was determined to be malfunctioning. Therefore, the results are not included in following figures. Figure 61, Figure 62, Figure 63, Figure 64, and Figure 65 show the measured force or moment recorded by the force transducer, during the constant speed period, as a function of carriage velocity. The forces in the X and Z directions are near a tenth an order of magnitude compared to the forces in the Y direction. In addition, the moments about the X axis are a factor of 10 higher than the moments about the Z axis, which validates that the testing rig was oriented well.

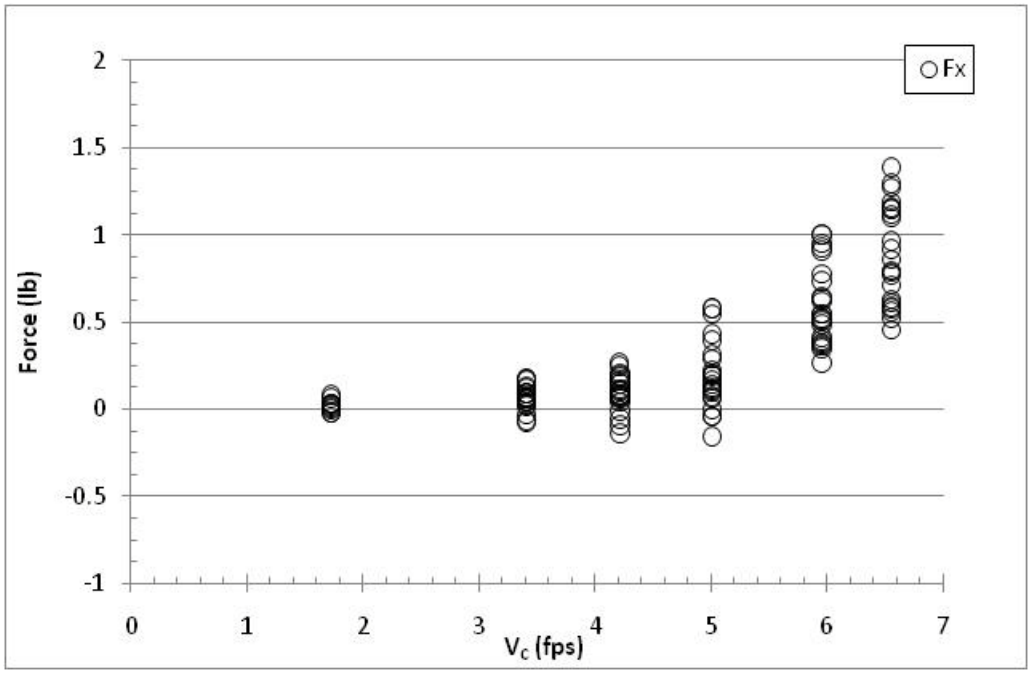

Figure 61. Tow Testing Data - Force Through Fx Channel Caused by Anchor.

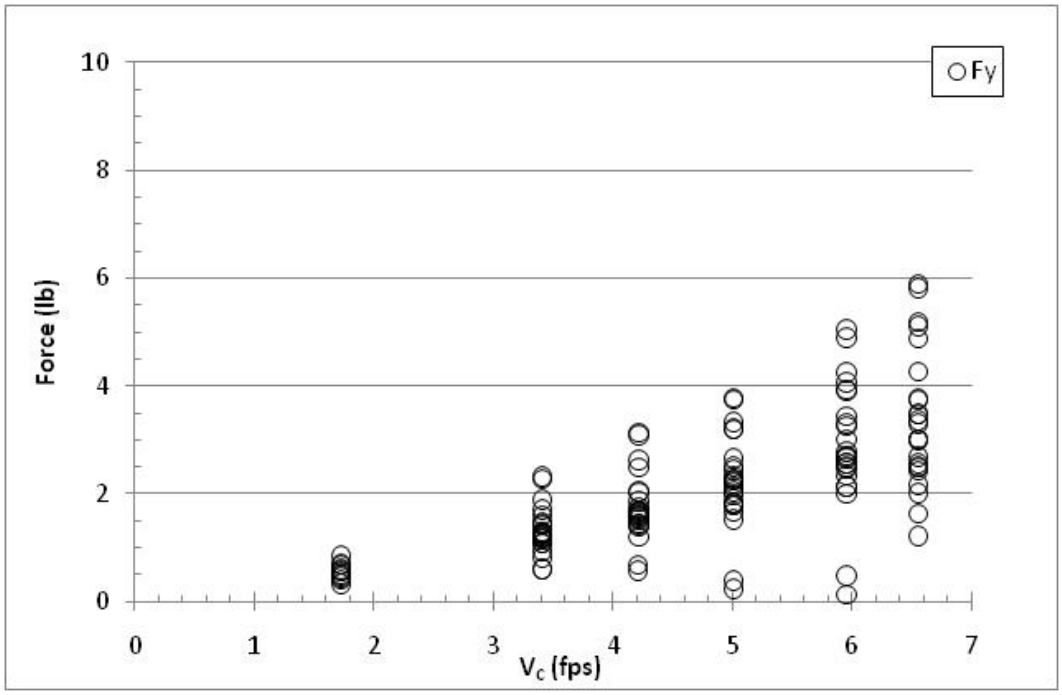

Figure 62. Tow Testing Data - Force Through Fy Channel Caused by Anchor.

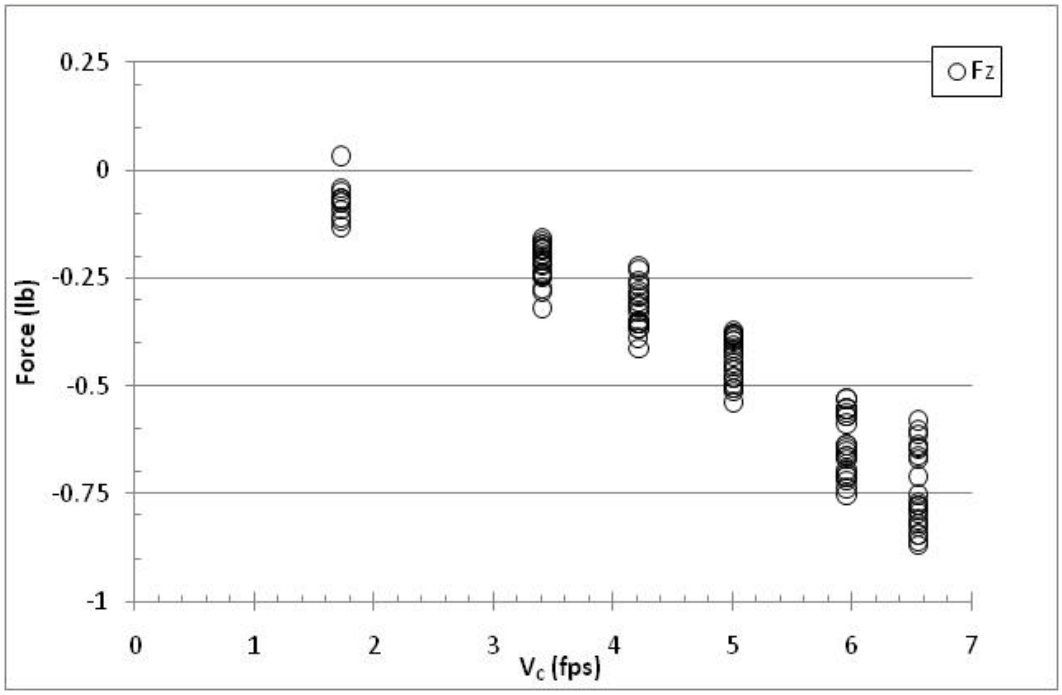

Figure 63. Tow Testing Data - Force Through Fz Channel Caused by Anchor.

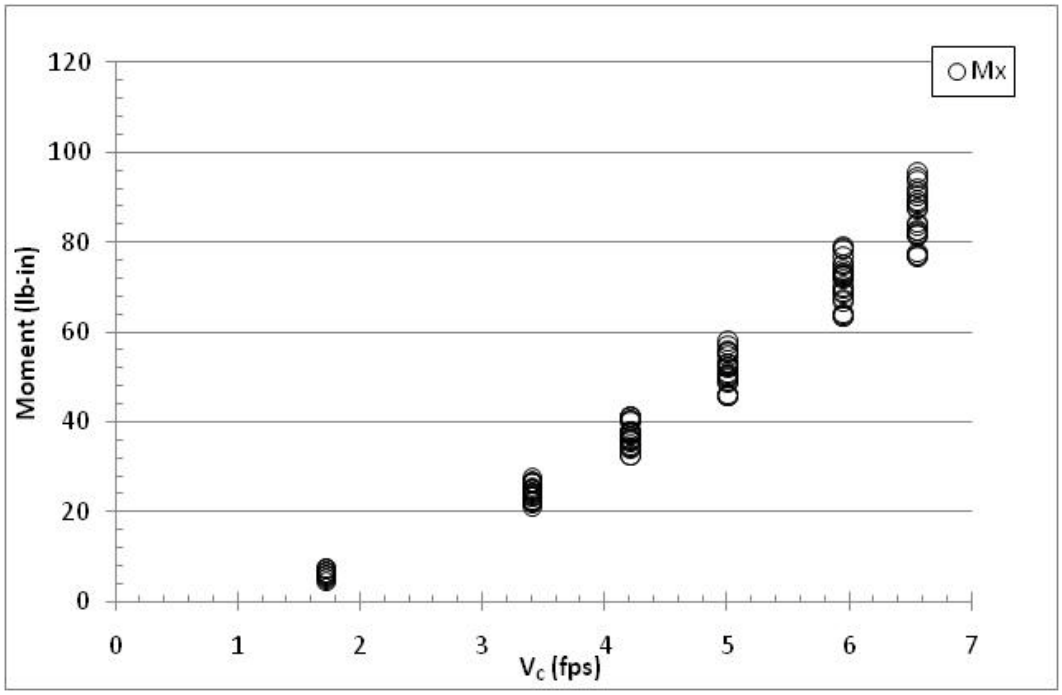

Figure 64. Tow Testing Data – Moment Through Mx Channel Caused by Anchor.

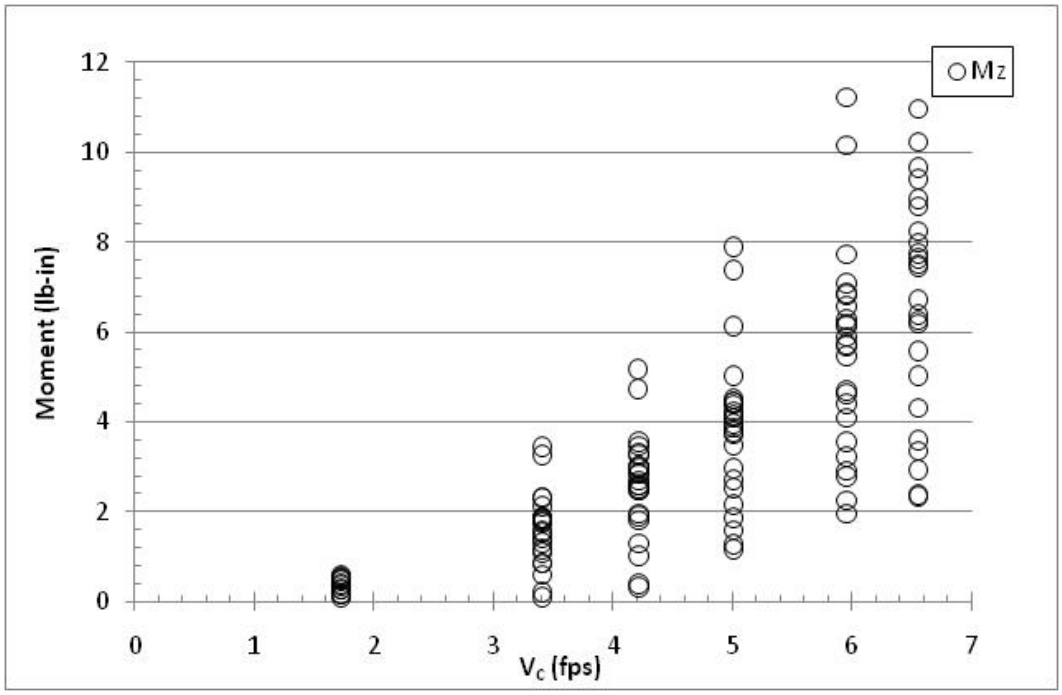

Figure 65. Tow Testing Data – Moment Through Mz Channel Caused by Anchor.

Another source of error occurred when repositioning the anchor on the testing rig. If too much force were applied during repositioning, then the calibration curve to calculate forces or moments from voltage changed slightly. During repositioning, great care was taken to ensure that the dynamometer was not subjected to very much force. Also, calibration curves were taken before and after testing and averaged to produce the curve used in data analysis.

Error was introduced during testing when the carriage was travelling along the rails. The rails caused vibrations which affected the lower section of the testing rig. The vibrations caused spikes in moment measurements which skewed the average during the constant speed period of the test run. This was addressed by isolating the testing rig with hard rubber dampeners and performing the test runs on the smoothest portions of the rail system.

There are a few recommendations concerning this phase of testing. A range of cylinders with different length to diameter ratios could be tested and evaluated to further validate the testing procedure. The ranges of test velocities could be increased between 1.73 and 6.55 fps to increase the resolution of results. In addition, more test runs per case would result in a smoother average moment value per anchor setting and tow velocity.

Free Fall Testing

Free Fall Testing Results

The 1/15 scale model OMNI-Max anchor was subjected to free fall testing to evaluate the terminal velocity and drag coefficient as a function of anchor shape and

anchor attachments. The evaluated anchor settings were placing the upper and lower fins into the fully extended, middle setting and fully retracted positions, while the mooring arm was varied between in-line with the fins and between the fins. In addition, the white model mooring line was attached to the model anchor to evaluate its effects. Table 13 summarizes a description of each test case that was evaluated.

Table 13. Free Fall Testing - Test Descriptions.

Test	Lower Fins			Upper Fins			Mooring Arm Position		Attachments
	Fully Extended	Middle Setting	Fully Retracted	Fully Extended	Middle Setting	Fully Retracted	In-Line with Fins	Between Fins	
1/1a	X			X			X		-
2/2a	X			X				X	-
13/13a		X			X		X		-
14/14a		X			X			X	-
15/15a			X			X	X		-
16/16a			X			X		X	-
17/17a	X			X				X	Mooring Rope
18/18a		X			X			X	Mooring Rope
19/19a			X			X		X	Mooring Rope

The tests were recorded using two video cameras positioned at different depths in the dredge/tow tank sediment basin. The movements of the free falling anchor were captured and analyzed. Through using the anchor's overall length and the striped board as references, a relation that calculated the depth from each camera's pixel map was formulated. A unique pixel to depth conversion ratio was calculated for each camera,

shallow and deep, for each test. Therefore, the velocity was calculated knowing the time step and change in depth of the anchor. Equation (27) is the relation used to calculate depth from a pixel map.

$$Depth = \frac{(P_{N,T} - P_R)}{R_{P-I}} + D_R \tag{27}$$

where $P_{N,T}$ is the pixel number associated with either the nose or the tail, P_R is the pixel number of the reference point, R_{P-I} is the ratio of pixels per inch, and D_R is a depth reference in inches. Essentially, P_R was the pixel denoting the top edge of the frame of the camera, which was either the top of the board for the shallow camera or the highest stripe shown by the shallow camera. Figure 66 shows the values used for R_{P-I}.

The anchor velocity as a function of depth was plotted as shown in Figure 67. The tail depth was transposed into a nose depth to form a clearer result curve. This was accomplished by adding the length of the anchor to D_R.

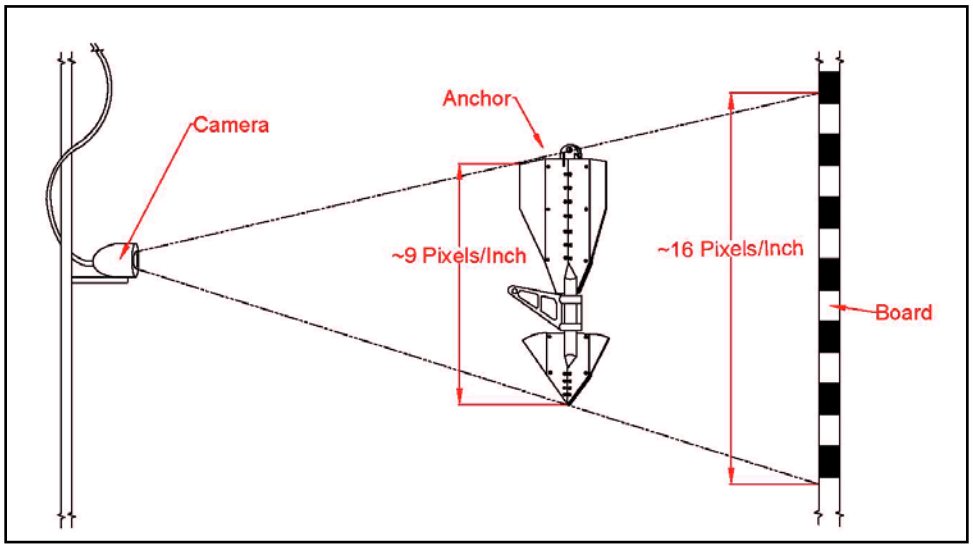

Figure 66. Schematic of Pixel Ratio for Free Fall Testing.

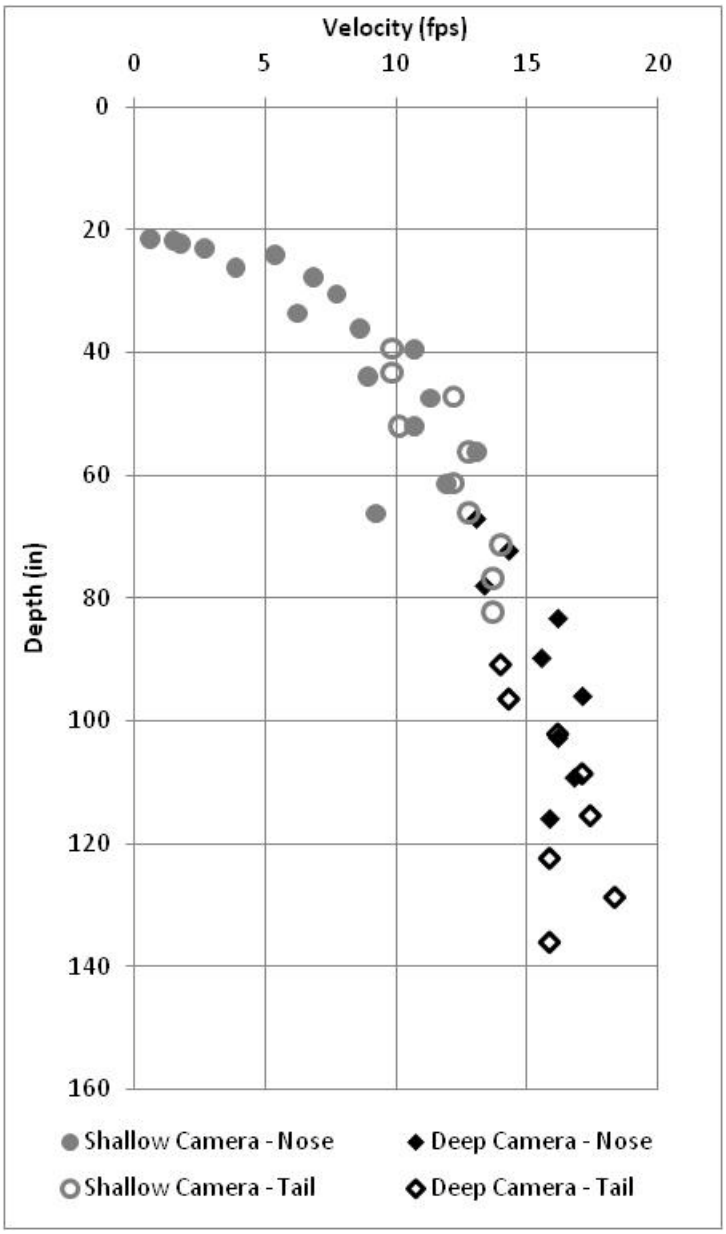

Figure 67. Typical Plot of Results for Velocity as a Function of Depth.

Plots were generated for each anchor free fall test and analyzed. According to the resulting curves, the anchor appeared to reach terminal velocity for every test condition. This was deduced by observing that the anchor velocity beneath a depth of around 100 in did not substantially increase. Therefore, averages of the velocities beneath a depth of 100 in were taken as the terminal velocity of the anchor. Once the terminal velocity was defined, the properties of the model anchor were used to calculate the drag forces on the anchor and the drag coefficients were calculated. Table 14 summarizes the dry and wet weight of the model anchor used to calculate the drag force when the anchor and/or mooring rope have reached terminal velocity. Table 15 depicts the results of the free fall testing by presenting the terminal velocity and drag coefficient for each case.

Table 14. Free Fall Testing Drag Force Assumptions.

Item	Dry Weight (lbs)	Wet Weight (lbf)	Difference (Buoyant Force) (lbf)	Drag Force (lbf)
1/15 Scale Model Anchor	20.92	17.67	3.25	14.42

Table 15. Free Fall Testing - Test Results.

Test	V_T (ft/s)	Re	A_F (in^2)	F_D (lbs)	C_D
1/1a	18.51	3.30E+06	13.55	14.42	0.461
2/2a	16.32	2.91E+06	14.21	14.42	0.565
13/13a	15.01	2.68E+06	13.34	14.42	0.712
14/14a	13.55	2.41E+06	14.00	14.42	0.833
15/15a	14.37	2.56E+06	13.09	14.42	0.792
16/16a	13.97	2.49E+06	13.73	14.42	0.798
17/17a	12.99	2.32E+06	14.21	13.83	0.857
18/18a	13.28	2.37E+06	14.00	13.83	0.831
19/19a	13.07	2.33E+06	13.73	13.83	0.876

The effect of the mooring arm alignment on the terminal velocity and drag coefficient was investigated. The arm was varied between I/L and B/T, like with the other test phases. However, the arm was consistently oriented in the towards the tow carriage, in the Westerly direction. Essentially, the anchor was rotated the same as during the tow testing phase. During tow testing, the mooring arm always hung toward the bottom of the tank while the anchor and stinger were rotated on the testing rig. The definition of I/L and B/T will still signify the same mooring arm setting.

Figure 68 plots the calculated drag coefficient as influenced by mooring arm position with different fin settings as function of Re number. The results show that placing the mooring arm B/T causes an increase in drag coefficient of varying amounts with respect to fin position. When the fins were placed into the F/E, M/S, and F/R positions, the C_D increased by 18%, 15% and 0.8%, respectively, when the mooring arm was placed into B/T from I/L. When the mooring arm was held B/T and the fin positions were varied from F/E to F/R and then from F/R to M/S, the drag coefficient increased by 29% and 4%, respectively. Also, when the mooring arm was held I/L and fin positions varied from F/E to M/S and then from M/S to F/R, the drag coefficient increased by 35% and 10%, respectively.

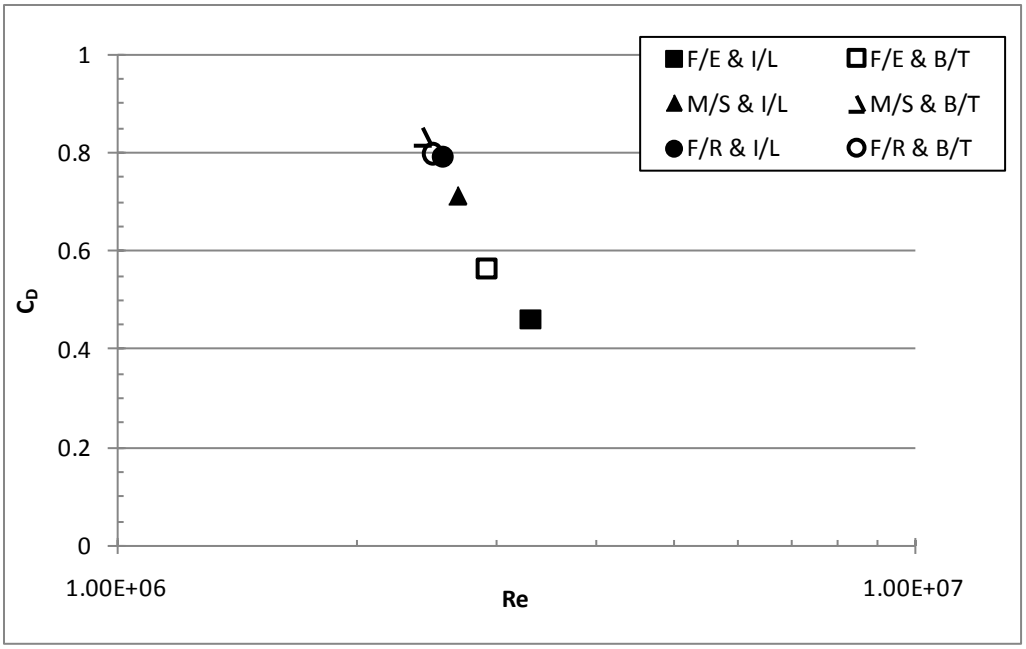

Figure 68. Drag Coefficient as a Function of Re – Fin Position and Mooring Arm Free Fall Testing Results.

One end of the white mooring rope was attached to the model anchor on the mooring arm and the other end was attached to a weight placed on the towing tank floor around 10 ft to 12 ft eastwardly, away from the cantilevered platform. When the anchor was lowered into the water, the attached model mooring rope took the shape of a reversed catenary curve before each test, which was due to the rope being positively buoyant. When the anchor was released, the rope tracked from a reverse catenary curve to a parabolic curve after the anchor impacted the sand bags. The drag coefficient of the anchor as affected by the mooring rope and is plotted in Figure 69 as a function of Re number.

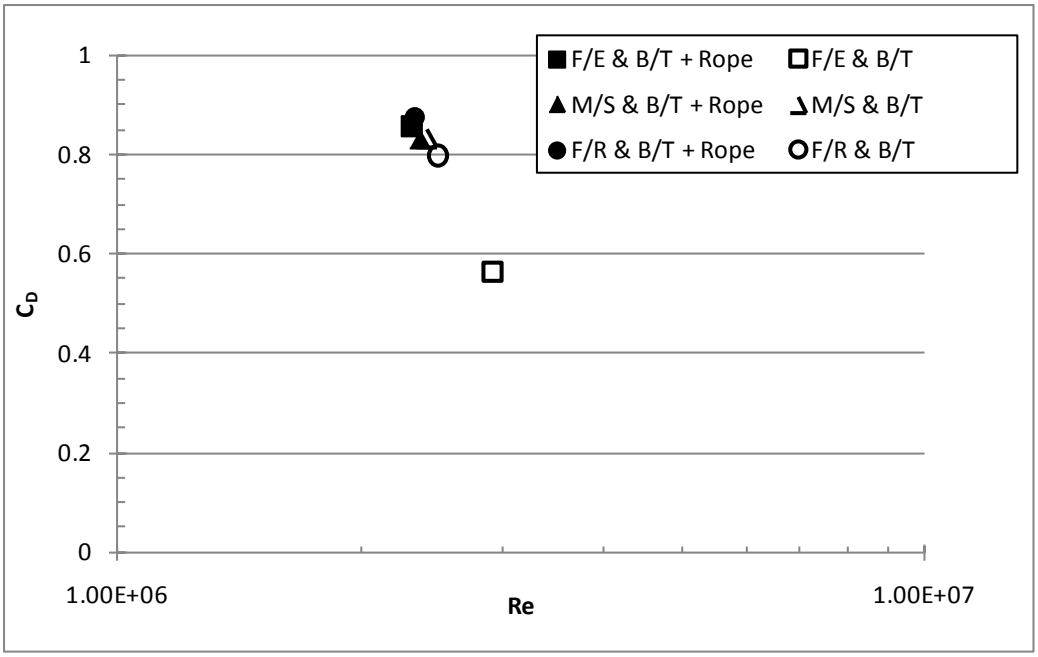

Figure 69. Drag Coefficient as a Function of Re - Mooring Rope Free Fall Testing Results.

Figure 70 indicates a slight difference in C_D when the rope is attached for the M/S and F/R fin position. The rope increases the drag coefficient by 9% when the fins are F/R. A decrease in drag coefficient of 0.8% was calculated when the rope was attached to the anchor with fins placed into M/S, which is a negligible difference. The drag coefficient for the anchor with F/E fins and the mooring rope is similar to other anchor fin settings with the mooring rope.

However, the drag coefficient for the anchor with the fins F/E without the mooring rope is considerably lower. This is attributed to the differences in human judgment, because separate people processed the images of the falling anchor at different periods during testing. This discrepancy only affected two test cases, when the anchor fins were placed into F/E, without the mooring rope, while the mooring arm was varied

between I/L or B/T. Therefore, comparing the effect of mooring arm position or fin position between the two is suitable because the same person processed the images for both cases. However, when making comparisons to images processed by another person, differences in choosing reference points on the anchor to record pixel coordinates, causing error, become pronounced. If different reference "points" on the anchor images are chosen, then the assumption that the pixel difference between the nose and tail points are separated by the entire anchor length is invalid. The differences in terminal velocity for the F/E test case are shown in Figure 70.

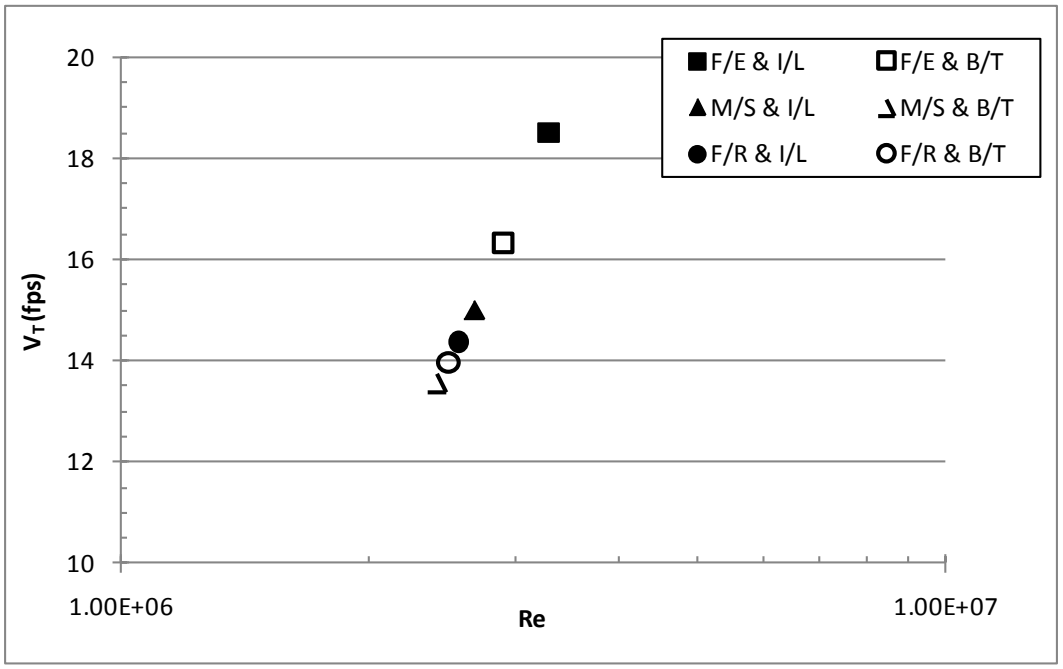

Figure 70. Terminal Velocity and Re - Free Fall Testing.

The previous figures and results in this section only depict the anchor during terminal velocity. The following figures show the typical behavior of the drag coefficient

during the acceleration period of free fall. Figure 71 shows the data points for anchor velocity increasing as a function of depth, with a natural log curve fit line.

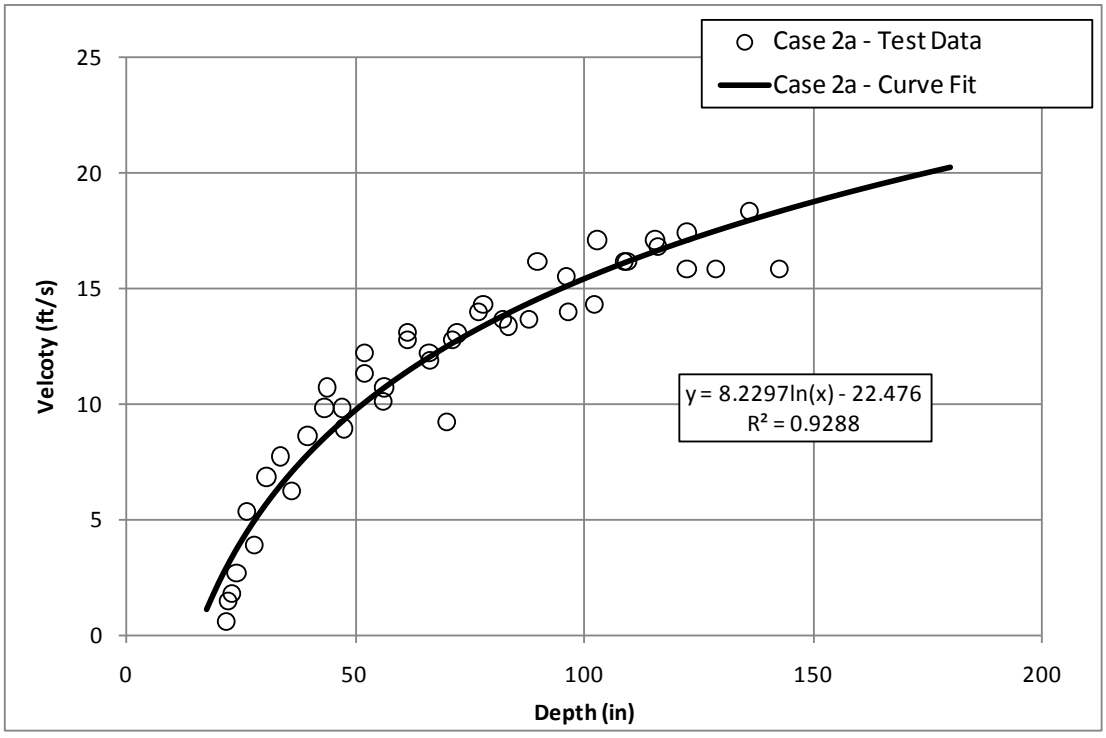

Figure 71. Example Plot of Velocity as a Function of Depth - Data Curve Fit.

There was an assumption made about the virtual mass, specifically the added mass (i.e. the water "carried" by the accelerating anchor) during free fall. This added mass was assumed to be 25% of the anchor mass for case 2a. Equation (22) was used to calculate the drag coefficient as a function of velocity. Figure 72 plots drag coefficient as a function of depth, with the vertical axis being placed into a base 10 log scale. The plot indicates that the drag coefficient decreases inversely logarithmically. This is due to the velocity as a function of depth data being curve fitted to a natural log expression. In

addition, the drag coefficient of 0.565 calculated through taking the average of the velocity deeper than 100 in is also plotted and shows a good relationship with the curve.

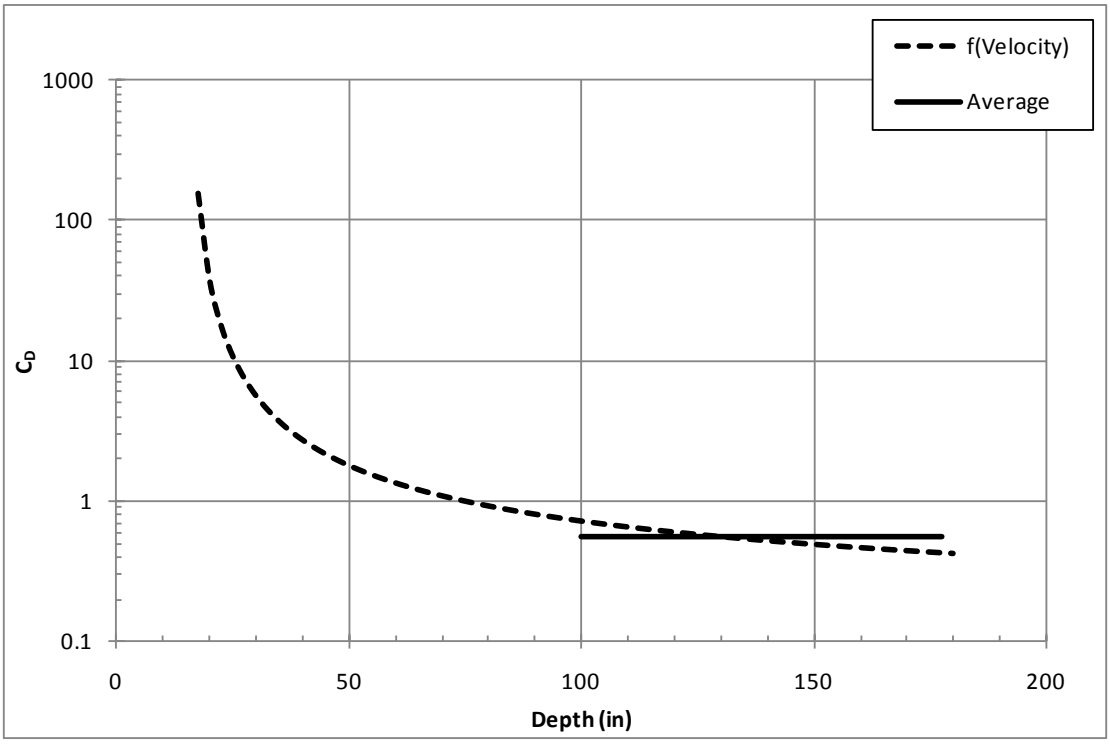

Figure 72. Free Fall Testing - Drag Coefficient as a Function of Water Depth.

Figure 73 shows how drag coefficient behaves as a function of anchor velocity, with the vertical axis being placed into base 10 log scale. The curve indicates that the drag coefficient decreases as velocity increases. This plot also shows that the drag coefficient is very sensitive to velocity, because the drag force is, primarily, a function of velocity. The drag coefficient calculated by taking the average of velocity data points beneath 100 in was plotted along with the curve and shows the averaging technique was justifiable.

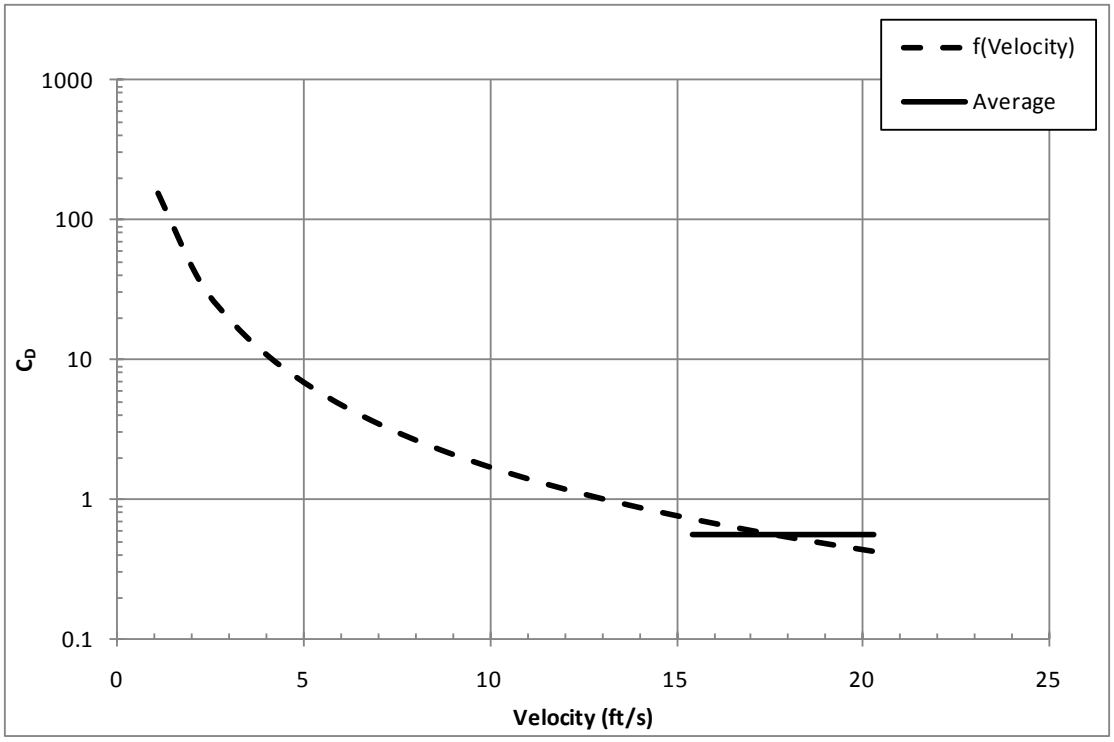

Figure 73. Free Fall Testing - Drag Coefficient as a Function of Velocity.

Figure 74 depicts the drag coefficient as a function of Re number, with both the vertical and horizontal axes being placed into base 10 log scales. The curve indicates that the drag coefficient decreases as Re number increases. Since both drag coefficient and Re number are functions of velocity, a straight line is logical. Also plotted was the drag coefficient calculated with the averaged velocity data.

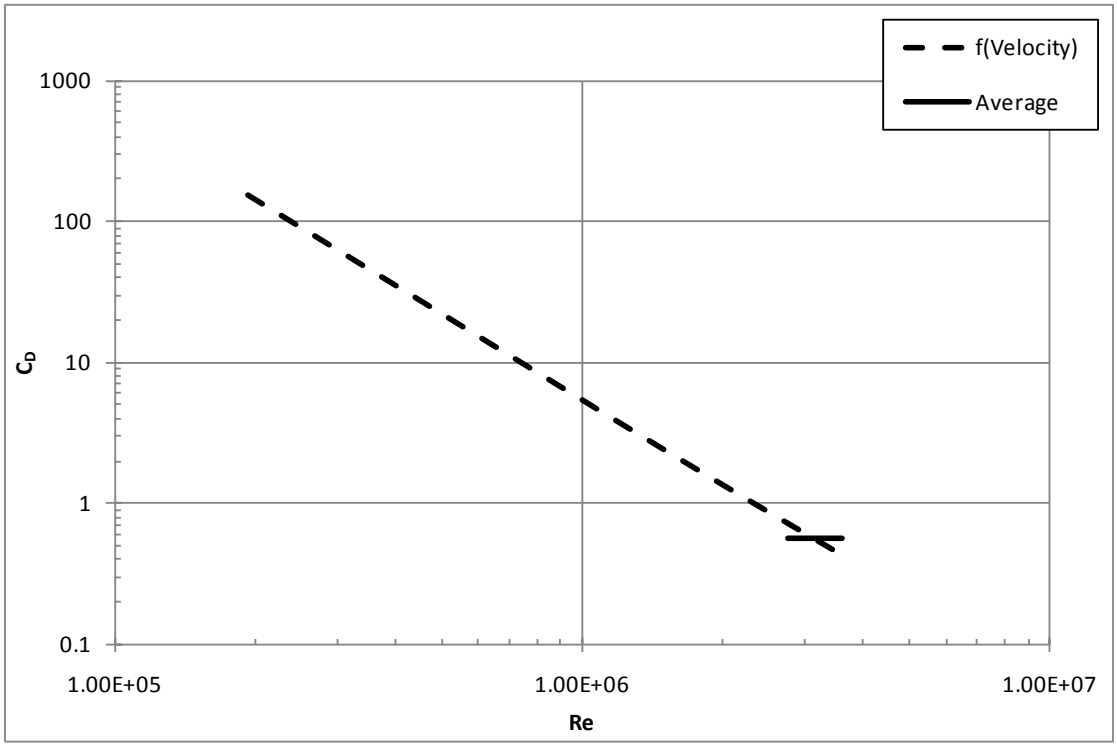

Figure 74. Free Fall Testing - Drag Coefficient as a Function of Re.

Free Fall Testing Discussion and Experimental Error

Overall, the free fall testing revealed a number of unique relationships between terminal velocity, anchor trajectory, and drag coefficient as affected by the anchor shape and the addition of a mooring rope. The mooring arm position did not significantly affect the drag coefficient whether it was I/L or B/T, a maximum of 18%, but the arm did affect the anchor trajectory. When the OMNI-Max anchor was released and allowed to enter free-fall, the anchor tended to veer away from the direction where the mooring arm was pointed. The reason is due to the weight of the mooring arm creating a moment

about the center of gravity of the anchor. This moment tended to push the nose of the anchor opposite the direction of the arm, resulting in the lower fins encountering increased drag forces as the anchor descended. The drag forces on the lower fins contribute a moment in the same direction as the mooring arm about the anchors' center of gravity. Meanwhile, the upper fins begin to experience increased drag forces, and due to the much larger surface area on the upper fins, the upper fin drag forces provided an equally strong countering moment about the anchors' center of gravity, opposite the direction of the lower fin and mooring arm moments. Therefore, the anchor does not turn "sideways" when released. However, the testing revealed a slight imbalance between moments because the anchor tracked away from the mooring arm.

However, when the mooring rope was attached to the mooring arm, the positively buoyant rope created a counteracting moment against the moment created by the mooring arm weight about the anchor center of gravity. Upon releasing the anchor and during descent, the rope appeared to balance the anchor into a straight, upright trajectory. This equal balance is primarily constituted from the moments created by the lateral drag forces on the upper fins , lateral drag force on the lower fins, vertical drag force on the mooring arm, weight of the mooring arm, buoyancy of the mooring line, and drag forces acting on the mooring line through the mooring arm. Further investigation into these relationships is recommended. Because in prototype applications, various types of mooring ropes may be attached to the anchor, affecting anchor trajectory.

The anchors' fin position affected the drag coefficient and terminal velocity of the anchor. The maximum change was 35% when the fins were placed from F/E to M/S with the mooring arm I/L. This is attributed to differences in human judgment when picking pixel coordinates on the images. The assumption is that the nose and tail pixel coordinates are separated by the anchor length. Therefore, if the chosen pixels were separated by a smaller distance compared to anchor length, then the pixel to inch ratio would decrease, resulting in a different anchor velocity. The fins in the M/S had the highest drag coefficient of 0.83 when the mooring arm was placed B/T. The lowest drag coefficient was 0.461 when the fins were F/E and the mooring arm was I/L, but the images were processed by another person which introduces a measure of uncertainty.

The errors influencing the results are more pronounced when compared to other phases of anchor testing. The most significant source of error is processing the images to track the same points of reference on the anchor as it is descending. Typical images used to calculate velocities are presented as Figure 75 for the shallow camera and Figure 76 for the deeper camera. The blur shown in the images is the result of the low frame rate of the camera. The light measurements recorded on the pixel board inside the camera optics can only be saved 30 times in one second, hence a 30 Hz frame rate. Therefore, the anchor moves so much that the measured light in the pixel changes before the data can be stored which results a blur of the image. The anchor being blurred is not a significant problem because if the same reference points are used accounting for the blur, like the darkest lowest pixel point on the nose, then fairly low error results are obtained.

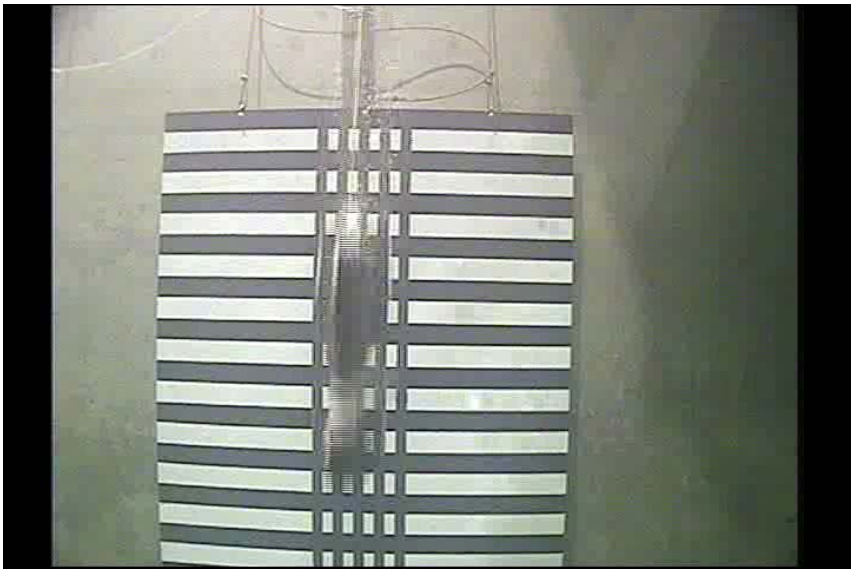

Figure 75. Typical Image Captured During Free Fall Testing – Shallow Camera.

Figure 76. Typical Image Captured During Free Fall Testing – Deep Camera.

Another source of error is related to the blurriness of the images. The reference points used, in most of the image processing, were the darkest, lowest pixel near the nose and the highest, lightest pixel where the white tips of the upper fins passed. Using

these points, it was assumed that the anchor length is the difference in pixels between the two points. Then knowing the anchor length and the difference in high and low pixels, the pixel to inch ratio was formulated. Therefore, the foundation of all calculations, the conversion to length scale, was based on human judgment. Computer programming was considered for image processing, but the images taken by the cameras have a low contrast and taken in color, which makes a computer analysis of the images very laborious and time consuming.

Even though this laboratory technique resulted in repeatable results, some improvements can be made. The most apparent is the acquisition of a high-speed camera which has the ability to be submerged into water. An average high speed camera typically saves approximately 1000 images taken over a second, which if applied to this phase of anchor testing would greatly enhance the resolution and reduce the amount of error. Another recommendation would be the addition of two more cameras positioned at the same depths as the original cameras, but looking West to East in the tow tank rather than just North to South. These additional cameras would allow tracking the anchors' descent in three dimensions and reducing error by generating more data. However, due to financial limitations and time constraints, acquiring the additional cameras were not feasible. Despite the limitations, the free fall testing of the OMNI-Max anchor produced good data to calculate terminal velocity and drag coefficient.

CONCLUSION

In conclusion, the OMNI-Max anchor was subjected to various phases of testing in the Haynes Laboratory. The soil penetration testing indicated the anchor penetrates slightly further into a mud when the mooring arm is in-line with fully extended fins. Also, the penetration depth of the anchor increases with a greater mudline impact velocity, which was caused by releasing the anchor from a higher elevation. The maximum amount of penetration was on the order of two anchor lengths.

During the tow testing phase, the upper and lower fins being set at the middle setting consistently causes the highest drag coefficient. The mooring arm being set in line with the fins caused a higher drag coefficient than it being placed between the fins. Also, the addition of a mooring line onto the mooring arm increased the drag coefficient 13.5%.

In the free fall testing phase, placing the fins into the middle setting and the mooring arm between the fins resulted in the highest drag coefficient. The anchor fell vertically when a buoyant mooring rope was attached to the mooring arm. Conversely, the anchor veered laterally in the opposite direction of the mooring arm when the mooring rope was unattached. The highest terminal velocity was calculated to be when the anchor fins were fully extended and mooring arm was in line with the fins. However, this is a result calculated with differences based on human judgments. Figure 77 shows the results for the anchor drag coefficients calculated in free fall and tow testing as a function of Re number compared to simply shaped objects. The plot does not include results where a mooring line was attached.

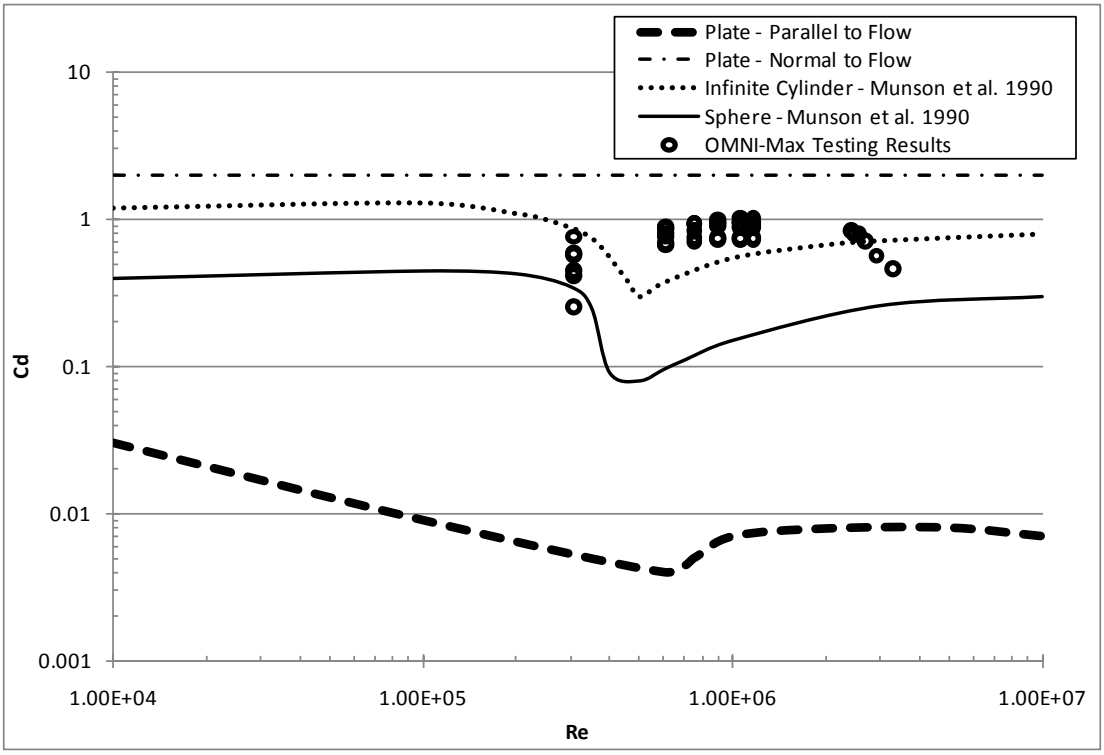

Figure 77. OMNI-Max Drag Coefficients as a Function of Re - Testing Results.

The data indicates that the laboratory techniques and methods captured good quality data which provided insights into the hydrodynamic relationships associated with the OMNI-Max anchor. When the laboratory results are scaled to prototype sized anchors, the recommended values for drag coefficient are summarized in Table 16 assuming the prototype anchor is 33 ft in length. When a mooring rope is attached to the anchor, a 15% increase in drag coefficient is recommended. The physical property values used for sea water are shown in Table 6. The OMNI-Max anchor is an innovative design in the offshore mooring system industry because it may be efficiently and quickly installed at minimal cost.

Table 16. Estimated Prototype Anchor Drag Coefficients.

Anchor Setting	Prototype Drag Coefficient
F/E I/L	0.65
F/E B/T	0.63
M/S I/L	0.81
M/S B/T	0.87
F/R I/L	0.77
F/R B/T	0.74

REFERENCES

Bradley, A. A., Kruger, A., Meselhe, E. A., and Muste, M. V.I. (2002). "Flow measurement in streams using video imagery." *Water Resources Research*, 38, (12), pp. 51/1 - 51/8.

Colliat, J-L. (2002). "Anchors for deepwater to ultradeepwater moorings." Proc., *2002 Offshore Technology Conference*, Houston, TX, Paper No. OTC 14306.

Ehlers, C. J., Young, A. G., and Chen, Jen-hwa. (2004). "Technology assessment of deepwater anchors." Proc., *2004 Offshore Technology Conference*, Houston, TX, Paper No. OTC 16840.

Einav, I, Klar, A., O'Loughlin, C. D., and Randolph, M. F. (2003). "Numerical modelling of deep penetrating anchors." Proc., *9th Australia New Zealand Conference on Geomechanics*. Auckland, Vol. 2, pp. 591-597.

Fernandes, A. C., and Mineiro, F. P.S. (2007). "Assessment of hydrodynamic properties of bodies with complex shapes." *Applied Ocean Research*, Vol. 29, pp. 155-166.

Fernandes, A. C., Sales JR, J. S., and Santos, M. F. (2009). "Installation of deepwater devices analysis through deepwater model testing." 4th International Workshop on Applied Offshore Hydrodynamics. Rio de Janeiro, BRAZIL.

Fernandes, A. C., Araujo, J. B., Almeida. J. C. L., Machado, R. D., and Matos V. (2006). "Torpedo anchor installation hydrodynamics." *Journal of Offshore Mechanics and Arctic Engineering*. Vol. 128. pp. 286-293.

Hartman, M., and Yates, J. G. (1993). "Free-fall of solid particles through fluids." *Collection of Czechoslovak Chemical Communications*, Vol. 58. pp. 961-982.

Hoerner, Sighard F. (1965). *Fluid-dynamic drag,* Brick Town, N.J.: Hoerner Fluid Dynamics.

Kundu, P. K., and Cohen, I. M. (2008). *Fluid mechanics* (4th ed.), Burlington, MA.: Academic Press, 2008.

Munson, B. R., Young, D. F., and Okiishi, T. H. (1990). *Fundamentals of fluid mechanics*, New York: John Wiley & Sons.

O'Loughlin, C. D., Randolph, M. F., and Richardson, M. (2004). "Experimental and theoretical studies of deep penetrating anchors." Proc., *2004 Offshore Technology Conference*, Houston, TX, Paper No. OTC 16841.

Randall, R. E. *Elements of ocean engineering.* (2nd ed), Jersey City, N.J. Society of Naval Architects and Marine Engineers.

Shelton, J. T. (2007). "OMNI-Max anchor development and technology." *2007 Oceans Conference*, Vancouver, B.C., Canada, Vol. 1-5, pp. 1900 - 1999.

Stewart, D. P., and Randolph, M. F. (1994). "T-bar penetration testing in soft clay." *Journal of Geotechnical Engineering*, 120, pp. 2230-2235.

Swift, M. R., Fredriksson, D. W., Unrein, A., Fullerton, B., Patursson, O., and Baldwin, K. (2006). "Drag force acting on a biofouled net panels." *Aquacultural Engineering*, Vol. 35, pp. 292-299.

True, D. G. (1975). *Penetration of projectiles into seafloor soils.* Port Hueneme, California: Civil Engineering Laboratory (Navy).

Young, D. R. (2009). "Forces on laboratory model dredge cutterhead." Texas A&M University, Ocean Engineering, College Station, TX.

Zimmerman, E. H., Smith, M. W., and Shelton, J. T. (2009). "Efficient gravity installed anchor for deepwater mooring." Proc., *2009 Offshore Technology Conference.* Houston, TX. Paper No. OTC 20117.

VITA

William André Cenac II received his Bachelor of Science degree in civil engineering from the University of Louisiana - *Lafayette* in December 2008. He entered the Ocean Engineering Program at Texas A&M University in January 2009 and received his Master of Science degree in May 2011. His studies focused on coastal engineering design and coastal planning. His research focused on laboratory experiments of vertically loaded anchors for deepwater mooring applications. He intends to make a career in the coastal engineering field by working towards ownership of a coastal construction company.

Mr. Cenac may be reached through the Coastal and Ocean Engineering Division, Zachry Department of Civil Engineering, 3136 TAMU, Texas A&M University, College Station, TX 77843. His email is cenac86@yahoo.com.

Name:	William André Cenac II
Address:	Ocean Engineering Program Zachry Department of Civil Engineering 3136 TAMU Texas A&M University College Station, TX 77843-3136
Email Address:	cenac86@yahoo.com
Education:	B.S., Civil Engineering, University of Louisiana - *Lafayette*, 2008 M.S., Ocean Engineering, Texas A&M University, 2011